TU Delft

Delft University of Technology

Anisotropic and Magnetic Microparticles: Preparation and Out-of-Equilibrium Assembly

Schyck, S.N.

DOI
10.4233/uuid:8fee3f85-44ab-4959-820f-d82695fcbeb7

Publication date
2023

Document Version
Final published version

Citation (APA)
Schyck, S. N. (2023). *Anisotropic and Magnetic Microparticles: Preparation and Out-of-Equilibrium Assembly*. [Dissertation (TU Delft), Delft University of Technology]. https://doi.org/10.4233/uuid:8fee3f85-44ab-4959-820f-d82695fcbeb7

Important note
To cite this publication, please use the final published version (if applicable).
Please check the document version above.

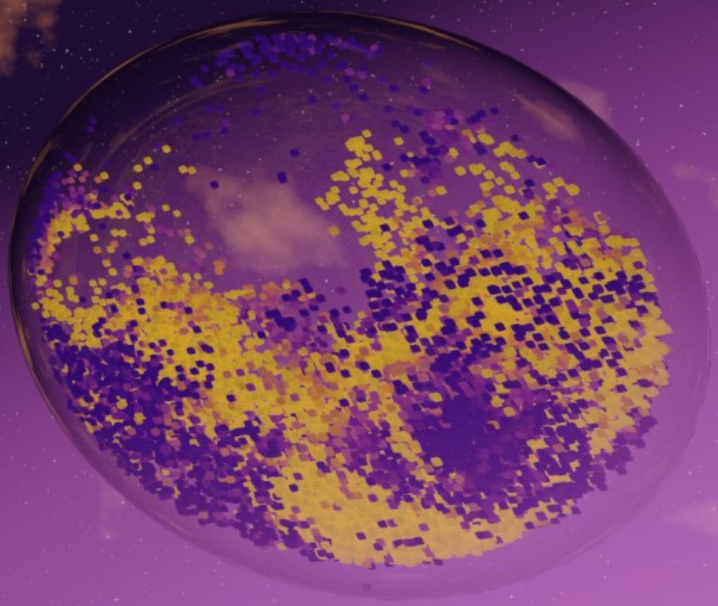
Copyright
Other than for strictly personal use, it is not permitted to download, forward or distribute the text or part of it, without the consent of the author(s) and/or copyright holder(s), unless the work is under an open content license such as Creative Commons.

Takedown policy
Please contact us and provide details if you believe this document breaches copyrights.
We will remove access to the work immediately and investigate your claim.

This work is downloaded from Delft University of Technology.
For technical reasons the number of authors shown on this cover page is limited to a maximum of 10.

Anisotropic and Magnetic Microparticles

Preparation and Out-of-Equilibrium Assembly



Sarah Schyck

Anisotropic and Magnetic Microparticles: Preparation and Out-of-Equilibrium Assembly

Anisotropic and Magnetic Microparticles: Preparation and Out-of-Equilibrium Assembly

Proefschrift

ter verkrijging van de graad van doctor
aan de Technische Universiteit Delft,
op gezag van de Rector Magnificus Prof.dr.ir. T.H.J.J. van der Hagen,
voorzitter van het College voor Promoties,
in het openbaar te verdedigen op woensdag 6 september 2023 om 12.30 uur

door

Sarah Nicole SCHYCK

Master of Science in Physics,
University of Nevada Las Vegas, Verenigde Staten,
geboren te Murray, Verenigde Staten.

Dit proefschrift is goedgekeurd door de

Samenstelling promotiecommissie:

Rector Magnificus,	voorzitter
Dr. P.E. Boukany,	Technische Universiteit Delft, Promotor
Dr. L. Rossi,	Technische Universiteit Delft, Copromotor

Onafhankelijke leden:

Prof. dr. ir. A. Urakawa,	Technische Universiteit Delft
Prof. dr. A.P. Philipse,	Universiteit Utrecht
Dr. ir. C. Chassagne,	Technische Universiteit Delft
Dr. J.A. Dijksman,	Universiteit van Amsterdam
Prof. C.A. Dransfeld	Technische Universiteit Delft, reservelid

Overige lid:

Prof. dr. S. Sacanna,	New York University



The research described in this thesis was performed in the Advanced Soft Matter (ASM) section at the Delft University of Technology, Faculty of Applied Sciences, Department of Chemical Engineering.

Keywords: Colloids, Self-assembly, Magnetic Microparticles, and Active Motion

Printed by: Proefschriftspecialist

Front & Back: Cover art prepared by Sarah Schyck in Blender.

Copyright © 2023 by S. Schyck

ISBN 978-94-6384-467-3

An electronic version of this dissertation is available at
http://repository.tudelft.nl/.

Contents

1 General Introduction **1**
1.1 Colloids . . . 2
1.1.1 Particle Interactions . . . 2
1.1.2 Magnetic Particles . . . 4
1.2 Colloidal Assembly . . . 6
1.3 Thesis Outline . . . 7

I Droplet-based Assembly of Microparticles **9**

2 Hollow Superball Assembly **11**
2.1 Introduction . . . 12
2.2 Experimental Methods . . . 13
2.2.1 Particle Preparation . . . 13
2.2.2 Assembly Process . . . 14
2.3 Results . . . 16
2.4 Discussion . . . 25
2.5 Conclusions . . . 26

3 Magnetic Superball Assembly **27**
3.1 Introduction . . . 28
3.2 Methods . . . 29
3.2.1 Particle Synthesis . . . 29
3.2.2 Sample Preparation . . . 29
3.2.3 Small Angle X-ray Scattering (SAXS) Measurements . . . 30
3.3 Results and Discussion . . . 30
3.3.1 Superball Properties . . . 30
3.3.2 Effect of Droplet Confinement . . . 31
3.3.3 Effect of Superball Shape in Capillary Sediments . . . 34
3.3.4 Effect of Superball Shape . . . 37
3.3.5 Effect of Magnetic Field on Evaporating Droplets . . . 38
3.3.6 Effect of Superball Shape and an Applied Field . . . 42
3.4 Conclusions . . . 45

II Active Swimming of Hematite Microparticles **47**

4 Active Hematite Swimmers **49**
4.1 Introduction . . . 50
4.2 Experimental Methods . . . 51
4.2.1 Colloid Synthesis . . . 51
4.2.2 Particle Calcination . . . 51
4.2.3 Particle Characterization . . . 51

4.2.4 Active Motion Imaging . . . 52
4.3 Results and discussion . . . 52
4.3.1 Active Motion of Hematite . . . 52
4.3.2 Active Motion of Calcined Hematite . . . 54
4.3.3 Optical and Surface Properties . . . 58
4.4 Conclusions . . . 59

III Preparation of Magnetic Microparticles 61

5 Magnetic Polystyrene 63
5.1 Introduction . . . 64
5.2 Materials and Experimental Methods . . . 65
5.2.1 Materials . . . 65
5.2.2 Methods . . . 65
5.3 Results and Discussion . . . 67
5.3.1 Effect of Surfactant Concentration . . . 67
5.3.2 Effect of Solvent-to-Water Ratio and Polymer Concentration . . . 69
5.3.3 Effect of Polystyrene to Cobalt Ferrite Ratio . . . 70
5.3.4 Effect of Plasticization . . . 74
5.4 Conclusions . . . 76

6 Anisotropic Magnetic Polystyrene 79
6.1 Introduction . . . 80
6.2 Experimental Methods . . . 82
6.2.1 Particle Synthesis . . . 82
6.2.2 PVA Film Preparation . . . 82
6.2.3 PVA film Stretching . . . 82
6.2.4 Particle Recovery . . . 83
6.2.5 Characterization . . . 83
6.3 Results and Discussion . . . 83
6.4 Conclusions . . . 88

7 General Conclusions & Outlook 91
7.1 Conclusions . . . 92
7.2 Outlook . . . 93
7.2.1 Self-assembly of Anisotropic Superball Particles . . . 93
7.2.2 Active Hematite Microswimmers . . . 94
7.2.3 Anisotropic and Magnetic Particle Preparation . . . 94

Bibliography 97

A Additional Sample Images 115
A.1 Additional Images for Chapter 5 . . . 115

Summary 129
Samenvatting 131
Acknowledgments 133
About the Author 137
Publications 139

Chapter 1

General Introduction

ABSTRACT:

Colloidal particles have captured the attention of researchers since their initial discovery in the early 1800s, owing to their distinct and often material-dependent properties. They find extensive applications across diverse fields such as biomedicine and microelectronics. This thesis aims to address the existing constraints faced by anisotropic and magnetic colloidal particles in the design of self-assembled materials and as photocatalytically active particles, seeking to enhance their performance. Furthermore, novel preparation methods for anisotropic composite magnetic microparticles are pursued. The introductory chapter begins with a concise overview of significant colloidal properties. It proceeds with a brief summary of the behavior of magnetic materials and the phenomenon of colloidal assembly, which constitute the central focus of this thesis. Finally, the outline of the subsequent chapters is presented and discussed.

1

1.1. Colloids

Colloidal particles are microscopic particles with a size range of a few nanometers to several micrometers that are dispersed in a liquid, solid, or gas medium. They can be composed of various materials, such as polymers or metals, and exhibit diverse shapes, including ellipsoids [1] and fractal snowflakes [2]. Examples of colloids found both inside and outside the laboratory are depicted in Figure 1.1. Due to their small size and large surface area, colloidal particles possess unique properties.

One crucial characteristic of colloidal particles is their tendency to undergo Brownian motion, which refers to the random movement of a particle due to collisions with surrounding molecules. The diffusion of a hard-sphere particle resulting from Brownian motion is governed by the Stokes-Einstein equation:

$$D_0 = \frac{k_B T}{6\pi\eta r}. \tag{1.1}$$

Here, k_B denotes the Boltzmann constant, η represents the viscosity of the continuous phase, T is the temperature, and r is the radius of the spherical particle [3]. Brownian particles typically range in size from a few nanometers to several microns, depending on the temperature and solvent viscosity. The diffusion coefficient, D_0, is related to the mean-squared distance that a particle travels after time t according to the Sutherland-Einstein-Smoluchowski equation [3]:

$$\langle \Delta r^2(t) \rangle = 2dD_0 t. \tag{1.2}$$

In this equation, $\langle \Delta r^2(t) \rangle$ represents the mean-squared displacement, and d is the number of accessible dimensions. For the scope of this thesis, $d = 2$ for particles confined to a 2D plane of a capillary, or $d = 3$ for particles allowed omnidirectional movement, as demonstrated in Part I.

1.1.1. Particle Interactions

As colloidal particles approach each other, their stability in a dispersion depends on whether they repel or attract each other. Colloidal dispersions are inherently unstable due to the large surface area of the particles, which leads to aggregation followed by

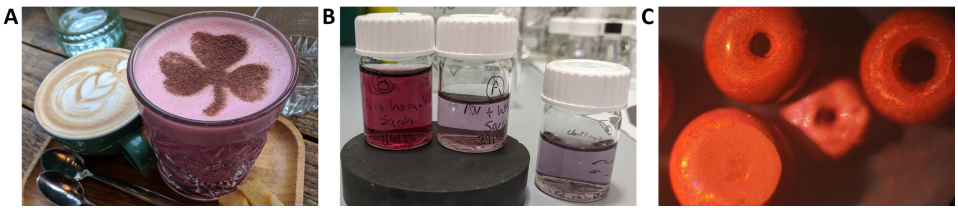


Figure 1.1: Colloidal examples from everyday life outside (and inside) the laboratory. (A) Decorative foams on top of lattes from a local café, where gas microbubbles act as a colloidal suspension inside a liquid. (B) Colloidal gold nanoparticles dispersed in water, generating different colored suspensions depending on the nanoparticle sizes. (C) Colloidal hematite particles assemble into opal-like structures with iridescent coloring under distinct conditions.

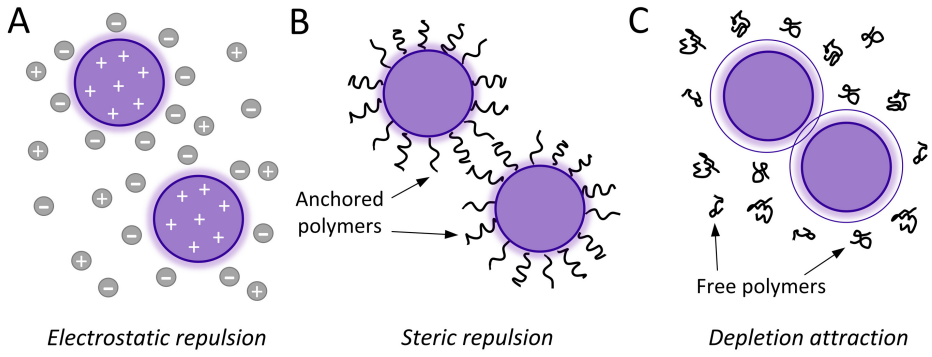


Figure 1.2: Summary of important colloidal interactions: (A) Electrostatic repulsion, (B) steric (polymer) repulsion, and (C) depletion attraction.

sedimentation or creaming [3]. To maintain a stable colloidal system, it is essential for the colloidal particles to remain suspended in the solvent.

The primary force that colloidal particles need to overcome is the attractive van der Waals (vdW) force. Short-range vdW interactions arise from the additive interactions between atoms of two colloidal particles in close contact [4]. Electrostatic repulsion between colloidal particles often balances this attractive force. Electrostatic repulsion occurs when the surface of a colloidal particle carries a charge. The surface charge attracts ions with an opposite charge in the solvent and repels ions with similar charges. This creates an electrical double layer around the colloidal particle, which can be controlled by the concentration of ions in the solvent, such as by adjusting the electrolyte concentration in the system. When the electrical double layers of two colloidal particles overlap, they repel each other (Figure 1.2). The interaction energy between two colloidal particles based solely on these forces is described by the DLVO theory, named after Derjaguin and Landau [5] and Verwey and Overbeek [6]. This theory has been successful in explaining colloidal phenomena, although it does not encompass all forces that can be important for colloidal system stability.

One common approach to control colloidal stability is through the addition of polymers. Polymers can interact with colloidal dispersions by either being anchored on or free near the particle's surface [7]. When polymers are anchored on the surface of a particle, the colloidal interaction depends on several factors: (i) the type of polymer, (ii) the type of solvent, and (iii) how the polymer is anchored. Different types of polymers can be adsorbed on the particle's surface through dipole interactions, Coulombic (charge-charge) interactions, vdW forces, or hydrogen bonding [4]. When two polymer-coated particles approach each other in a good solvent, the polymer chains overlap and compress. This results in a repulsive osmotic force between the particles, preventing their surfaces from getting too close to each other. This mechanism is known as steric stabilization (Figure 1.2B). However, in a non-ideal solvent for the polymer, the polymer chains collapse and lose their steric stabilization, leading to a net attractive force between the two coated colloidal particles due to vdW forces [7]. On the other hand, free polymers can cause depletion interactions between particles [8]. When two colloidal particles come

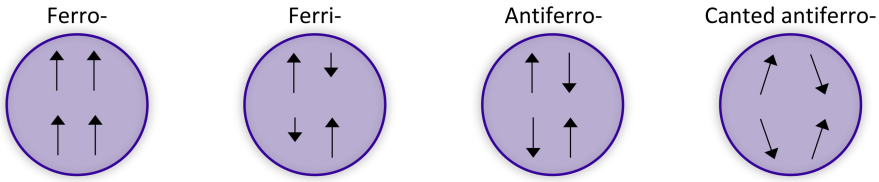


Figure 1.3: Schematics of the spin orientation for ferro, ferri-, antiferro-, and canted antiferro-magnets.

close enough together, their excluded volumes overlap, and free polymers are expelled from the space between them (Figure 1.2C). This generates depleted polymer zone which results in a net attractive force between particles [9]. For a more in-depth understanding of colloidal particle interactions, comprehensive books and reviews have been published [4, 7, 8, 10–13].

1.1.2. Magnetic Particles

In addition to the aforementioned forces, magnetic particles introduce an entirely new dimension of interactions that significantly impact colloidal systems. Magnetic colloids have a wide range of functions due to their ability to interact with each other and with magnetic fields, making them of interest in various fields such as microelectronics and biomedical diagnostics [14–18]. The origin of magnetic fields in materials can be attributed to the movement of electrical charges.

At the elementary scale, electrons themselves posses a permanent magnetic dipole moment, due to their intrinsic electric charge and motion known as spin. Therefore, the arrangement of electrons inside an atom determines the atomic magnetic moment. The arrangement of electrons within an atom determines its atomic magnetic moment. The Pauli exclusion principle dictates that electrons cannot occupy the same state, resulting in opposite spins if they are in the same orbital [19]. Unpaired electrons lead to a net magnetic moment for an atom. Based on the ordering and net magnetism of atomic magnetic dipoles in the presence and absence of a magnetic field, materials can be classified as diamagnetic, paramagnetic, ferromagnetic, antiferromagnetic, or ferrimagnetic (Figure 1.3) [14].

In **diamagnetism**, which applies to all materials, the motion of electrons changes under an applied magnetic field, resulting in a weak magnetization that opposes the field. Pure diamagnetic materials do not have a net magnetic moment in the absence of a field. Materials that are not *purely* diamagnetic fall into the following categories.

In **paramagnetism**, the atomic magnetic dipoles are uncorrelated with each other due to either their low concentrations, which prevent their spins from interacting, or weak interactions between them that maintain a net magnetization of zero. As a result, the atomic dipoles undergo orientational fluctuations due to thermal motion. When a magnetic field is applied, the dipoles align along the field direction but randomly reorient after the field is removed. For **ferromagnetism**, the atomic moments are parallel with each other; thus, the material possesses a macroscopic magnetization. **Antiferromagnetism** results from atomic moments coupled antiparallel with each other. Here,

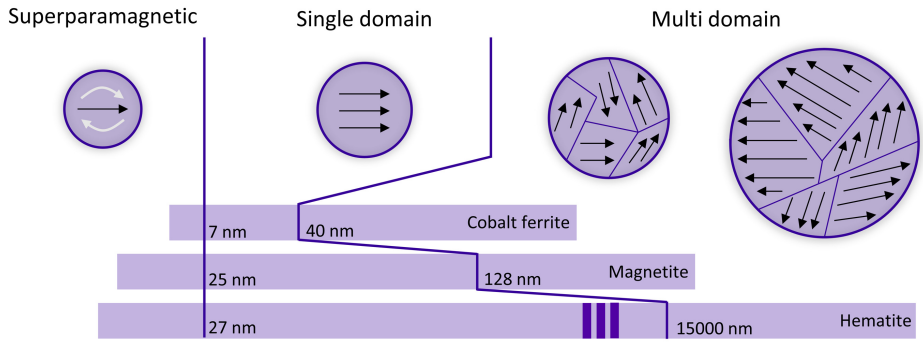


Figure 1.4: Schematics of the transition from super-paramagnetic to single domain to multi-domain with the size transitions of cobalt ferrite [22], magnetite [23], and hematite [20] as examples.

the atomic moments have the same magnitude which leads to no net magnetization. When atomic moments that are antiparallel do not have the same magnitude, as is the case for **ferrimagnetism**, the material possesses net magnetization. We note that some antiferromagnetic materials can still posses net magnetization via spin canting. A well known example of this is hematite which has canted antiferromagnetism due to the spin-orbital coupling allowed by its crystal structure [20]. We take advantage of hematite's net magnetization in chapter 3.

Magnetic materials possess several key properties related to their magnetization behavior. For example, the maximum magnetization of a material occurs when all atomic moments are aligned in the same direction, often achieved under an applied field, and is known as the saturation magnetization, M_s. After the magnetic field is removed, the material may retain a remnant magnetization, representing the magnetization parallel to the field that persists for a certain duration depending on its (magneto)crystalline anisotropy [14]. For instance, cobalt ferrite has a similar saturation magnetization to magnetite but a larger crystalline anisotropy, causing the magnetic moment of cobalt ferrite to relax more slowly after magnetization [21]. This property has significant implications in colloidal design, as demonstrated in chapter 6.

Effect of particle size in magnetic materials

In colloidal magnetic particles, the properties at the nano- and micro-scale can differ significantly from those in the bulk phase [14]. Figure 1.4 illustrates the arrangement of atomic moments in differently sized particles. When the particle size exceeds a critical diameter, d_0, which is material-dependent, magnetic domains form within the particle to minimize the total magnetostatic energy. A magnetic domain refers to a region in the material with uniform magnetization. To reduce the total magnetostatic energy, magnetic domains form with non-parallel magnetization orientations. Consequently, particles with multiple magnetic domains exhibit an approximate net magnetization of zero.

For particles below d_0, the formation of domain walls is no longer energetically favorable, resulting in particles with a permanent dipole moment. Single-domain particles have their magnetic moment aligned along a specific direction, known as the easy-axis,

which is influenced by the material and particle shape [24]. Further reduction in particle size can lead to **superparamagnetic** particles, where the magnetic dipole moment can be easily fluctuated by thermal motion. The critical sizes at which these transitions occur vary depending on the material's intrinsic properties. For instance, the single-to-multidomain transition can occur at the nanoscale, such as cobalt ferrite at approximately 40 nm [22] and magnetite at 128 nm [23], or at the microscale, as observed in hematite at around 15 μm [20]. Figure 1.3 provides a scheme of the concepts discussed in this section.

1.2. Colloidal Assembly

Colloidal particles may be thought of as building blocks for well-ordered structures, with the potential to produce functional materials with desirable qualities [25, 26]. In this respect, colloidal crystals act as both a significant model system for studying the atomic world [27] and a distinctive method for creating new functional materials on the macroscale [28]. In general, the macroscopic structure that the particles assemble into is dependent on (i) the constituent particles' shape, (ii) inter-particle interactions, and (iii) the assembly method. The simplest particle shape, a sphere, often forms face-centered cubic (fcc), hexagonally close-packed (hcp), or randomly hexagonally close-packed (rhcp) assemblies [27, 29]. Additionally, anisotropic colloids can form colloidal crystals with rich structural diversity or desirable optical or mechanical properties. For example, simulations of faceted polyhedra, which carefully control the design of the polyhedra shape, produce a variety of phases from liquid and plastic crystals to solid crystals with specific lattices beneficial for the hierarchical design of functional materials [30, 31]. Experimentally, anisotropic particles, such as polyhedra, rods, or branch-like particles, have been assembled into close-packed 2D arrays and 3D superstructures by a variety of assembly techniques such as solvent evaporation, sedimentation, or via external forces [26]. One assembly method, utilized throughout Part I of this thesis, relies on evaporation of solvent from a spherical droplet. Initially, the colloidal particles are randomly distributed throughout the bulk of these droplets. As the droplets dry, the particle concentration increases and inter-particle forces (e.g., van der Waals or magnetic dipole-dipole interactions) force the particles to assemble which results in macro-scale, free-standing supraparticles (Figure 1.1 C) [26, 32–34].

Active Colloidal Particles

Another intriguing out-of-equilibrium colloidal system is active particles, which are capable of autonomous motion. These self-propelled particles offer exciting opportunities for various applications, including targeted drug delivery [35], environmental remediation[36–38], and microscale robotics [39]. By harnessing the catalytic properties of certain materials, such as platinum or hematite[40, 41], active colloidal particles can convert the chemical energy of H_2O_2 into mechanical motion, enabling them to move in a directed and controlled manner. This propulsion mechanism relies on the generation of concentration gradients and the ensuing fluid flow around the particles [39]. We utilize this property of hematite microswimmers in Part II. The active motion of these colloidal systems not only exhibits fascinating dynamic behavior but also opens up possibilities for manipulating and directing the motion of individual particles and their assemblies [42].

1.3. Thesis Outline

In this thesis, we explore how to overcome some of the constraints current anisotropic and magnetic particles face in the design of self-assembled materials and as active particles, and we seek to develop new preparation methods for composite magnetic microparticles. Following the theoretical background, the content of the thesis has been divided into three parts: droplet-based assembly, active motion, and preparation of anisotropic and magnetic microparticles.

In Part I, we focus on the assembly of magnetic colloids with particles prepared from well-known synthesis methods. Specifically, it explores the self-assembly of functional materials and how particle anisotropy affects the resultant structures. We first investigate the effect of shape anisotropy (chapter 2) followed by the addition of magnetic anisotropy (chapter 3) throughout various particle assemblies. In Part II, we utilize the photocatalytic proprieties of hematite to autonomously propel microparticles. This active motion is necessary for the preparation of micro- and nano-scale robots. We also demonstrate a simple method to increase the active motion of magnetic hematite particles under ultraviolet irradiation (chapter 4). Part III deals with the preparation and characterization of tailored (composite) magnetic microparticles. A simple emulsion-based synthesis method is discussed (chapter 5) which is used as a basis for creating shape anisotropic particles (chapter 6). Finally, we conclude the thesis and provide an outlook on the future directions and applications of the particle systems explored (chapter 7).

Part I

Droplet-based Assembly of Microparticles

Chapter 2

Self-assembly of Colloidal Superballs Under Spherical Confinement of a Drying Droplet

ABSTRACT:

Understanding the relationship between colloidal building block shape and the assembled material structure is important for the development of novel materials by self-assembly. In this regard, colloidal superballs are unique building blocks because their shape can smoothly transition between spherical and cubic. Assembly of colloidal superballs under spherical confinement results in macroscopic clusters with ordered internal structure. By utilizing Small Angle X-Ray Scattering (SAXS), we probe the internal structure of colloidal superball dispersion droplets during confinement. We observe and identify four distinct drying regimes that arise during compression via evaporating droplets, and we track the development of the assembled macrostructure. As the superballs assemble, we found that they arrange into the predicted paracrystalline, rhombohedral C_1-lattice that varies by the constituent superballs' shape. This provides insights in the behavior between confinement and particle shape that can be applied in the development of new functional materials.

Parts of this chapter have been published in JCIS Open **5**, 100037 (2022) [43].
The data that support the findings of this chapter are openly available in 4TU.ResearchData at https://doi.org/10.4121/19122308.v1 reference number [44].

2.1. Introduction

The self-assembly of colloidal particles is an ideal mechanism for structuring matter at the nano- and microscale, and can produce materials of interest for different applications, such as photonics, opto-electronics, catalysis or energy storage [45, 46]. To direct the self-assembly process towards the desired structures, different methods have been developed and explored [47]. One unique way to tune the spontaneously formed structures is to assemble the colloidal particles under spherical confinement induced by evaporating micro-emulsion droplets or larger dispersion droplets [48–51]. Colloidal spheres typically crystallize into face centered cubic (FCC) crystal phases. When this type of crystallization occurs under spherical confinement, unique optical properties can arise in the final clusters, i.e., structural colors [50, 52, 53]. Furthermore, control over the number of particles inside a dispersion droplet has been shown to produce novel structures, such as icosahedral clusters and magic number clusters [54–56]. Depending on the initial colloidal volume percent and the drying substrate properties, dispersion droplets drying on superhydrophobic surfaces can form various cluster shapes, e.g., doughnuts or flattened discs and spheres [48, 52, 53, 57].

Besides finely tuning the assembly process, improvements in the synthesis of anisotropic colloidal particles have opened the path for more structurally varied assemblies [58]. Consequently, there is a great diversity within the colloidal assemblies of different anisotropic and polyhedral shapes [31, 59, 60]. Combining spherical confinement with anisotropic shapes can lead to even more complex micro structures. For instance, simulations of different polyhedral shapes showed that spherical confinement leads to unique clusters distinctly different from the packings of spheres [30]. For rod-like colloids, it was found that confinement led to disordered supraparticles possessing unique scattering enhancing properties in contrast to their spherical counterparts [61]. Among available anisotropic particles, the superball shape, which encompasses the transition from a sphere to a cube via a rounded cube, has become of interest due to its unique shape-dependent phase behaviour and experimental availability [62–67]. For hard superballs, the densest packing is a rhombohedral-like crystal structure that, with increasing asphericity of the superballs, continuously evolves from an FCC lattice (spheres) to a simple cubic (SC) lattice (perfect cubes) [62, 63, 65, 66, 68]. Before assembling into their densest packings from a liquid phase, superballs can form a plastic crystal (or rotator) phase which has translational order and rotational mobility [64, 68]. Experimentally, the phase diagram of micron-sized superballs has been studied via crystallization under gravitational settling in a capillary and depletion-assisted assembly [67–69]. For nano-sized superballs, the dense packings have also been investigated [65, 66]. These studies also confirmed the formation of dense rhombohedral-like structures of which the exact packing is dependent on the asphericity of the superball shape.

In addition, the self-assembly of micron-sized superballs into monolayers driven by solvent evaporation processed on flat substrates was investigated [70, 71]. These studies showed that solvent flow and immersion capillary forces, which can reach 10^6 kT for micron-sized colloids, will lead to the formation of similar dense rhombohedral-like crystal structures but also revealed that the out-of-equilibrium process induces the formation of lower density crystal lattices with hexagonal-like structures as well as disordered packings. So far, only a few studies have investigated the effect of spherical confinement on

the assembly of superball (cubic-like) particles and the relationship between particle asphericity and the resulting densely packed structure symmetries. For superball nanoparticles with increasing asphericity, the confined structure changes from icosahedral clusters with strong local orientation to simple-cubic structures [56]. Cubic nanoparticles, with very sharp edges, assemble at the surface and in bulk of the droplet and form densely packed clusters with random orientations throughout the confined structure [33]. Moreover, it has been shown that when nanocubes form dense supraparticles, the finite corner roundness and the surface tension of the confining droplet determine the superstructure morphology [34]. To understand the final self-assembled supraparticles' structure formed by superballs, it is crucial to understand the dynamics of the particles during droplet evaporation. For this, small angle x-ray scattering (SAXS) is a very powerful tool that allows visualization of the assembly process of different nanoparticles during spherical confinement in detail and has been used to resolve micron-sized superball particle assembly [33, 68, 72–74].

In this chapter, we use in-situ synchrotron small angle X-ray scattering with microradian resolution (μrad-SAXS) to reveal the crystallization process of micron-sized silica superball shells under spherical confinement through droplet drying and elucidate the structural transitions during assembly. We are able to follow the droplet evaporation process in detail and identify different stages during the process. As the solvent evaporates, the particle concentration increases. After this stage, dewetting of the superball shells occurs before full solvent evaporation. We find that crystalline structures start to form as particle concentration increases, and that the structures remain throughout the later stages. In addition, we find that as we increase the asphericity of the superballs, the assembled supraparticles' structures are polycrystalline assemblies of their predicted rhombohedral-like lattices.

2.2. Experimental Methods

The experimental methods detailed below include the particle preparation for the superball particles and the assembly process for the generation of superball assemblies. This includes the variety of characterization methods in determination of particle morphology and assembled structures.

2.2.1. Particle Preparation

Hematite cube template particles were prepared following a sol-gel procedure [75]. Silica shells were grown following Ref. [76]. The hematite templates were dissolved through the addition of hydrochloric acid to produce hollow shells. The complete particle synthesis procedure to obtain different m values can be found in Ref. [69]. Silica spheres were prepared using a variation on the Stöber method [77] from Ref. [78] to create spheres with diameter of $D \approx 500$ nm. The obtained particles were characterized by transmission electron microscopy (TEM - Philips TECNAI12/20). Details on the properties of all prepared particles are presented in Table 2.1.

Table 2.1: A table of all samples and their parameters used in this work. Solid silica spheres are denoted by the prefix *S* while hollow silica superballs are denoted by the *HSB* prefix in the sample name. The outer *m* value denotes the shell shape while the inner *m* denotes the core shape. The thickness, *t*, is in nm along with half the distance between two flat faces, *a*, or the radius in the case of spherical particles.

Name	Outer m	Inner m	t (nm)	a (nm)
S1	2	–	–	233
S2	2	–	–	206
HSB1	2.6	3.65	220	512
HSB2	2.8	3.65	187	446
HSB3	3.1	3.65	56	315
HSB4	3.3	3.9	111	413

2.2.2. Assembly Process

Superball particles are assembled in an aqueous droplet deposited on a superhydrophobic surface. Preparation methods for the superhydrophobic surface and assembled colloids are highlighed in this section.

Superhydrophobic Substrate

Superhydrophobic substrates with contact angles above 160° were prepared following a modified procedure from Deng *et al.* [79]. Briefly, a thin layer of soot from the flame of a paraffin candle is deposited on a cleaned glass substrate. Then, the substrate is coated with a thin silica layer by enclosing it in a desiccator with two open containers of 2mL tetraethyl orthosilicate and 2mL NH_3 (29 wt%) for 24 hr. The substrate is then calcinated in an Evenheat Rampmaster RM2 furnace by heating at 600°C for 2 hr. After, 350 μL of 1% trichlorododeylsilane in chloroform is dropcasted on the substrate and allowed to evaporate. Droplet pinning positions are created on the substrate via notches on the surface.

Spherical Confinement of Colloids

Self assembled macrostructures of colloidal spheres and superballs were formed by depositing and drying 2-5 μL droplets of colloidal dispersions from 5 to 30 vol% on a superhydrophobic substrate at the pinning positions. These are necessary to prevent the droplets from moving and escaping the superhydrophobic surface. Evaporation rates were be controlled via drying inside a humidity chamber.

Small Angle X-ray Scattering (SAXS) Measurements

μrad-SAXS measurements were conducted at the beamline BM26B DUBBLE [80] at the European Synchrotron Radiation Facility (ESRF) in Grenoble, France using a microradian setup [81] employing compound refractive lensens [82]. The incident X-ray beam with a photon energy of 13 keV (λ = 1.0332 Å) was focused on a Photonic Science CCD detector with $4,008 \times 2,671$ pixels and a pixel size of 22×22 μm at a distance of 7.11 m. The detector was protected from the direct beam by a wedge-shaped beam-stop. Substrates with the drying droplets were placed horizontally in the X-ray beam. Measurements were performed during the full evaporation process at the position of the initial center of the drying droplet.

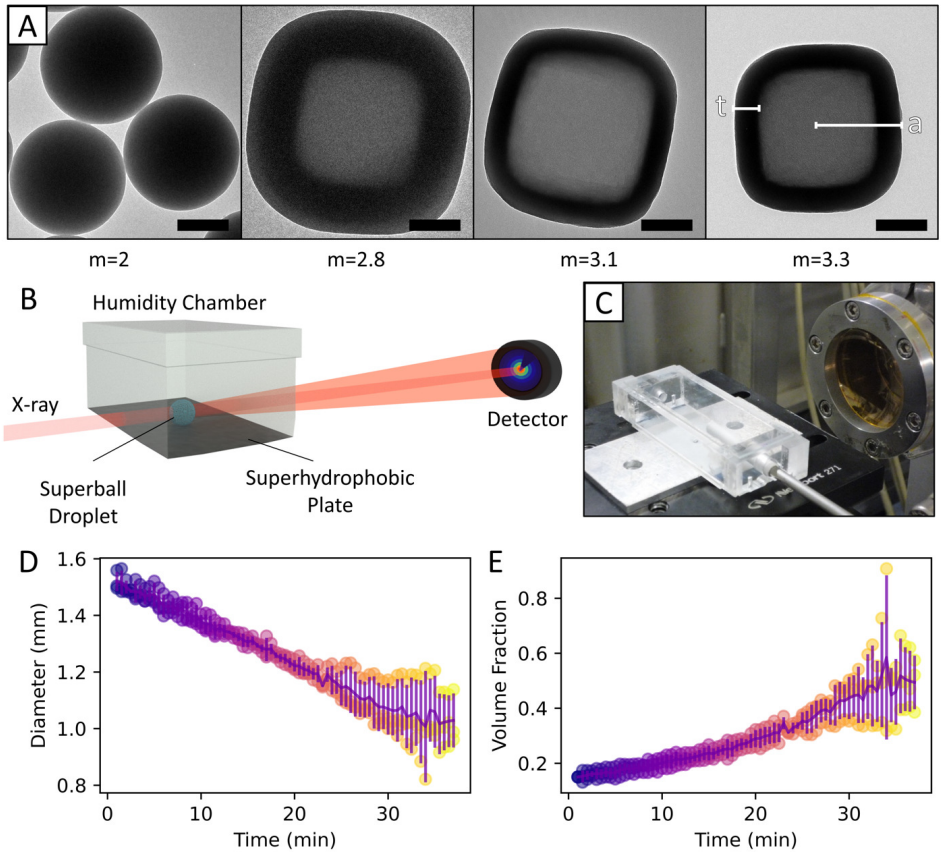


Figure 2.1: (A) Transmission electron microscopy images of a solid silica sphere and hollow silica superballs with different shape parameters, m, shell thicknesses, t, and radii, a. Scale bars are 200 nm. (B) Schematic representation of the in-situ SAXS setup. A dispersion droplet on a superhydrophobic surface is placed inside a humidity chamber. Scattered x-rays are collected on a 2D detector with a wedge-shaped beam-stop. (C) A photograph of the custom humidity chamber with hydrophobic plate aligned with the X-ray path for SAXS measurements. (D) Average droplet size over time for six droplets drying inside the humidity chamber under a microscope camera (purple line) with the standard deviation as the error overlayed with the individual time points of the varying droplets. (F) The the expected volume fraction of superball particles when starting from a 15 vol% droplet calculated from the droplet diameter.

2.3. Results

To study the self-assembly process of superball particles, we synthesized four samples of hollow silica superballs. We note that superballs are a family of shapes defined by

$$\left|\frac{x}{a}\right|^m + \left|\frac{y}{a}\right|^m + \left|\frac{z}{a}\right|^m \geq 1 \tag{2.1}$$

where a is $\frac{1}{2}$ the distance between two opposite faces, and m is the shape parameter defining the roundness of the particles where $m = 2$ is a sphere which becomes more cubic as $m \to \infty$ [62, 83]. To create superballs with a range of m values, we coat hematite superball seeds in silica where increasing the silica shell thickness, t, decreases the resulting m values making the particles more spherical [69]. The hematite seeds are etched away through the porous silica superball shell (Figure 2.1 A). For example, $m = 2.6$ particles have shells of $t = 120$ nm and particle sizes of $2 \cdot a = 1240$ nm with a size dispersity of 4%. A table of all sample parameters is provided in section 2.2. For particles with $m = 2$ (spheres), we grew two sets of silica particles without a template which resulted in solid silica spheres with radii of $r = 206$ nm and $r = 233$ nm [78]. We fabricate assemblies of colloidal superballs by drying 1.5 μL dispersion droplets of 15 vol% superballs in MiliQ water on the surface of a superhydrophobic substrate. We add small pinning positions to the surface of the substrate with a needle tip to prevent droplet rolling. These types of dispersion droplets dry via diffusion of the water vapor into the air [57].

To investigate how the structure assembles under spherical confinement, we performed in-situ SAXS measurements on a series of drying dispersion droplets where each contained different m valued superballs, as schematically shown in Figure 2.1 B. To control the evaporation rate throughout experiments, droplets were dried at ~64% relative humidity in a custom-made chamber (Figure 2.1 C). As water evaporates, the droplet contracts from the initial diameter of 1.5 – 2 mm to ~ 1 mm (Figure 2.1 D-E) and eventually yields a closed-packed assembly which is apparent from the rise in iridescent colors resulting from the Bragg scattering of light as seen in Figure 2.2 A[50, 52]. The synchrotron X-ray beam, of width 500 μm, passed through approximately the center of each droplet, and 2D images were recorded every ~ 4 seconds by the high-resolution 2D X-ray detector for 30-35 minutes as the droplet dried. From the 2D images, the 1D radially averaged scattering profiles were extracted. A typical set of scattering profiles collected in time during the droplet drying process for superballs, with $m = 2.6$, is displayed in Figure 2.2 B. Time resolved scattering profiles for all investigated droplets are displayed in Figure 2.3 A-F.

Generally, the scattering intensity, $I(q)$, from a collection of discrete particles is dependent on the form factor, $P(q)$, and the structure factor, $S(q)$. $P(q)$ arises from the particles' shape and size, while $S(q)$ arises from the particles' organization. The total scattering intensity, $I(q)$, for superball particles can be approximated by the $I(q)$ for mono-disperse spherical particles [68, 84]. In this approximation:

$$I(q) \propto \phi_{part} \cdot P(q) \cdot S(q) \tag{2.2}$$

where ϕ_{part} is the particle volume fraction [33]. In addition, the overall droplet drying process can be monitored via the normalized scattering power, Q^*, which is defined by:

$$Q^* = Q/Q_{max} \propto \Delta\rho \cdot \phi_{SB}(1 - \phi_{SB}) \tag{2.3}$$

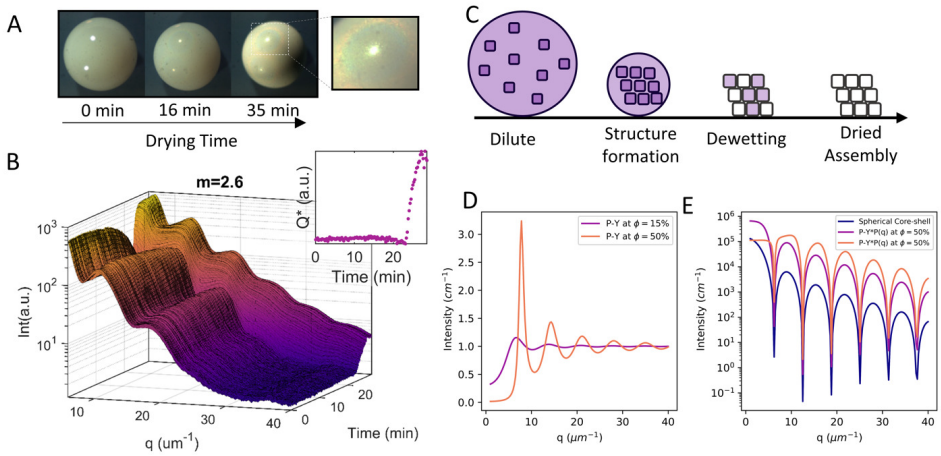


Figure 2.2: (A) A time sequence of an evaporating droplet of 3 μL containing superballs with $m = 3.1$ collected with a digital camera. The droplets have a radius of approximately 1-2 mm. (B) Time-resolved radially-averaged SAXS profiles of the drying process of a droplet containing superballs with $m = 2.6$ at 15 vol%. The inset shows the normalized scattering power Q^* during the drying process. (C) A schematic representation of the different observed stages of drying: Dilute (non-interacting), structure formation, dewetting, and the final dried assembly. (D) The calculated Percus-Yevick structure factor at a particle volume fraction of $\phi = 15\%$ (purple line) and at $\phi = 50\%$ (orange line). (E) The calculated Percus-Yevick structure factor at a particle volume fraction of $\phi = 15\%$ and at $\phi = 50\%$ coupled with a model spherical core-shell P(q) (blue line).

where

$$Q = \int_0^\infty q^2 \cdot I(q) dq \tag{2.4}$$

is the Porod invariant, Q_{max} is the maximum Q value, ϕ_{SB} is the volume fraction of superballs, and $\Delta\rho$ is the scattering length density (SLD) which arises from the difference in electron density between the particle and surrounding medium [72].

Throughout the droplet drying process, we observe four distinct regimes in the intensity, $I(q)$, patterns as shown schematically in Figure 2.2 C. Initially, the superball particles in the droplet are in a dilute, non-interacting, fluid state where we can assume that $S(q) \approx 1$ and that $P(q)$ dominates the scattering profile. We note that we assume $S(q) \approx 1$ in the observed experimental q region due to the lack of additional long range effects from the superballs because we consider the superballs to be hard particles [65]. We check this assumption via the Percus-Yevick $S(q)$ for our initial particle volume fraction, $\phi_{SB} = 15$ vol%, compared to a much higher volume fraction, $\phi_{SB} = 50$ vol%, as shown in Figure 2.2 D. When the Percus-Yevick $S(q)$ is coupled with a model P(q), we can observe the expected influence on the I(q). In this regard, we use the P(q) for a core-shell sphere with a diameter of 1 μm defined by:

$$P(q) = [\frac{3}{V_s}(V_c(\rho_c - \rho_s)\frac{\sin qr_c - qr_c \cos qr_c}{(qr_c)^3} + V_s(\rho_s - \rho_{solv})\frac{\sin qr_s - qr_s \cos qr_s}{(qr_s)^3})] \tag{2.5}$$

where V_s is the volume of the shell and core, V_c is the volume of the core, r_s is the radius of the particle, r_c is the radius of the core, ρ_s is the scattering length density (SLD) of the

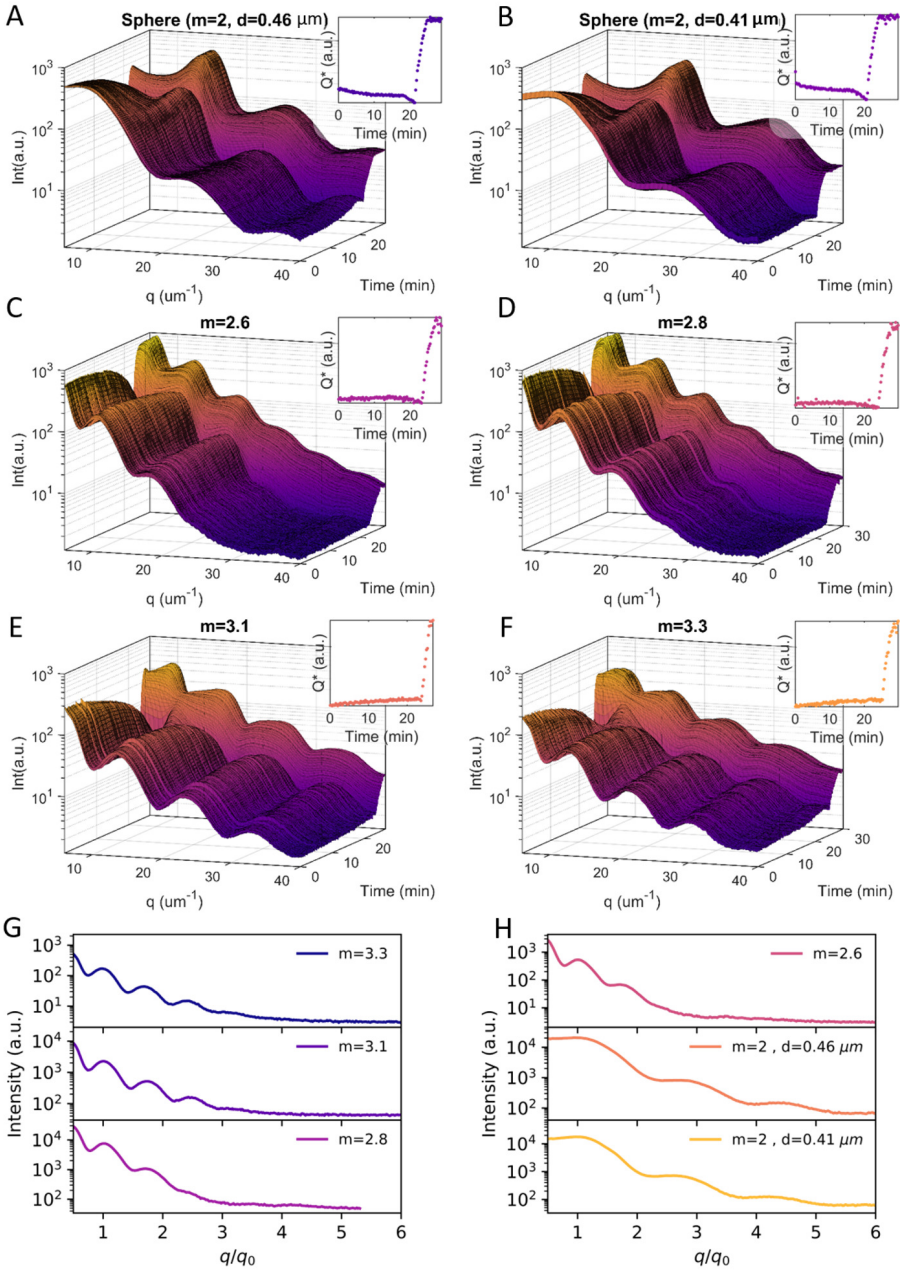


Figure 2.3: Time resolved scattering profiles of all experiments. Solid silica sphere samples (A) S1 and (B) S2 where $m = 2$. Hollow silica superball samples (C) HSB1 where $m = 2.6$, (D) HSB2 where $m = 2.8$, (E) HSB3 where $m = 3.1$, and (F) HSB4 where $m = 3.3$ for the whole-time range. The insets depict the normalized scattering power, Q*, that corresponds with the experimental scattering profiles. (G-H) Extracted form factor for hollow silica superball, where $m = 3.3, 3.1, 2.8$, and 2.6, and solid silica sphere, where $m = 2$ and $d = 0.46$ and 0.41 μm^{-1} experiments.

core, ρ_s is the SLD of the shell, and ρ_{solv} is the SLD of the solvent. From the curves shown in Figure 2.2 E, we can conclude, that even though two small S(q) peaks appear around $q = 3.5$ and 6 μm^{-1}, the influence on the overall I(q) is negligible for the experimentally accessible q-region of $q = 7 - 40$ μm^{-1}.

During the first drying period, the evaporation and confinement do not influence the system, which is evident from the limited changes in the patterns and the little variation in Q^*. As water evaporates from the droplet, the confining volume decreases, and the concentration of particles increases. As a result, inter-particle interactions arise, leading to $S(q) \neq 1$, and $S(q)$ peaks start to appear in the $I(q)$ profiles indicating structure formation. Near the final stage of drying, dewetting occurs where the remaining water inside and outside the particles evaporates, and the surrounding medium of the particles becomes air. This change of medium from water to air dramatically increases the difference between SLDs of the colloids and the surrounding medium, $\Delta\rho$. This step in the drying process leads to a change in the overall intensity of the 1D profiles and appears as a rapid increase in Q^*. Therefore, we utilize the inflection point of Q^* to determine the beginning of dewetting (see inset in Figure 2.2 B). For all investigated superballs and their droplets, dewetting began at similar times (at 24.1 minutes for $m = 2.6$, at 21.7 minutes for $m = 2.8$, 3.1, and 3.3, and at 22.9 minutes for both $m = 2$ containing samples). Discrepancies between dewetting times are likely due to the $2 - 5$ minute time variation in placing the droplet and beginning the SAXS measurements. Eventually, all of the remaining water in the system evaporates and only the dried assembly of particles remains. When the dried assembly is formed, the 1D profiles and Q^* plateau. During the SAXS measurements, not all investigated droplets formed a dried assembly as seen from the insets of Figure 2.3.

Before characterizing the full drying process, we first characterize the particles in the initial, dilute state where $P(q)$ dominates the scattering profile. $P(q)$ was determined to be the initial free particle scattering profiles when $t = 0$, $I_{t=0}(q)$ and is shown for all investigated particle shapes with $2 \leq m \leq 3.3$ in Figure 2.3 G-H. As is well known for hollow spherical shells, the P(q) of a hollow object will be dependent on the details of the shell thickness and the contrast between the solvent, shell, and core [85]. In the case of hollow superballs, the P(q) is determined by the superball shell thicknesses (t), inner shape (m_{inner}), and outer shape (m_{outer}) parameters [68]. The slight variations visible between the $P(q)$ of the different hollow superballs seen in Figure 2.3 G-H can be attributed due to these differing parameters. In addition, it is clear that the $P(q)$ minima are not very distinct, which we attributed to a small size dispersity ($3 - 5\%$) of the particles [86]. It is important to note, for drying hollow superballs, using $I_{t=0}(q)$ as $P(q)$ is only valid when all the particles' cores match the surrounding medium's electron density. When dewetting occurs, particle cores do not empty at the same time and $P(q) \neq I_{t=0}(q)$ as shown schematically in Figure 2.2 C.

Additionally, we observe $S(q)$ changes as neighboring particles no longer posses the same SLD. Figure 2.4 depicts the drying process in a 2D system made of a superball monolayer. As the system dries, we can clearly identify the distinct phases we have seen in the SAXS patterns. Initially, in Figure 2.4 A, the monolayer is fully wetted where the particle cores and surrounding medium are water. This creates a defined contrast between the particles' shell and makes them easily visible. As the water in the surrounding medium evaporates, the particles' core remains filled. In Figure 2.4 B, we can no longer visibly see

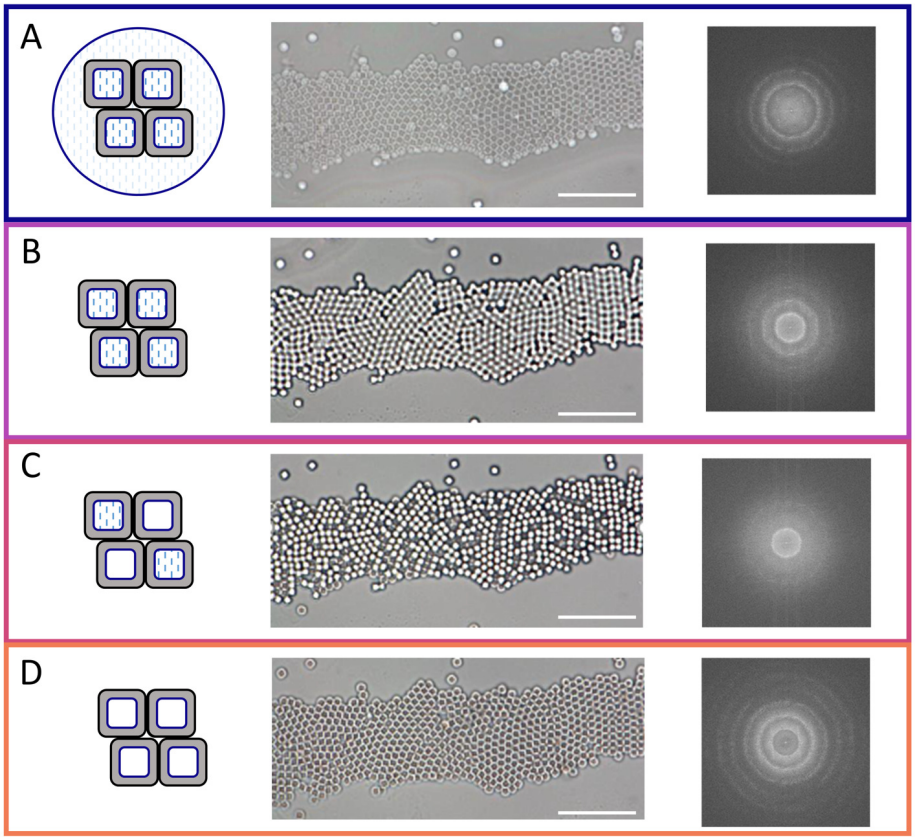


Figure 2.4: Overview of the drying process directly visualized by optical microscopy. For each stage, a schematic, optical microscopy image, and corresponding fast Fourier transform (FFT) image is provided for the (A) fully wetted monolayer, (B) onset of dewetting, (C) superball dewetting, and (D) fully dry monolayer. Scale bars correspond to 10 μm.

the shell, but rather the entire particle. When the water empties out (Figure 2.4 C), we see how each individual particle changes rather than all at once. Eventually, all of the water empties from the superball cores and we have a better contrast in the images due to the complete change in medium (Figure 2.4 D). We collected Fourier transforms (FFT) of the monolayers for each phase of dewetting. By directly observing and radially averaging them, we can see how each phase changes. For the fully wet and fully dry monolayer, Figure 2.4 A and D respectively, the patterns are remarkable similar to each other and are mostly dominated by the $P(q)$ peaks. As the cubes dewet, Figure 2.4 B and C, we see the patterns change where $P(q)$ completely disappears as the particles empty, and there is only a small contribution from the $S(q)$ peaks. By visualizing a simpler system, we better identify how the changing contrast and environment relates to changes in the SAXS patterns even though the physical structure does not change further.

We can visualize the drying process by examining the 2D scattering images as done in

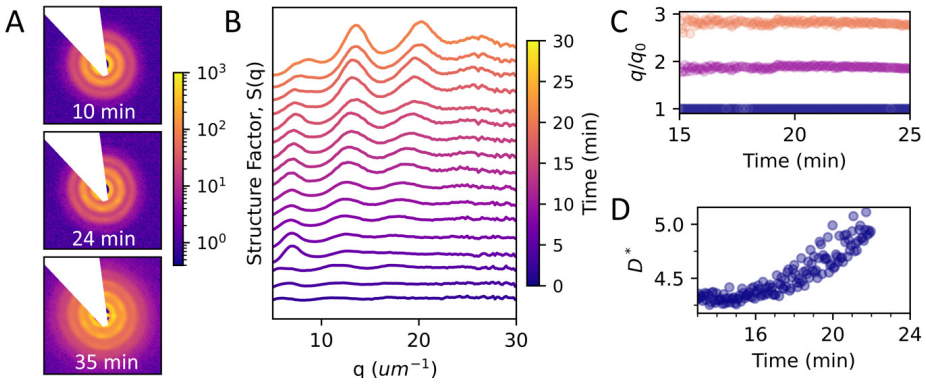


Figure 2.5: Structural evolution for a drying droplet containing superballs with $m = 2.6$. (A) Selected 2D SAXS patterns showing the rise of Bragg peaks during drying. (B) Selected $S(q)$ curves extracted until the dewetting phase. (C) The ratio of peak positions to the first peak location (q/q_0) at selected times. (D) The average crystallite size normalized to the particle size ($2 \cdot a$) over droplet drying.

Figure 2.5 A for a drying droplet with $m = 2.6$ superballs. Here, we observe isotropic scattering profiles from the fluid until Bragg peaks appear in the first ring after 10 minutes, indicating the formation of crystalline structures. These $S(q)$ peaks are present through the dewetting point ($t = 24.1$ minutes). Compared to distinct single crystalline 2D SAXS patterns observed for 3D superball sediments [68, 87], the radial width of these peaks is larger and the fact that higher order peaks are absent indicate that the resultant structure is poly-crystalline where the domains have only weak orientational correlations with each other. For all investigated superball dispersion droplets, we find similar scattering patterns. Although as m increases, the peaks broaden, and for $m = 3.3$ only isotropic rings can be seen. To further understand the structure formation, we examine the 1D $S(q)$ curves. We can extract $S(q)$ by dividing $I(q)$ with the $P(q) \approx I_{t=0}(q)$ [65] up to the dewetting phase where the patterns start to change dramatically (as discussed above). Figure 2.5 B shows selected $S(q)$ curves for superballs with $m = 2.6$ up to $t = 24.1$ min. It can be seen that three consistent, albeit broad, peaks develop in the curves around $t = 10$ min indicating that structure formation has begun. During drying, all peak positions continuously shift towards higher q values demonstrating decreasing inter-particle distances between the superball particles. After $t = 20$ min, a shoulder emerges from the q_0 peak. To reveal how the structure evolves, we follow the ratio between the peak positions and the first peak, q/q_0 [65, 68]. Peak positions and widths were determined by fitting the peaks with a Voigt function [88]. Figure 2.5 C shows the peak position ratios over time for the $m = 2.6$ superball droplet. The ratio remains relatively constant throughout droplet drying and suggests that no significant phase transitions occur. From the q_0 peak width, the average crystallite size can be calculated using the Scherrer equation [89]. To easily compare the results between different cubes, the average crystallite size, D, is normalized by dividing the superball side length, $(2 \cdot a)$, to find $D^* = \frac{D}{2 \cdot a}$. Figure 2.5 D shows that D^* begins to increase rapidly after 16 minutes as the droplet dries. This indicates that the average crystalline domain grows.

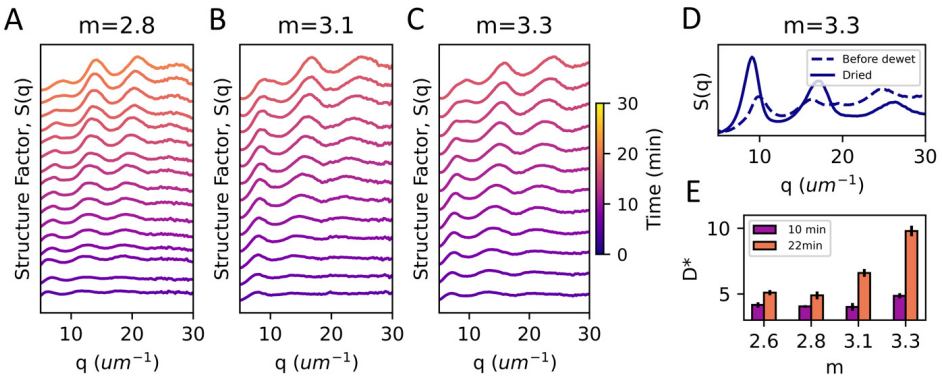


Figure 2.6: Structural evolution of superball dispersion droplets during drying. Selected $S(q)$ curves extracted until the dewetting phase for (A) $m = 2.8$, (B) $m = 3.1$, and (C) $m = 3.3$ with a time-step of 1.2 min between curves starting from $t = 2.6$ minutes. (D) Comparison of $S(q)$ curves from before dewetting (blue, dashed) to the final dried assembly (blue, solid) for $m = 3.3$. (E) The normalized average crystallite size for all superball systems at 10 minutes (purple bars) and 22 minutes (orange bars).

To understand the influence of particle shape during assembly, we explore how $S(q)$ evolves for all dispersion droplets of superballs with $2.6 \leq m \leq 3.3$. Figure 2.6 A-C show the temporal $S(q)$ curves for $m = 2.8$, $m = 3.1$, and $m = 3.3$. In all droplets, we observe a trend similar to $m = 2.6$ where $S(q) > 1$ at $t \approx 7$ minutes. The peak positions shift to higher q values, and a shoulder emerges from the q_0 peak. To confirm that the structure remains after dewetting occurs, we can extract $S(q)$ of a dried assembly and compare to the structure before dewetting by rescaling $P(q)$ [85]. The solid black curve in Figure 2.6 D depicts the structure of the dried assembly and is compared to $S(q)$ before dewetting (dashed black curve). The increase in intensity is due to the change in surrounding medium [85]. Otherwise, there are no significant changes to $S(q)$ after dewetting. Furthermore, we compare the average crystallite size, D^*, over time for all investigated droplets in Figure 2.6 E. As the droplets dry, we observe that the average crystallite size increases for all investigated droplets. Indeed, the average crystallite size at the onset of structure formation ($\approx$ 10 minutes) spans approximately 5 particle diameters for all droplets. At 22 minutes before dewetting occurs, $D^* \approx 5$ particles per crystallite for $m = 2.6$ and $m = 2.8$. Then, D^* increases with the m value where the most cubic-like particle assembly ($m = 3.3$) has $D^* \approx 9.8$ particles per crystallite.

To determine the crystal structures that have formed in the droplets, we first extract $S(q)$ for the spherical particle dispersion droplets just before dewetting (Figure 2.7 A). To compare different dispersions, we re-scaled q of all the $S(q)$ curves by the corresponding q_0 position of the first $S(q)$ peak. In general, spherical colloids do not assemble into pure FCC lattices, but they form a random hexagonal close packed (RCHP) structure that is a mixture of both the FCC and hexagonal close packed (HCP) lattices [90]. Therefore, we compare the $S(q)$ curves from two separate droplets with different solid silica sphere particle radii ($R = 206,233$ nm) to the expected $S(q)$ peaks for FCC (black model lines) and HCP (green lines) in Figure 2.7 A. We find that the spherical assemblies produced similar broad peaks near expected FCC peak positions for the hkl planes 111, 311, 331,

and 440.

In order to confirm that the broad peaks we observe in the S(q) from the spherical particles truly form an FCC lattice. We utilize a model of a para-crystalline FCC lattice, we modify the description from Förster *et al.* for a similar type of structure [91]. In this case, we describe $I(q)$ as follows

$$I(q) \propto P(q) \cdot [1 + (Z(q) - 1) \cdot G(q)] \tag{2.6}$$

where

$$G(q) = \exp\Big(-\frac{q^2\langle u\rangle^2}{3}\Big) \tag{2.7}$$

is the usual Debye-Waller factor with the mean square displacement of the lattice points, $\langle u\rangle^2$, and

$$Z(q) = \sum_{hkl} \frac{2M}{\pi\sigma q^2 q_{hkl}} \exp\Big[-\frac{4(q-q_{hkl})^2}{\pi(\sigma q_{hkl})^2}\Big] \tag{2.8}$$

Here, q_{hkl}, is the reciprocal lattice vector for the hkl reflection, σ is the distortion factor, and M is the multiplicity. For simplicity, we assume there is no Debye-Waller factor, i.e., $G(q) = 1$. In this version, we also assume that the peak width increases for higher q_{hkl} values. For FCC, the reciprocal lattice vector is defined as $q_{hkl} = \frac{2\pi}{a}\sqrt{h^2+k^2+l^2}$. Figure 2.7 B shows this model for one experiment involving spheres (S1 where $r = 0.41$ μm). Since the distortion factor is kept constant ($\sigma = 0.11$), the model differences arises from particle size dispersity.

On the other hand, as the m value increases, we expect that perfect cubic particles pack into simple cubic (SC) lattices [33]. Therefore, in Figure 2.7 C, we compare the curves to the expected $S(q)$ peaks for FCC (black model lines) and SC lattices (gray model lines). For all m, it is clear that the peaks do not perfectly match either the FCC peaks or the SC peaks. Instead as we increase m, we observe a slight shift of peak positions away from q_0. Indeed, simulations and experiments have shown that the equilibrium structure formed by superballs, with $m \geq 2.30$, is a densely packed rhombic crystal lattice, described by the C_1-lattice [62–64, 68].The C_1-lattice is dependent on the superball m parameter and describes a continuous transition from an FCC structure for $m = 2$ to an SC structure for $m \to \infty$ as shown in Figure 2.7 D.

To compare our assembled structures to the C_1-lattice, we calculate how the $S(q)$ peaks evolve as the m values increases. The lattice vectors for the C_1-lattice are defined by Jiao *et al.* [62] as

$$\begin{aligned}
\mathbf{e_1} &= -2(s+2^{-1/m})\mathbf{i} + 2s\mathbf{j} + 2s\mathbf{k} \\
\mathbf{e_2} &= -2s\mathbf{i} + 2s\mathbf{j} + 2(s+2^{-1/m})\mathbf{k} \\
\mathbf{e_3} &= -2s\mathbf{i} + 2(s+2^{-1/m})\mathbf{j} + 2s\mathbf{k}
\end{aligned} \tag{2.9}$$

where s is the smallest positive root of the equation $(s+2^{-1/m})^m + 2s^m - 1 = 0$. The structure varies as m increases by changing the angle, α, between lattice vectors:

$$\alpha = \arccos\frac{\mathbf{e_i}\cdot\mathbf{e_j}}{|\mathbf{e_i}||\mathbf{e_j}|} \tag{2.10}$$

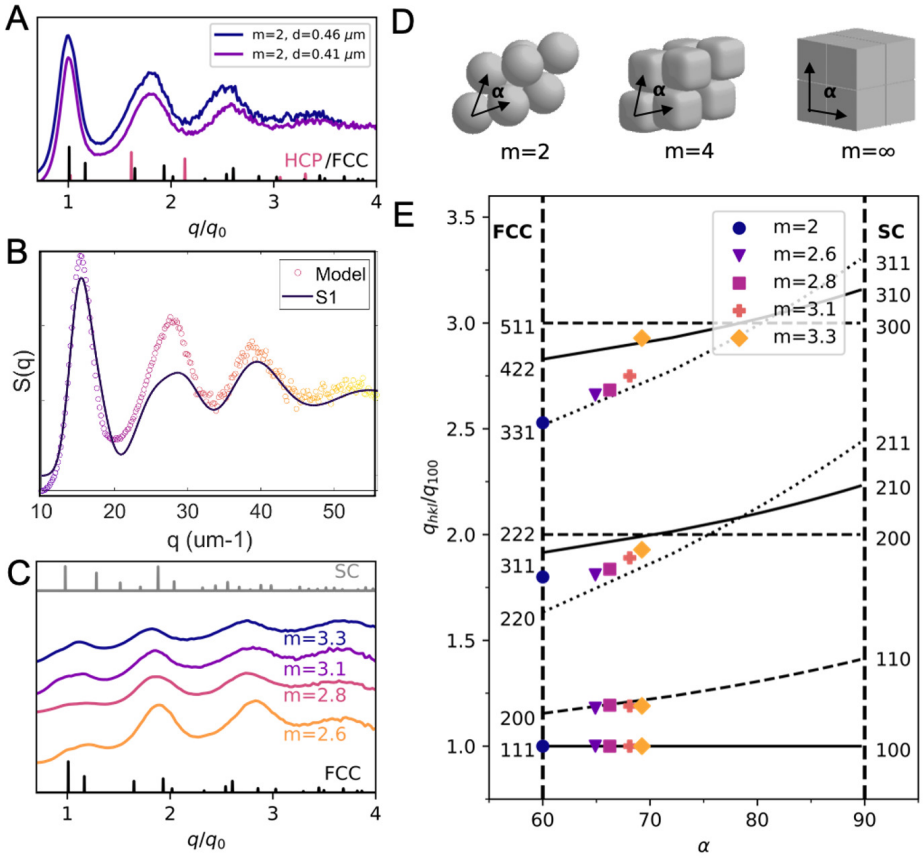


Figure 2.7: Evolution of the structure over m. (A) Stacked plot of extracted structure factors before dewetting for all sphere experiments with model hexagonal closed packed (HCP) and face-centered cubic (FCC) lines. (B) The structure factor for solid silica spheres, S1, before dewettin at 22.8 minutes with the proposed paracrystalline model (solid line) with a distortion factor, $\sigma = 0.11$. (C) Stacked plot of extracted structure factors before dewetting for all superball experiments with model simple-cubic (SC) and face-centered cubic (FCC) lines. (D) Schematic of the angle dependent rhombic structure as the m value transitions from $2 \geq m \geq \infty$. (E) Model lines are plotted of the allowed ratio of the (hkl) diffraction peak position over the angle, α. Experimental values (m=2, 2.6, 2.8, 3.1, and 3.3) of the peak position ratios are overlaid on top (markers).

where $i, j = 1,2,3 (i \neq j)$. It has been shown that when superballs assemble into their densest packing, we can directly map their expected angle, α, from the experimental m value [68]. We note that as m increases from 2 to 3.3, the angle, α, increases from 60° to 69°. Achieving higher angles ($\alpha > 80°$) requires particles with high m values ($m > 10$). Then, we can follow the transition between FCC and SC lattices of the C_1 lattice via the ratio of the diffraction peak position for $60° < \alpha < 90°$. This ratio is defined as

$$\frac{q_{hkl}}{q_{100}} = \Big[\frac{(h^2+k^2+l^2)\sin\alpha^2}{\sin\alpha^2} + \frac{2(hk+kl+lh)(\cos\alpha^2 - \cos\alpha)}{\sin\alpha^2} \Big]^{\frac{1}{2}} \tag{2.11}$$

where q_{hkl} are the peak positions of allowed (hkl) reflections. Figure 2.7 E shows how the ratios of several hkl peak positions are expected evolve according to eq.(1) for angles from $60 \leq \alpha \leq 90$ (lines). The respective FCC and SC hkl values related to the calculated rhombohedral planes are included. Additionally, we overlay the experimental data points (symbols) on top of the lines for comparison. As α increases, the diffraction ratio generally grows for most hkl planes. Higher q value peaks tend to increase more rapidly compared to lower q value peaks. However, that is not the case for all hkl planes such as the horizontal lines associated to the transitions into the SC $h00$ planes. While the experimental values are only available up to $m = 3.3$, corresponding to $\alpha \approx 70$, the peak ratio appears to generally follow the predicted trends. We observe that the emerging peak off of q_0 closely follows the FCC $200 \rightarrow 110$ SC plane transition. Similarly, the higher-order peaks also increase with increasing m.

2.4. Discussion

Our μrad-SAXS results show that the spherical confinement, due to drying dispersion droplets of different superball colloids, leads to the formation of polycrystalline assemblies with their expected rhombohedral C_1-lattice packing [62]. We further find that the average crystalline domain increases with the particles' m value that is particles with a more cubic shape. Our findings are in part in agreement with the results of Wang *et al.* who showed that for small droplets, with ≈2000 cubic nanoparticles, there are short range correlations between the particle positions of dried superball assemblies with low m values, and long-range correlation increases with increasing m [32]. However, in contrast to their study, we do not find the formation of icosahedral clusters for low m as the droplets investigated here are much larger and contain $\approx 2 \times 10^9$ superball particles. In this respect, our results are more in line with studies focusing on droplets with a larger number of particles. For nanocubes with $m > 5$, Agthe *et al.* showed that spherical confinement in a levitating drop leads to polycrystalline domains where domains at the surface were aligned to the droplet interface [33]. For micron-sized spheres, Marin *et al.* showed that droplets on superhydropic surfaces, at high enough particle concentration, will form densely packed structures with many different crystalline domains also aligned to the droplet surface [48]. The reason for this polycrystalline structure is that densification of a droplet leads to multiple nucleation sites when the droplet contains a large number of particles. Interestingly, we did observe the appearance of distinct six-fold Bragg peaks on top of the S(q) ring in the 2D μrad-SAXS patterns of dispersion droplets with $m < 3.3$. This could indicate that while a large part of the surface crystallites are randomly oriented, the center part of the droplet may contain a structure with long-range order, but more investigations are needed to confirm this.

By following the full drying process, we showed that the system densifies and the crystalline structure starts to form as the droplet evaporates. Interestingly, the forming crystal structures did not undergo any phase transitions, which might be expected based on a previous study by Meijer *et al.* who showed that superball colloids, upon slow sedimentation, will first form a rotator FCC crystal before transforming into their densest rhombic packing [68]. Clearly, the current assembly process during spherical confinement occurs via different pathways. We further revealed that a dewetting stage occurs, during which the water evaporates from between and inside the hollow colloids, leading

to the dramatic change in the particle $P(q)$. Since the water does not evaporate from all of the porous hollow colloids at one instant, we do not observe such a significant change for the solid spheres, and this has not been observed for other droplet drying studies of solid particles as well. Thus these hollow particles allowed us to obtain more insight into the local evaporation process as we tracked the changing intensity in $P(q)$ and the corresponding $I(q)$. In addition, strong capillary forces acting on the colloidal particles during dewetting of the droplet, which can reach 10^6 kT, do not lead to rearrangement of the crystalline structures that have formed, as the S(q) before and after dewetting are the same [92].

2.5. Conclusions

In conclusion, we investigated the structural evolution of colloidal superball assemblies during spherical confinement induced by a drying dispersion droplet. The presented results show that the structure of the assembled superballs nucleate into the predicted C_1-lattice. As the droplet evaporates, we found that the structure does not undergo any additional phase transitions throughout drying. The resulting assembly contains several small crystallites that increase in size as the superballs become more cubic-like indicating a polycrystalline structure, and the assembly exhibits optical reflections on its surface. As our understanding of superball assemblies continues to advance, we anticipate that insights into the relationships between the constituent anisotropic particles and resulting assembly's structural color and mechanical properties will arise. It has been shown that by switching from spherical to rod-like particles, dramatic changes in the assembly's structural color can be obtained after spherical confinement [61]. Similarly, particle size and interparticle bonds influence the mechanical properties of the assembly [93]. In chapter 3, we explore how additional magnetic dipole interactions caused by retaining the hematite seed particle influence the assembly under spherical confinement.

Acknowledgements

I would like to express my sincere gratitude to my coauthors, namely Janne-Mieke Meijer, Lucia Baldauf, Peter Schall, Andrei V. Petukho, and Laura Rossi. Their invaluable assistance in conducting the experiments, analyzing the data, and providing guidance and feedback played a pivotal role in the successful publication of this chapter. I would also like to extend our appreciation to the Netherlands Organization for Scientific Research (NWO) for generously providing the beam-time for our research. We are grateful for the financial support granted to Laura Rossi through a VENI grant (680-47-446) and to Janne-Mieke Meijer (016.Veni.192.119) by NWO. Additionally, we acknowledge the support received by Lucia Baldauf through a Studienstiftung des Deutschen Volkes research grant. We are also grateful to the DUBBLE personnel of the European Synchrotron Radiation Facility in Grenoble for assistance with the small angle X-ray scattering experiments.

Chapter 3

Self-assembly of Magnetic Superballs Confined to an Evaporating Droplet

ABSTRACT:

The self-assembly of materials driven by the inherent directionality of the constituent particles is of both practical and fundamental interest. By employing evaporation assisted self-assembly, we form opal-like structures with micro-sized magnetic superball particles. We study the structure formation during evaporation of a dispersion droplet with in-situ small angle x-ray scattering (SAXS) in the presence and absence of an external magnetic field. In the absence of a magnetic field, strong shape-dependent structures form as the water evaporates from the system. Applying a magnetic field to the droplet has a unique effect on the system; strong magnetic fields inhibit the growth of well-ordered assemblies due to the formation of out-of-equilibrium dipolar structures while lower magnetic fields allow particles to rearrange and orient without inhibition. In this chapter, we show how the superball assembly inside a droplet can be controlled by the magnetic field strength and the superball shape. Tuning these interactions provides insights for the controllable formation of macroscopic colloidal assemblies as functional materials.

The data that support the findings of this chapter are openly available in 4TU.ResearchData at 10.4121/4b4b1f8a-b32e-4d6f-974f-991c289925b6, reference number [94].

3.1. Introduction

Designing the structure of colloidal assemblies is a crucial step towards controlled development of novel micro-structured materials and devices. In general, spherical particles assemble into a compact structure through either a face-centered cubic (fcc) or hexagonal close-packed (hcp) arrangement, providing a way to engineer photonic crystals capable of specific functions [95, 96]. As a result, 3D assemblies of isotropic, spherical particles have demonstrated fascinating optical properties, acting as optical waveguides [29] and functioning as long-pass optical filters [50]. We can further explore a rich world of structural diversity by adding anisotropy to the constituent particles, such as a non-spherical shape or an intrinsic directionality via an internal magnetic moment [96–98]. One such anisotropic shape experimentally accessible on the colloidal scale is the superball which is a family of shapes that encompasses the transition from a sphere to a cube via a rounded cube [62]. Superballs have been shown to form a plastic crystal (or rotator) phase prior to their densest packing [68], which is a rhombohedral-like packing that progresses continuously from an fcc lattice (as spheres) to a simple cubic lattice (as perfect cubes) [62–66]. Superballs possessing additional directional anisotropy, such as an internal magnetic moment, can lead to different dense packing. For micron-sized magnetic superballs, Meijer *et al.* [87] showed the presence of hexagonally stacked layers that transform into long-range ordered body-centered monoclinic lattices in the presence of an applied magnetic field for 3D assemblies induced by sedimentation in capillaries. In addition, for paramagnetic nanocubes, Ahniyaz *et al.* [99] showed that an applied magnetic field induced the formation of highly ordered simple-cubic superlattices when assembled by a controlled solvent evaporation method.

The resultant macro- and micro-structure can be further influenced by the employed assembly technique [28]. Specifically, particle confinement within an evaporating droplet is one promising method for creating free-standing colloidal assemblies which can find applications as photonic devices, drug delivery, and magneto-optical materials [100–102]. These droplet-based assemblies are created using either substrate-free processes, such as ultrasonic levitation and emulsification [33, 54, 103], or substrate-based methods like deposition on a superhydrophobic surface [52, 104]. For the latter, the final shape of the assemblies can be varied by modifying the size of the droplet pinning site or the initial particle concentration, resulting in spheres, donuts, and mushrooms [95, 105, 106]. The internal structure of assemblies inside evaporating droplets is dependent on the droplet size and the dispersed particles' properties. For example, spherical particles have been shown to organize into their typical bulk dense packing or form novel icosahedral clusters depending on particle concentration [54–56]. For anisotropic truncated nanocubes, both bulk evaporation and droplet confinement assembly techniques lead to well-ordered fcc lattices [107].

We predict that the combination of anisotropic colloids and confinement induces the formation of more complex self-assembled structures. In the previous chapter, we showed that micron-sized silica superballs assembling inside droplets form expected close-packed structures, albeit poly-crystalline [43]. In this chapter, we increase the complexity of the system by assembling micron-sized superball particles with a magnetic dipole moment in spherical confinement. We utilized *in-situ* synchrotron small-angle x-ray scattering with micro-radian resolution (μrad-SAXS) to investigate the crystallization

process. For dispersions of varying superball shapes, we collected scattering profiles over the droplet height as it evaporates in the absence and presence of an applied magnetic field. Our results show that the combination of confinement and magnetic interactions provides unique control over the final superstructures which is of interest for the fabrication of designer materials as well as photonic structures.

3.2. Methods

Table 3.1: Properties for all particles used within this work. Here, m is the shape parameter, $2a$ is the edge-edge distance of the superball, t is the silica-shell thickness, and t/a is the ratio of shell to particle size.

Name	m	2a (nm)	t (nm)	t/a
Fa3-3	2.8	892	374	0.41
Fa2-2	2.9	799	281	0.35
Fa1-1	3.2	684	166	0.24
Fd4-1	3.5	720	115	0.15
Fc1-1	3.7	895	97	0.11

3.2.1. Particle Synthesis

Hematite cube particles were prepared following the sol-gel procedure [24, 75, 108]. Silica shells were grown on hematite cubes to obtain m-values between 2.8 and 3.7 [67, 76]. The complete particle synthesis procedure to obtain different m values can be found in Ref. [69]. The obtained particles were characterized by transmission electron microscopy (TEM - Philips TECNAI12/20).

3.2.2. Sample Preparation

As-prepared hematite particles were dispersed in Milli-Q water at 0.05 vol%, 15 vol%, and 30 vol%.

Capillary Sample Preparation

Capillary samples for form factor measurements were prepared by dispersing a 0.05 vol% particle dispersion inside a flame-sealed glass capillary. Capillary sediments were prepared by dispersing a 30 vol% particle dispersion inside a glass capillary, flame-sealed, and allowed to sediment for at least 2 days.

Droplet Sample Preparation

Superhydrophobic substrates with contact angles above 160° were prepared as described in chapter 2. Aqueous droplets of 1.5 μL with 15 vol% concentration of superball particles were deposited on superhydrophobic surfaces for drying. A custom-made set-up [87] consisting of permanent magnets was used to apply a magnetic field between $14-35$ mT during the drying process. The droplets were placed in the center of the set-up where the field is uniform.

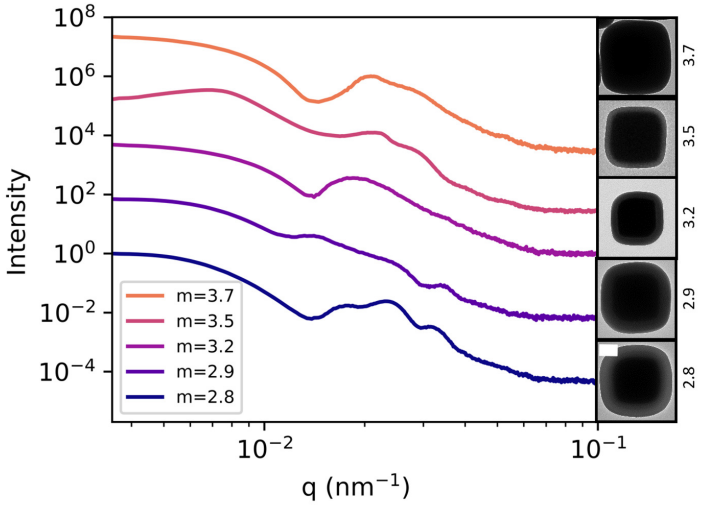


Figure 3.1: Integrated SAXS form factors, P(q), for superball particles with different m-values. Insets for each curve are representative TEM images of superball particles. Scale bar is 200 nm and representative for all insets.

3.2.3. Small Angle X-ray Scattering (SAXS) Measurements

SAXS measurements were conducted at the beamline BM-26B DUBBLE at the European Synchrotron Radiation Facility (ESRF) in Grenoble, France, as described in chapter 2. During these experiments, the incident X-ray beam with a photon energy of 13.96 keV ($\lambda = 0.886$ Å) was focused on a Photonic Science CCD detector with $4,008 \times 2,671$ pixels and a pixel size of 9×9 μm at a distance of 7.87 m. Substrates with the drying droplets were placed horizontally in the X-ray beam. Measurements were performed in the droplets during the full evaporation process at varying heights (z-positions) of 0.1 mm. Background measurements for droplet assemblies were taken with plain water droplets at various heights and for capillary experiments with plain water-filled capillaries. Form factors for superballs were collected from dilute particle dispersions (0.05 vol%) in glass capillaries immediately after preparation.

3.3. Results and Discussion

3.3.1. Superball Properties

In order to prevent superball aggregation due to strong magnetic dipole-dipole attractions and generate a range of m-values, we coat magnetic hematite superball seeds in silica. As we increase the silica shell thickness, t, we decrease the m-value of the superball particles, as seen in the electron microscopy insets in Figure 3.1. For example, superball particles with $m = 2.8$ have silica shells of $t = 374$ nm and edge lengths of $2a = 892$ nm, and particles with $m = 3.7$ have shells of $t = 97$ nm and edge lengths of $2a = 895$ nm (Table 3.1).

To characterize the superball particles' assembly, we use small-angle x-ray scattering (SAXS) with microradian resolution. In general for SAXS measurements, the scattering

intensity, $I(q)$, obtained from a collection of discrete particles is dependent on the form factor, $P(q)$, and the structure factor, $S(q)$. $P(q)$ is determined by the particles' shape and size, and $S(q)$ is determined by the structure that the particles form. Here, we approximate $I(q) \propto \phi_{\text{particle}} \cdot P(q) \cdot S(q)$ where ϕ_{particle} is the particle volume fraction [33]. To determine the structure of assembled superballs, we decouple $S(q)$ from $I(q)$ by obtaining $P(q)$ curves from dilute suspensions (<0.01 wt%) of particles where $S(q) = 1$. Figure 3.1 displays the collected $P(q)$ curves for all investigated particles. For core-shell particles, $P(q)$ depends on the silica shell thickness (t), inner shape (m_{inner}), and outer shape (m_{outer}) [68, 85]. The hematite cores in particles with $m = 2.8$, 2.9, and 3.2 are identical, and the final particle size and shape are mainly determined by the thickness of the silica shell layer. Here, we observed that the size and shape of the hematite core particle strongly affect the overall shape of the $P(q)$, and the silica shell introduces additional oscillations in the $P(q)$ depending on t. When the thickest shell layer is used ($m = 2.8$ and $t = 187$ nm, dark blue curve), we observe several oscillations after the initial valley, which is due to a stronger contribution of the silica shell to the form factor. On the other hand, for the same hematite core particle with a thinner shell ($m = 3.2$), we observe more uniform $P(q)$ peaks initially due to a larger contribution from the hematite core particle. These small differences between particles results in large variations of the $P(q)$ and highlight the importance of collecting sample specific form factors for complex anisotropic systems.

3.3.2. Effect of Droplet Confinement

To investigate the structure formation and drying process of assembling superballs in dispersion droplets, we conducted *in-situ* SAXS measurements, tracking the scattering patterns at different heights within the droplet. As water evaporates from the droplet, iridescent colors arise on the surface of the assembly due to the Bragg scattering of light indicating the formation of close-packed structures [50, 52] as shown in Figure 3.2 and Figure 3.3 A. We note that assemblies formed by this technique may result in a variety of shapes, e.g., spheres, donuts, and mushrooms, based on the contact pinning size and the colloidal dispersion concentration [52, 104]. Throughout this work, we aimed to maintain a nearly-spherical shape during drying, but found that some assemblies experienced a slight cavitation as shown in Figure 3.2. Cavitation of evaporating dispersion droplets is attributed to a higher portion of particles assembling close to the droplet interface rather than in the droplet bulk which creates a core-shell-like macroscopic structure. If the assembled shell cannot withstand the critical pressure for cavitation, the assembly will partially collapse forming indented spheres or toroidal shapes [95, 105, 106]. Here, the formation of the shell is attributed to the size of the pinning position on the superhydrophobic surface and the particle concentration where volume concentrations < 15% will form collapsed structures [53].

In order to follow the internal structure formation of the spherical particle assemblies during drying, we investigate the evaporation of dispersion droplets via *in-situ* SAXS measurements (Figure 3.3 B-C). With a 500 μm beam size, we collect measurements over the height of the droplet with a 100 μm step size as shown in Figure 3.3 C. During these experiments, we observed three main height regions where there was (i) scattering from the air, z_{air}, (ii) scattering from the dispersion droplet, z_{droplet}, and (iii) scattering due

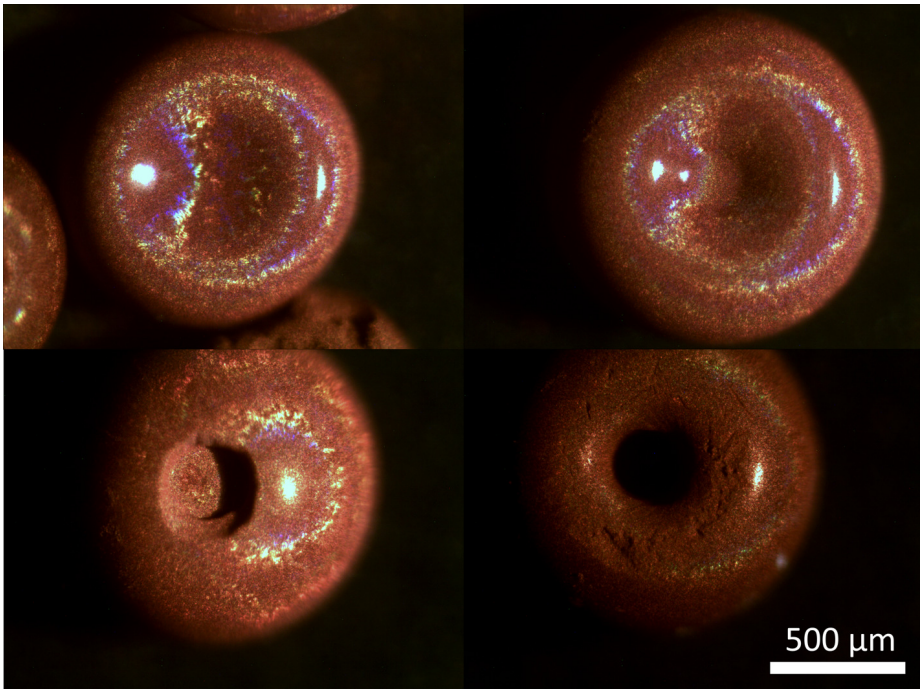


Figure 3.2: Optical microscopy images of recovered assemblies showing possible cavitation. In general, cavitation occurred as an indent on the surface, with two extreme cases shown in the bottom panels, where cavitation formed a deeper hole/donut.

to the superhydrophobic substrate, $z_{\text{substrate}}$. To analyze the overall drying process, we track the change in droplet height as it evaporates by following the position of z_{air}. Scattering from the substrate appears around 4 steps above the substrate due to the beam size being larger than the step size, as demonstrated by significant vertical flares and low intensity values in the 2D SAXS pattern. For simplicity, we have denoted $z = 0$ to correspond to the height immediately above the substrate ($z_{\text{substrate}}$). The typical evolution of the 2D SAXS patterns as a function of z-height and time for a drying dispersion droplet containing magnetic superball particles with $m = 2.8$ is shown in Figure 3.3 D for a dispersion droplet containing magnetic superball particles where $m = 2.8$. At $z = 0.5$ mm, scattering is no longer observed after 15 min as the droplet has shrunk by 0.4 mm, which agrees well with optical microscopy observations (Figure 3.3 A). At $z = 0.3$ mm in the 2D pattern, only $P(q)$ features in the form of distinct rings are present at short times (< 20 min), indicating that the dispersion is still quite dilute. After 20min, these 2D patterns undergo a transformation, and a distinct inner ring with several peaks appears. This ring and peaks represent $S(q)$ features, indicating the formation of denser particle structures in the droplet. At $z = 0.1$ mm, $P(q)$ and $S(q)$ features are already present after 15 min. Additionally, the average $I(q)$ intensity at $z = 0.1$ mm is higher because the beam completely hits the droplet, leading to a larger probed particle concentration [72], compared to near the top of the droplet where it interacts with both the droplet and the air above,

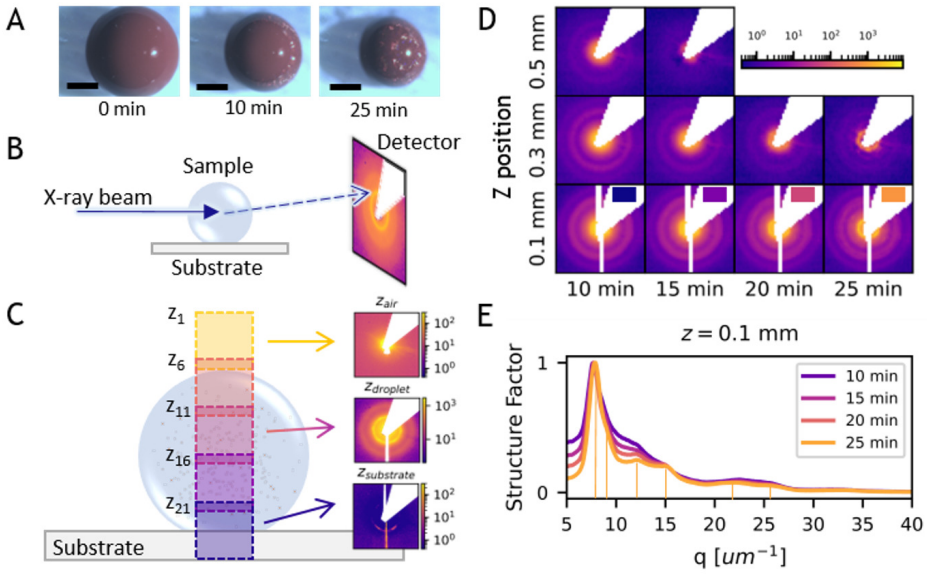


Figure 3.3: (A) Optical microscopy images of an evaporating dispersion droplet with $m = 2.8$ hematite superball particles on a superhydrophobic surface. Scale bars are 500 μm. (B) General schematic of the experimental SAXS configuration. (C) Sample-view schematic of the x-ray beam path over the droplet height. Insets are example 2D SAXS patterns at varying heights: z_{air}, z_{droplet}, and $z_{\text{substrate}}$. (D) Selected 2D SAXS patterns over the droplet height, z-position, and drying time for a dispersion droplet of $m = 2.8$ superball particles. (E) Extracted S(q) curves over drying time at a droplet height of 0.1 mm for the same particles. Line colors are matched to their respective 2D SAXS curves in (D).

potentially causing flares due to scattering at the droplet edge.

To further analyze the $S(q)$ peaks, we extracted the 1D $S(q)$ curves by taking the radial average of the 2D images, $I(q)$, and dividing by $P(q)$. Figure 3.3 E displays selected $S(q)$ curves over time for $z = 0.3$ mm, where the evolution into several well-defined peaks, indicated by the vertical orange lines above the x-axis, is clearly visible. We fit the peak positions and widths with a pseudo-Voigt function [88] and obtained peak positions for the first four main peaks. After a drying time of 25 minutes, the peak positions were located at 7.87, 9.08, 12.73, and 15.14 μm^{-1}. These final positions are the same at the lower part of the droplet, specifically at $z = 0.1$ mm, as shown in Figure 3.3 F. These positions are similar (within ± 0.01) to those expected for an fcc-like lattice, where the ratios of the first four peak positions to the first peak are 1, 1.15, 1.63, and 1.91. From our analysis we conclude that the superballs assemble into different fcc grains that are randomly oriented throughout the bulk of the droplet as well as on the surface. This result is consistent with the findings of Agthe *et al.* [33], who demonstrated that the assembly of magnetic nano-cubes in a droplet resulted in a polycrystalline structure, with alignment near the droplet surface and randomly oriented clusters throughout the bulk. Our *in-situ* SAXS investigations of the drying droplets of superballs shows that we can obtain a detailed understanding of the evolution of droplet size and the formation of the superball

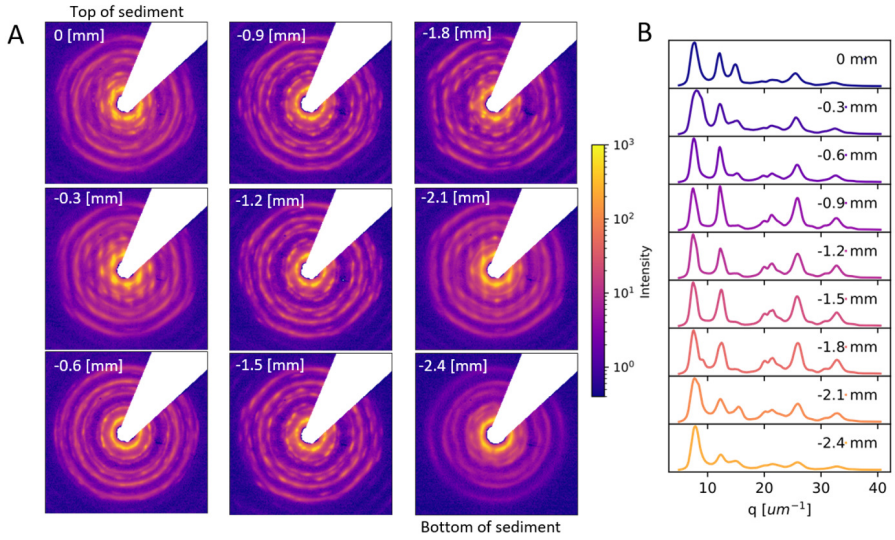


Figure 3.4: Study of 3D capillary sediments of $m = 2.8$ magnetic superball particles. (A) Series of representative 2D SAXS images taken throughout the height of the capillary sediment. (B) Extracted 1D curves of the radially average structure factor, S(q), at selected sediment heights.

structures.

3.3.3. Effect of Superball Shape in Capillary Sediments

In order to detect the influence of confinement on the resultant structure, we sediment samples of particles where $m = 2.8$, 3.2, and 3.7. Previously, we found that the assembly of non-magnetic superballs in evaporating droplets form their predicted close-packed, albeit paracrystalline, rhombohedral lattices [43]. This result matched closely to a study by Meijer *et al.* [68] where 3D capillary sediments of non-magnetic superballs would also nucleate into their predicted close-packed rhombohedral crystals. In this regard, we expect similarities in the close-packed structures that arise between these two types of assembly methods for the magnetic superballs. Meijer *et al.* [87] have shown that magnetic superballs form a brick-wall-like stacking of the rhombohedral structure dependent on the particle shape and height of the sediment.

We show the obtained structure in the droplets to 3D capillary sediments for superballs of $m = 2.8$, 3.2, and 3.7 in Figure 3.4, 3.5, and 3.6. While the 2D SAXS patterns throughout the capillary sediments are more structurally robust, the extracted 1D S(q) curves for $m = 2.8$ near the top and bottom of the capillary sediments correspond well to the S(q) curves obtained from droplet-based assemblies, albeit with a shift to slightly lower peak positions. For example, the first peak position of the droplet-based assembly is $q_{1,\text{droplet}} = 7.87$ μm where in the capillary sediment it is $q_{1,\text{capillary}} = 7.367$ this observed shift correlates to smaller inter-particle spacing between particles inside the droplet where $d_{\text{droplet}} = 0.79$ μm and $d_{\text{capillary}} = 0.85$ μm for assemblies in droplets and capillaries, respectively. One explanation for the decreasing inter-particle spacing inside

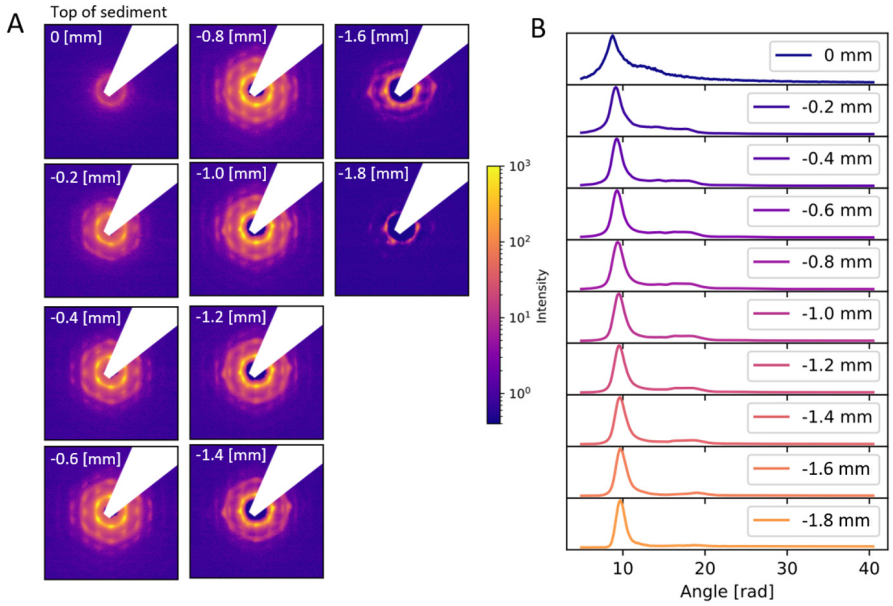


Figure 3.5: Study of 3D capillary sediments of $m = 3.2$ magnetic superball particles. (A) Series of representative 2D SAXS images taken throughout the height of the capillary sediment. (B) Extracted 1D curves of the radially average structure factor, S(q), at selected sediment heights.

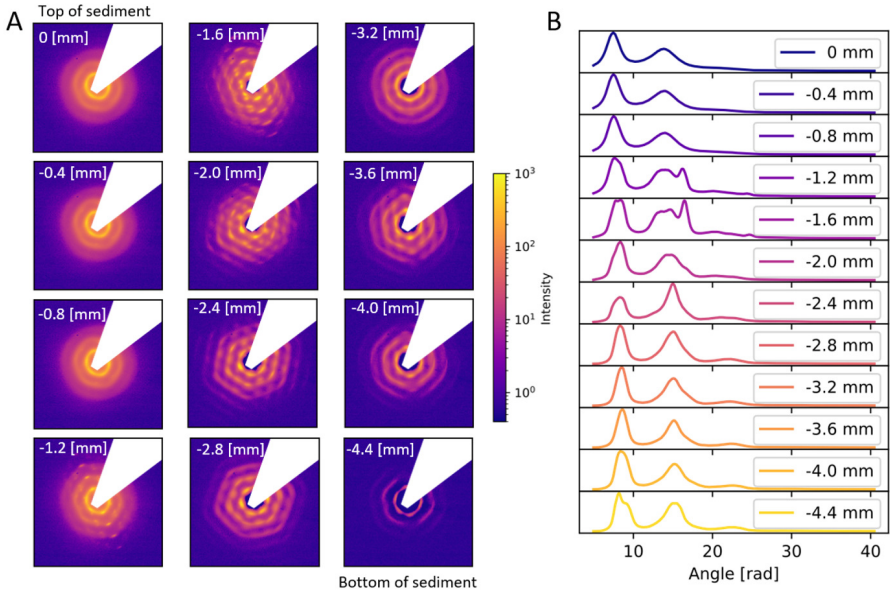


Figure 3.6: Study of 3D capillary sediments of $m = 3.7$ magnetic superball particles. (A) Series of representative 2D SAXS images taken throughout the height of the capillary sediment. (B) Extracted 1D curves of the radially average structure factor, S(q), at selected sediment heights.

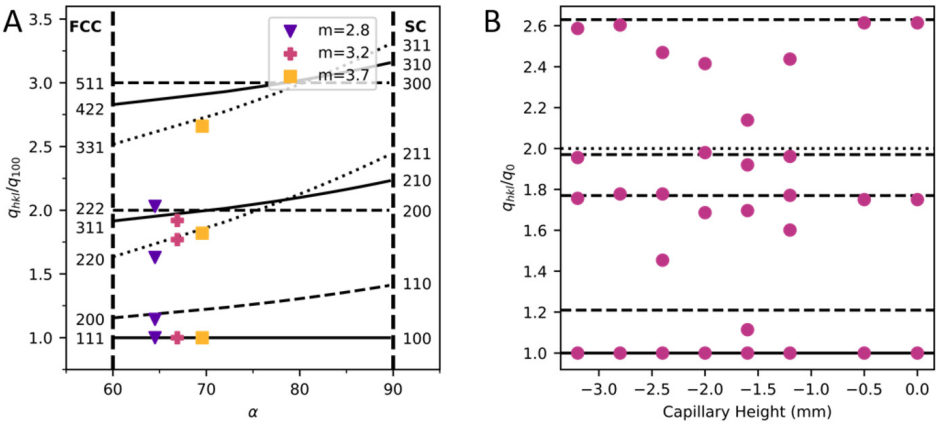


Figure 3.7: (A) Model lines are plotted of the allowed ratio of the (hkl) diffraction peak position over the angle, α, for the predicted C_1 lattice. Experimental values ($m = 2.8$, 3.2, and 3.7) of the peak position ratios extracted from capillary sediments are overlaid on top (markers). (B) Peak position ratios through the capillary sediment of $m = 3.7$ (markers) with the predicted C_1 lattice ratios for that m-value.

the droplet assemblies relates to the strong capillary forces that occur during particle assembly in an evaporating droplet that are not present during assembly via gravitational settling. From the 2D patterns, we observe a hexagonal symmetry indicative of the layered rhombohedral structure [87]. For capillary sediments of $m = 2.8$ and $m = 3.7$, we observe several high order Bragg peaks that cannot be seen in the $m = 3.2$ capillary sediment. This indicates the the particle morphology, such as the m-value and silica shell thickness, affects the order of the structure. One possible explanation related to the m-value is that at lower m the roundness of the superballs allows for more rotational freedom which in turn becomes restricted at higher m until faces of the superballs become flat enough to induce a preferential orientation between themselves and the flat capillary walls. In order to understand the formed structure, we compare the peak positions near the top of the sediment (0 mm) to the predicted close packed rhombohedral superball structures observed in chapter 2, the C_1-lattice. This lattice describes a continuous transition from an fcc structure for $m = 2$ to a simple cubic (SC) structure as $m \to \infty$. The structure can be characterized by the angle α, which transforms from 60 to 90 degrees for fcc and SC, respectively (see Refs. [43, 62, 68] and chapter 2). It has been shown that when superballs assemble into their densest packing, we can directly predict their expected angle, α, from the experimental m value [43, 68]. We note that as m increases from 2.8 to 3.7, we expect the angle, α, to increase from 66° to 71°.

We then plot the ratio of the peak positions to the first peak, q_0, with respect to α, from our capillary sediments to the expected hkl planes. Figure 3.7 A shows the expected q_{hkl}/q_0 ratios calculated from Equation 2.11 overlaid with the measured q_{hkl}/q_0 from the capillary sediments. We observe that the top of the capillary sediment the assemblies correspond well to the predicted C_1 lattice for their corresponding α. However, as we probe lower in the sediment we observe a shift in the ratio of peak positions to the q_0 peak away from the C_1 lattice corresponding to their shape as shown in Figure 3.7 B

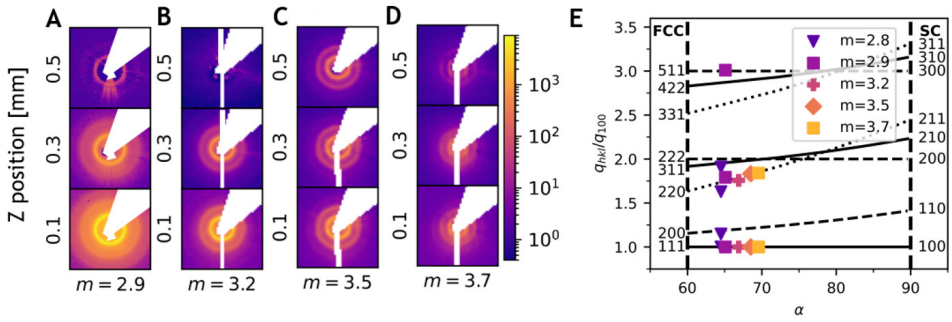


Figure 3.8: Selected 2D SAXS patterns of dried droplet assemblies without an external magnetic field for (A) $m = 2.9$, (B) $m = 3.2$, (C) $m = 3.5$, (D) $m = 3.7$. (E) Model lines are plotted of the allowed ratio of the (hkl) diffraction peak position over the angle, α, for the predicted C_1 lattice. Experimental values (m= 2.8, 2.9, 3.2 3.5, and 3.7) of the peak position ratios are overlaid on top (markers).

for the $m = 3.7$ capillary sediment. This paired with the strong presence of long range Bragg peaks with hexagonal ordering in the 2D plots suggest there a "brick-wall" stacking. Mejier *et al.* [87] have observed similar behavior of superballs in capillary sediments and show that this ordering to due partly to the preferential orientation with the cube face to the flat capillary walls under the higher hydrostatic pressure further into the sediment. Therefore, the top of the capillary sediments better reflect the structures that present inside of evaporating droplets because they are not as driven by this preferential orientation. In this regard, the structures we expect to see for magnetic superballs are closely related to the particle shape.

3.3.4. Effect of Superball Shape

To examine how the shape of superball particles influences the structure formation, we analyzed dispersions consisting of superball particles with varying shapes, specifically with m values of 2.8, 2.9, 3.2, 3.5, and 3.7. Figure 3.8 A-D depict the obtained 2D SAXS patterns from dried dispersion droplets ($\geq$ 25 min) with four of these superballs. Here, we still observed scattering from the different assemblies at 0.5 mm, compared to our $m = 2.8$ assembly, even though the initial vol% is the same. This observation can be attributed to slight differences in the pinning position or the substrate position in the x-ray beam. For $m = 2.9$, the 2D patterns show broad $S(q)$ rings throughout the droplet, except near the top where two nearly vertical peaks are present at $q = 8.82\ \mu m^{-1}$. However, these peaks are partially obscured due to the presence of strong flares related to the scattering from the edges of the droplet. For $m = 3.2$, we observe similar $S(q)$ rings and a difference in the 2D SAXS patterns near the top of the assembly (0.5 mm), where hexagonal symmetry in the $S(q)$ peaks is observed. Further increase in the shape parameter to $m = 3.5$ only reveals strong isotropic $S(q)$ rings throughout the height of the droplet. For our most cubic particles ($m = 3.7$), we observed a slight difference in the $S(q)$ pattern, where it is no longer isotropic but exhibits a slight vertical elongation (Figure 3.8 D). This type of symmetry has also been observed in superball assemblies with higher cubicity ($m >$ 3.5) when they form a brick-wall-like stacking in capillaries [87], suggesting that our

particles are likely adopting a similar structure. Previously, we found that the assembly of non-magnetic superballs in evaporating droplets form their predicted close-packed, albeit paracrystalline, rhombohedral lattices in chapter 2. This result matched closely to a study by Meijer *et al.* [68] where 3D capillary sediments of non-magnetic superballs would also nucleate into their predicted close-packed rhombohedral crystals. In this regard, we expect similarities in the close-packed structures that arise between these two types of assembly methods for the magnetic superballs. For capillary sediments of magnetic superballs, Meijer *et al.* [87] demonstrated the formation of hexagonally stacked layers of superballs, with the specific stacking pattern depending on the shape of the superballs. Within these layers, it was hypothesized that the superballs adopted their predicted densest rhombohedral structures. Since the dried droplet assemblies of the magnetic superballs are polycrystalline, we compare the peak positions near the bottom of the droplet (0.1 mm) to the predicted close-packed rhombohedral superball structures, the C_1-lattice.

By utilizing the ratio of the diffraction peak position, we compared the experimentally measured ratio to the calculated ratio for C_1. Figure 3.8 E provides a comprehensive analysis of the relationship between the observed experimental $S(q)$ peaks (markers) and the predicted C_1 lattice (lines) by examining the $\frac{q_{hkl}}{q_{100}}$ ratio. The second and, if present, third observed peaks in all samples exhibit a close alignment with the predicted lattice, indicating a strong correlation between particle shape and the formation of a rhombohedral lattice. This alignment suggests that the shape of the particles plays a significant role in determining the structure within the assemblies for droplet-based assemblies, rather than relying on magnetic dipole-dipole interactions. A similar behavior was observed for superball clusters (4-9 particles) formed in evaporating emulsion droplets, where both magnetic and nonmagnetic superball clusters with the same geometries exhibited comparable patterns [109, 110]. This observation demonstrates that the assembled structure resulting from spherical confinement over multiple length scales is primarily influenced by particle shape rather than interparticle interactions for this magnetic field strength. Additionally, this highlights the strong relationship between the m-value of the sample and the structures formed by magnetic superballs in evaporating droplets, further emphasizing the importance of particle shape in controlling the droplet-based self-assembly process.

3.3.5. Effect of Magnetic Field on Evaporating Droplets

Due to the presence of a magnetic moment inside the hematite core, we can control the orientation of the superballs and induce the formation of dipolar structures inside the droplets by applying a magnetic field [24]. To investigate the effect of a magnetic field on our assemblies, we applied a uniform field of 35, 26 or 14 mT to drying dispersion droplets of $m = 2.8$ superballs. We observed distinctly different 2D SAXS patterns for the three droplets drying under varying magnetic field strengths. The most notable observation is the appearance of $S(q)$ peaks at the beginning of droplet evaporation. These $S(q)$ peaks exhibit different symmetries corresponding to the different field strengths, ranging from square for $\vec{B} = 14$ mT, to isotropic for $\vec{B} = 26$ mT, and finally to hexagonal for $\vec{B} = 35$ mT (see Figure 3.9 A-C). The presence of diverse peak symmetries at an early stage suggests the formation of different ordered structures.

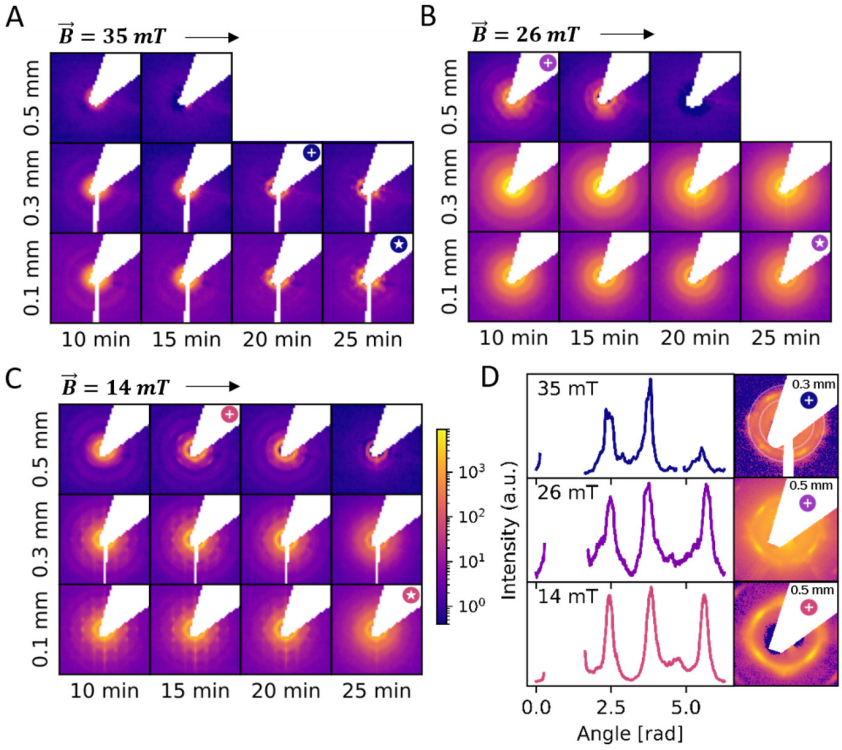


Figure 3.9: Selected 2D SAXS patterns from 10 to 25 minutes of dispersion droplets with $m = 2.8$ superballs under an applied magnetic field of (A) 35 mT, (B) 26 mT, and (C) 14 mT. (D) Azimuthal intensity taken at q_0 for assemblies in varying magnetic fields near the top of the droplet, either 0.3 or 0.5 mm heights. Insets are of 2D SAXS images with a cropped q range to show the q_0 peaks. The extracted plots and insets can be matched to their corresponding 2D SAXS image via the symbol (+) in A, B, and D.

To compare the assembled structures at an early stage (at 10 minutes) under different magnetic fields, we examined the anisotropy within the inner-most $S(q)$ ring at q_0 by analyzing the azimuthal intensity for the corresponding q_0-value. Figure Figure 3.9 D presents a comparison of the azimuthal intensity for the different assemblies' q_0, located at $q = 7.90$, 7.85, and 7.69 μm^{-1} for the $\vec{B} = 14$, 26, and 35 mT assembly, respectively. Interestingly, the q_0 peaks shifts to higher q-values with decreasing field strength, corresponding to a real-space shift from $d_{35\,\mathrm{mT}} = 0.83$ to $d_{14\,\mathrm{mT}} = 0.79$ μm. This greater interparticle distance at higher magnetic fields might be related to the formation of superball chains that quickly sediment and jam during assembly, hindering the close-packing of the structure [24, 87]. Notably, we observed consistent 4-fold anisotropy at q_0 across all assemblies, indicating similar local arrangements at the onset of structure formation.

To understand the structure through the height of the droplet dried at 14 mT, we investigate the structure factor at 15 minutes at droplet heights of 0.5 mm and at 0.1 mm. However, due to the presence of anisotropy in the S(q) rings from some of the assemblies,

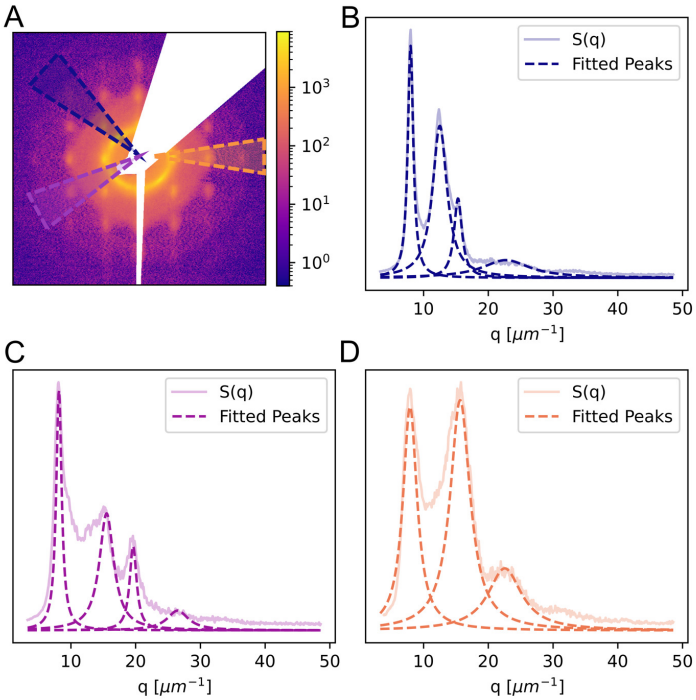


Figure 3.10: Example plots for peak analysis from extracted angular wedges. (A) Displays a 2D SAXS image example that requires the use of angular wedges to collect all peak positions. Three example wedges are displayed via the drawn triangles. (B) The first angular wedge (blue) with peak positions fitted at: q = 8.0, 12.52, 15.33, 22.72 μm^{-1}. (C) The second angular wedge (purple) with peak positions found at: q = 8.16, 15.32, 19.62, 26.5 μm^{-1}. (D) The third angular wedge (orange) with peak positions found at: q = 7.99, 15.36, 22.70 μm^{-1}.

more care needs to be taken to properly find information on the peaks. Therefore, we collect radial averages along different angular wedges where the various peaks lie from which we can extract the actual peak information. Figure 3.10 shows an example where three angular wedges are collected (dark blue, purple, and orange) and the specific peak positions are fitted. Here, we observe different peaks based on the angular wedge we collect indicating strong texture in our samples. In order to properly collect all Bragg reflections, we carefully chose the angular wedges such that all reflections are accounted for.

In Figure 3.11 A, we show the structure factor with the extracted peak positions (as done via various angular wedges). Near the top of the droplet, we identify that the first four most intense peaks correspond well to the structure factor from the assembly at 0.1 mm. Therefore, the overall structure inside the droplet is consistent. Interestingly, the apparent structure observed at 0.1 mm is similar to the base-centered monoclinic (BCM) lattice observed by Meijer *et al.* [87] for 3D capillary sediments of superballs inside a magnetic field. The presence of high-ordered Bragg peaks in the assembly formed under a 14 mT field, allows us to further investigate the resultant structure by rotating the

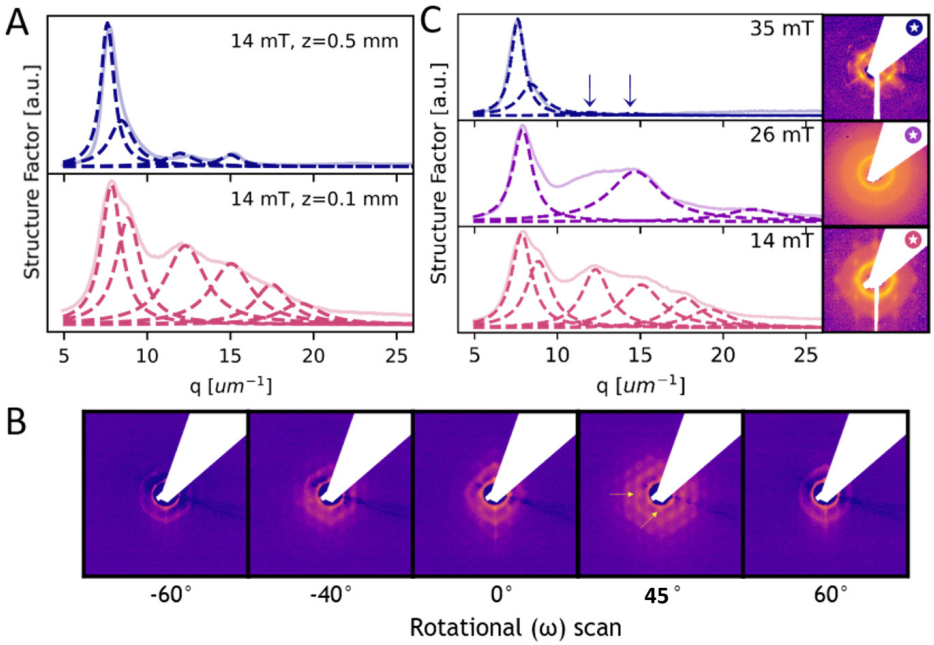


Figure 3.11: (A) Extracted S(q) curves at 15 minutes for the assembly form under a 14 mT magnetic field. The blue curve is taken from the top of the droplet at 0.5 mm (pink +) and the pink curve is from the assembly at 0.1 mm (pink ×) in Figure 3.9 D. Dashed lines correspond to the peak positions collected from various angular wedges. (B) Selected rotational scans of the assembly dried under a 14 mT field at -40^o, 0^o, and 45^o. (C) Extracted S(q) curves at a droplet height of 0.1 mm and 25 minutes for the three assemblies of $m = 2.8$ superballs dried under varying magnetic fields with their corresponding 2D SAXS image as an insert.

sample from −60° to +60°. Figure 3.11 B shows selected 2D SAXS patterns of −60°, −40 °, 0°, +45°and +60°. Here, Bragg spots exhibiting square symmetry are visible, suggesting the presence of a crystal lattice with cubic characteristics. Previously, for 3D capillary sediments, magnetic superballs under a magnetic field assembled into a body-centered monoclinic (BCM) lattice [24, 87]. We observe clearly the [100] projections of the BCM lattice at $\omega = +45°$ and $-40°$ dictating a rotation of 85°. We determine the additional lattice parameters for the BCM lattice by tracking the position of the horizontal and vertical peak positions. The horizontal peaks in the [100] projections at $\omega = +40°$ and $-40°$ are $q = 12.79\ \mu m^{-1}$ and $q = 12.63\ \mu m^{-1}$, respectively. The vertical peaks present in all rotations is located at $q = 7.89\ \mu m^{-1}$. Then, the resulting lattice parameters for the BCM lattice are $a = 0.99\ \mu$m, $b = 0.98\ \mu$m, and $c = 1.52\ \mu$m where $\alpha = \beta = 90^o$ and $\gamma = 80^o$. In the presence of very low magnetic fields the assembly of particles into a body-centered monoclinic (BCM) lattice occurs while higher field strengths hinder its development. It is clear that there is a delicate balance between the strength of the magnetic attraction and the rate of aggregation. If the attraction is too strong, particles agglomerate quickly without re-orientation, resulting in dense deposits. Surprisingly, the confinement of the droplet has no effect on the creation of the BCM lattice, further emphasizing the com-

plex interplay between magnetic field strength and particle interactions throughout the self-assembly process.

Figure 3.11 C displays the radial averages (solid lines) with the extracted peaks (dashed lines) for all assemblies at 25 minutes and 0.1 mm droplet height. Here, the number of identified peaks varies between different assemblies, from 6 peaks at 14 mT to 4 peaks at 35 mT and 26 mT. Although the structure factor at 26 mT is limited due to the broad peak sizes, we can compare nearly 1:1 the peak positions collected at 35 mT to 14 mT (see Table 3.2), which indicates that the overall structure of the two assemblies inside the high and low magnetic field remains relatively consistent. Additionally, we observe an increase in crystallinity, as evidenced by the presence of higher-order Bragg peaks at lower magnetic fields. This suggests that more particle reorganizations can occur. Similarly, for superparamagnetic truncated nanocubes assembled via solvent evaporation, weak magnetic fields induce the formation of well-ordered 3D mesocrystals [111, 112]. This finding suggests that the applied magnetic field strength can be tuned to control and manipulate the degree of ordering in our assemblies.

Table 3.2: Table of peak positions (q_n) and peak ratios (q_n/q_0) for $m = 2.8$ assemblies under various applied magnetic field after dewetting occurs.

Field	q_0	q_1	q_2	q_3	q_1/q_0	q_2/q_0	q_3/q_0
14 mT	7.85	8.86	12.3	15.05	1.14	1.57	1.92
26 mT	7.9	14.7	21.8	-	1.86	2.76	-
35 mT	7.61	8.65	11.98	14.49	1.14	1.57	1.90

3.3.6. Effect of Superball Shape and an Applied Field

To investigate the relationship between particle shape and structure formation under an applied magnetic field, we evaporated dispersion droplets of varying m-valued superball samples under a magnetic field. For these samples, we utilized either a 26 or 14 mT magnetic field to prevent possible jamming effects observed at higher magnetic fields (as shown earlier in Figure 3.9). Figure 3.12 A-B show the 2D SAXS data at the onset of structure formation (10 minutes) for $m = 2.9$ and $m = 3.2$ superballs throughout the height of the droplet under a 14 mT field. In both cases, we observed similar structural behavior to the $m = 2.8$ superball assembly where the inner S(q) ring contains a 4-fold anisotropy which is located at $q_0 = 8.39\ \mu m^{-1}$ and at $q_0 = 9.71\ \mu m^{-1}$ for assemblies of $m = 2.9$ and $m = 3.2$, respectively. These positions correspond to $d = 0.75\ \mu m$ and $d = 0.65\ \mu m$ which are similar to the characteristic length of the superballs, $2a = 0.79\ \mu m$ and $0.68\ \mu m$ for $m = 2.9$ and 3.2, respectively. Therefore, the difference between these peak positions is attributed to the different sizes of the superball samples at different m-values. At 0 mm, for the $m = 2.9$ assembly, Bragg peaks are faintly visible above the background intensity and located at $q_{1-3} = 9.87$, 13.60, and 17 μm^{-1}. In Table 3.3, we observe a similar symmetry of the apparent Bragg peaks in the $m = 3.2$ assembly at 0 mm. We again compare the structure between the different assemblies by calculating the ratio of the peak positions, q_n, and the first peak position, q_0. For $m = 2.8$, 2.9, and 3.2, the ratios correspond well to each other (within ± 0.02) with values of $q_n/q_0 = 1.15$, 1.6, and 2 indicating that they all form into similar BCM structures highlighted earlier for $m = 2.8$. As we increase the

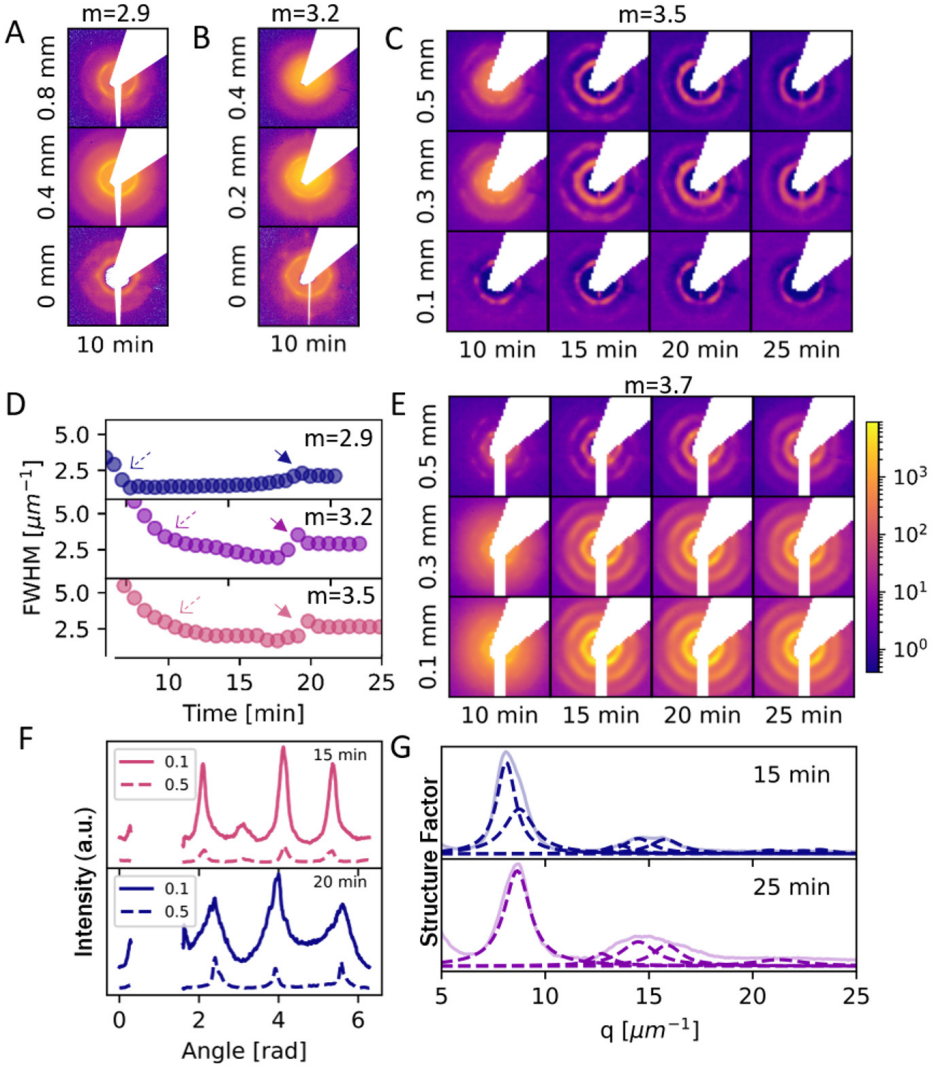


Figure 3.12: Selected 2D SAXS patterns for dispersion droplets of superballs with m-values of 2.9 to 3.7. (A) 2D SAXS patterns at 10 minutes for $m = 2.9$ superballs with an applied field of $\vec{B} = 14$ mT and (B) for a $m = 3.2$ dispersion droplet with an applied field of $\vec{B} = 26$ mT. (C) Patterns over time for $m = 3.5$ at droplet heights of 0.1, 0.3, and 0.5 mm with an applied field of $\vec{B} = 14$ mT. (D) Full width half maximum (FWHM) of the first S(q) peak, q_0, at 0.1 mm droplet heights for assemblies of $m = 2.9$ (blue markers), 3.2 (purple markers), and 3.5 (pink markers). Arrows in each subplot indicate the onset of structure formation (dashed arrow) and the dewetting point (solid arrow). (E) Selected 2D SAXS patterns over the droplet height and time for a dispersion droplet with $m = 3.7$ superballs in an applied magnetic field of 26 mT. (F) Selected azimuthal curves for $m = 3.7$ superballs at heights of 0.1 and 0.5 mm for 15 and 20 minutes. (G) Selected structure factor curves for $m = 3.7$ superballs (solid lines) taken at a droplet height of 0.1 mm before dewetting at 15 minutes and after at 25 minutes with their corresponding fitted peaks found via angular analysis (dashed lines).

Table 3.3: Table of peak positions (q_n) and peak ratios (q_n/q_0) for assemblies under an applied magnetic field before dewetting occurs.

m	**Field (mT)**	**Time (min)**	q_0	q_1	q_2	q_3	q_1/q_0	q_2/q_0	q_3/q_0
2.8	14	27.8	7.85	8.96	12.3	15.55	1.14	1.57	1.98
2.9	14	20.5	8.39	9.73	13.42	16.78	1.16	1.6	2
3.2	26	21.8	9.71	11.17	15.78	19.66	1.15	1.62	2.02
3.5	14	10.8	9.39	10.76	15.79	17.81	1.15	1.68	1.91
3.7	26	22.5	7.93	8.98	14.65	15.38	1.13	1.84	1.93

cubicity of the particles to $m = 3.5$, we observe a different structural behavior as shown in Figure 3.12 C. At the onset of structure formation (between 10 and 15 minutes), radially and azimuthally broad Bragg peaks appear throughout the height of the droplet. This azimuthal spread of the reflections implies there is a slight orientational mismatch between superball particles. After 20 minutes, a transition to rectangular symmetry can be seen throughout the height of the droplet. When dewetting occurs at 25 minutes, broad rings encompass the Bragg peaks indicating that the structure inside partially collapses into a polycrystalline state. Additionally, we tracked the formation of the assembled structure by following the changes in the q_0 peak width. Figure 3.12 D depicts the full width half maximum (FWHM) of the q_0 peak at 0.2 mm for the assemblies in Figure 3.12 A-C. We observed the onset of structure formation (dashed arrows) by a rapid decrease in the FWHM towards a plateau which decreases to 1.5 ± 0.1, 2.3 ± 0.1, and 1.8 ± 0.1 μm^{-1} for assemblies of $m = 2.9$, 3.2, and 3.5, respectively. Immediately afterwards, a sharp, upward spike appears in the plots followed by a smooth secondary plateau. This can be attributed to the dewetting of the assembly which does not undergo anymore structural changes after total evaporation of the water droplet. The observed FWHM can be correlated to the average inverse length of well-ordered particles [89]. Therefore, the increase of the FWHM after dewetting suggests that the dewetting process is slightly disruptive to the structure which is seen for assemblies of superballs where $2.9 \leq m \leq 3.5$ in Figure 3.12 D.

As we move to the most cubic superball, $m = 3.7$, clear Bragg peaks with hexagonal symmetry are seen throughout the droplet at the onset of structure formation, denoted as 10 minutes in Figure 3.12 E. This strong hexagonal symmetry results from the brick-wall-like stacking of the superballs. At 15 minutes, we observe a peak broadening in the azimuthal direction and a decrease in overall intensity throughout the height of the droplet as shown as pink curves in Figure 3.12 F. This indicates that the particles near the top of the droplet are well aligned with each other, but the orientation becomes slightly offset further into the bulk of the droplet [66, 113]. After 20 minutes, the symmetry of the Bragg peaks switches from hexagonal to rectangular throughout the height of the droplet. To further investigate the structure of the $m = 3.7$ superball assembly, we display the structure factor generated from the radial average at $z = 0.1$ mm (solid lines in Figure 3.12 G) before and after dewetting occurs at 15 and 25 minutes, respectively. Dashed lines are collected from fitting peaks taken from the intensity along varying angular wedges. At 15 minutes (blue curves), we obtain several peak positions due to the presence of well-defined Bragg peaks in the 2D pattern. At 25 minutes (purple curves), peak posi-

tions are harder to elucidate directly from the radial average due to the increased peak width radially and azimuthally of the Bragg peaks. However, we find that the peak positions correspond well to the peaks present at 15 minutes with the exception of the peak corresponding to $q = 8.66\ \mu m^{-1}$ at 15 minutes which is not observable at 25 minutes. The overall peak positions after drying paired with the significant difference in the peak ratios for $m = 3.7$ to all other samples(Table 3.3) indicates the presence of a different well-ordered structure. One possible reason for this drastic difference could be due to the decreasing silica shell used to coat the hematite superballs for higher m-values. As the shell decreases, the particles will feel stronger magnetic forces when they come close together as thicker silica shells prevent close contact between the magnetic cores [24, 87]. Therefore, the interplay between the silica shell thickness, particle shape, and magnetic field strength are important considerations when determining the resultant superball assembly structure.

3.4. Conclusions

The self-assembly of magnetic superball particles confined in an evaporating droplet was investigated for a variety of changing parameters including the superball shape, m, and the external magnetic field strength. For micron-sized, silica-coated hematite superballs, we obtain free-standing macrostructures as we tune these two factors. Without an applied magnetic field, we observed the formation of polycrystalline structures with their expected densest rhombohedral symmetry for all m-values. While applying a high magnetic field hindered the assembly of magnetic superballs, at a lower magnetic field of 14 or 26 mT, well-defined symmetries arose at the onset of structure formation. However, well-ordered structures only remained after dewetting for superballs of $m = 2.8$ and 3.7, our roundest and most cubic samples. Our study shows that the shape of colloid particles, the presence of magnetic interactions, and the assembly in a confining droplet are all important parameters that determine the formation of well-ordered structures. Finally, the tunability of these parameters allows for the precise formation of macroscopic colloidal assemblies and holds promising potential for the creation of functional materials with customized properties on a macro-scale, paving the way for future advancements in material design and applications.

Acknowledgments

We would like to thank Andrei Petukov and Janne-Mieke Meijer for assistance during the experiments as well as insights throughout the data analysis. We also thank Max Schelling for assistance with synchrotron experiments. We thank the Netherlands Organization for Scientific Research (NWO) for the provided beam-time. We thank Nick Blankenstein and Lucia Baldauf for the synthesis of various samples used throughout this work. We are also grateful to the DUBBLE personnel of the European Synchrotron Radiation Facility in Grenoble for assistance with the small angle X-ray scattering experiments.

Part II

Active Swimming of Hematite Microparticles

Chapter 4

Enhancing the Active Motion of Hematite Microswimmers by Calcination

ABSTRACT:

The development of autonomous, self-propelled active particles has garnered significant interest due to their potential applications in cargo delivery and environmental remediation, as well as their utility as models for understanding biological systems. However, designing highly active and cost effective microparticles is challenging. On one hand, highly effective swimmers can be produced in small amounts using 2D techniques. On the other hand, large amounts of hematite microparticles can be readily synthesized in a variety of shapes and exhibit photocatalytic behavior necessary for light-driven active motion, but their applications are still limited due to their low efficiency. In this chapter, we investigate how to improve the photocatalytic properties of hematite microparticles by using a general approach that can be applied to a variety of experimental systems. For this approach, we calcine hematite microparticles and measure their activity by tracking the particle motion with optical microscopy. We calculated the mean-squared displacement (MSD) under different conditions and found that increasing the calcination time results in a higher ensemble MSD for the hematite micro-particles. Calcined particles have a maximum 87-fold rise in MSD at 1-minute lag times. This simple, scalable approach makes hematite more accessible to key areas of soft matter and photocatalysis research.

The data that support the findings of this chapter are openly available at reference numbers [114, 115].

4.1. Introduction

Active microswimmers are capable of navigating through complex, three-dimensional environments and have potential implications in drug delivery [35], environmental remediation [36–38], biomedical diagnostics [39], as well as models for collective phenomena [42]. In one category of active microswimmers, they propel themselves due to the phoretic motion derived from the photocataltyic decomposition of a fuel to produce self-generated chemical gradients. One fuel often used is hydrogen peroxide, H_2O_2, whose decomposition into O_2 and H_2O is catalyzed in the presence of illuminated semiconductors [40, 41]. In order for the particle to propel, the self-generated gradients or the particles themselves must be asymmetric [35]. Therefore, numerous methods have been developed to produce active microswimmers with inherent asymmetry. For example, these methods include the preparation of Janus particles [116], which possess photocatalytic properties on one half of the particle, bimetallic rods [117], and porous microparticles [118], all of which are tailored to achieve this desired characteristic. However, the complex synthetic strategies required to prepare these microparticles inhibit both applications and up-scaling. Hematite, as an active swimmer, mitigates this due to its scalability and spontaneous symmetry breaking required for active motion [119, 120]. Hematite active swimmers also play an essential role in dynamic assembly and cargo transport [37, 119, 121, 122] owing to their ability to transition between active and passive behavior when exposed to short ($\lesssim$ 500 nm) wavelengths and they posses a permanent magnetic moment [108].

For photocatalytic activity in general, the semiconductor absorbs photons greater or equal to its band gap, and electrons from the valence band move to the conduction band. This creates a electron-hole (e-h) pair which can either i) recombine or ii) diffuse to the surface and participate in redox reactions with the fuel [123]. Properties of hematite, such as the light penetration depth and e-h recombination time, limit its catalytic activity compared to other active particles, such as TiO_2 or Pt based microswimmers [124]. For example, the light penetration depth of hematite at λ = 550 nm is 118 nm and $\approx$ 20 nm at λ = 395 nm [125]. Whereas, the diffusion length of an e-h pair is only 2-4 nm, and the e-h recombination time is around 2 ps [123]. One possible strategy to mitigate some of hematite's limitations is by particle calcination which is a process where particles are heated to high temperatures, causing them to lose some of their defects and surface impurities to become more homogeneous. For example, calcination is used for TiO_2 active particles to refine the internal crystal phase and increase the internal crystallite size as well as alter the particle size which leads to an enhancement of the particles' photocatalytic properties [126, 127]. For hematite nanorods and nanoparticles in general, this technique has improved hematites' photocatalytic properties in regards to chemical degradation for environmental remediation [128–131]. Additionally, calcined hematite nanoparticles have shown enhanced electrocatalysis when acting as an anode material for lithium-ion batteries [132]. Thus, calcination, a simple step after the synthesis of hematite microparticles, fully enhances hematites' photocatalytic properties without other more intensive solutions, e.g., doping. In this work, we explore the active motion of photocatalytic hematite particles using hydrogen peroxide as a fuel. We present as-prepared hematite microswimmers alongside calcined microswimmers which can be activated by exposure to UV wavelengths. Non-calcined microswimmers preform noticeably worse than all calcined microswimmers with the best preforming microswimmers

reaching an average 87-fold increase in their mean-squared displacements.

4.2. Experimental Methods

4.2.1. Colloid Synthesis

Hematite superballs were prepared from a gel-sol synthesis based on a procedure in Ref. [75]. The specific superball shape is described in Chapter 2. Details on the preparation procedure of hematite colloids can be found in a previous work [67]. Briefly, a 6 M NaOH solution is slowly added to a 2 M aqueous iron chloride solution to form a gel-sol that is aged at 100°C for 8 days.

4.2.2. Particle Calcination

Hematite samples were calcined in a Nabertherm L5/S27 furnace in air at 600°C for 2, 3, 4, 6, and 10 hours. An initial ramp-up over 1.5 hours of 6.5 degrees per minute was used for all samples. After calcination, the furnace automatically stopped heating and slowly cooled to room temperature. Powdered calcined samples were redispersed into water with a small amount of Tetramethylammonium Hydroxide (TMAH, 0.002%) added to stabilize the particles.

4.2.3. Particle Characterization

Scanning Electron Microscopy

Visualization of hematite particles was done with a scanning electron microscope (JEOL-6010).

Diffuse Reflectance Measurements and Band Gap

Light absorption properities of samples were investigated using a UV-Vis spectrometer (Perkin Elmer UV/VIS/NIR Lambda 1050) equipped with a mini-integrating sphere (150 mm InGaAs) for diffuse reflectance measurements. Band gap energies were calculated via the Kubelka-Munk method:

$$(f(R)h\nu)^{\gamma} = A(h\nu - E_g) \tag{4.1}$$

where $f(R) = \frac{(1-R)^2}{2R}$, R is the measured reflectance, $h\nu$ is the photon energy, E_g is the band gap, A is a proportionality constant, and γ is 2 for the direct allowed transition type of hematite corresponding to the hybridization between O 2p and Fe 3d states [133, 134]. The linear region of the Tauc plots, $(f(R)h\nu)^{\gamma}$ plotted against $h\nu$, are fit and E_g is extracted from the x-intercept of the linear fits [135].

Atomic Force Microscopy

Atomic Force Microscopy (AFM) measurements were conducted on a Bruker Dimension Icon. Surface Roughness, R_a, was calculated from AFM measurements by the volume of deviation from the average plane divided by the scanned area (500×500 nm^2). AFM image analysis was completed with open source python packages, specifically SPIEpy and pySPM [136, 137].

Single Particle X-ray Diffraction

Single particle x-ray diffraction (XRD) was preformed at the ID13 beamline of the European Synchrotron Radiation Facility (ESRF) in Grenoble, France. Samples of calcined hematite were prepared on silicon nitride windows via a droplet deposition. The incident x-ray beam with a photon energy of 13 keV (0.954 Å) and size of 250 nm was focused on a Dectris Eiger X 4M detector. The detector has 2048 x 2048 pixels with pixel size of 75 μm and was positioned 76 mm from the sample. 2D scattering patterns were collected with resolution up to $2\theta = 55$, i.e., $d = 1.0$ Å for several particles to account for various orientations of the particles on the substrate. Sample rotation was preformed from +45° to −45°. Data analysis and 2D integration of diffraction data was done in python with the PyFai package [138, 139]. We probe how the crystallite size changes for the various planes via the Scherrer's equation: $D_{hkl} = K\lambda/\beta\cos\theta$ [89]. The measured crystallite size is limited to the resolution of the experimental set-up which was determined via calibration with Al_2O_3 to be 200 nm. Therefore, crystallite sizes > 200 nm are reported to be ≥ 200 nm.

4.2.4. Active Motion Imaging

Aqueous swimming solutions contained 0.00075 wt% hematite particles and 5% H_2O_2 and were adjusted to pH 9 by drop-wise addition of TMAH. Samples were collected inside flat rectangular capillaries (Vitrocom 0.05 x 1.00 mm) and sealed with wax on a microscope slide. We followed the particle dynamics via an inverted microscope (Zeiss Axio Observer) equipped with a 20x objective (N-Achroplan 20x/0.45 M27), a CCD camera (Axiocam 705 color), and a mercury lamp (HXP 120 V). The intensity of the light source was controlled via a manual knob, and a longpass filter (AT450/50x) was used to restrict light emission to 425-475 nm. We acquired time lapses with frame rates between 2 and 55 fps for up to 2 minutes. The particles' positions were followed over time and their mean-squared displacements (MSD) were calculated in Python with the TrackPy package [140].

4.3. Results and discussion

4.3.1. Active Motion of Hematite

In order to investigate the swimming behavior of hematite microswimmers, we prepare a dispersion of hematite superballs in an aqueous solution of H_2O_2. Figure 4.1 A shows trajectories of the microswimmers from a common origin in the absence (pink lines) and presence (blue lines) of UV light. When the light is off, we observe that the microswimmers are restricted to a small region over the investigated time frame due to their Brownian motion. When the UV light is switched on, the micro-swimmers propel in random directions with relatively long, linear trajectories. Since the particles leave the origin in all directions, this lack of a preferred directionality in the trajectories indicates that the swimming motion is due to the activity of hematite rather than interactions with an external magnetic field or fluid flows. The observed swimming behavior of hematite is caused by a chemical gradient generated around the microparticle by the decomposition of H_2O_2 which allows self-phoretic propulsion to occur, as shown in the schematic of Figure 4.1 B [40]. While the entire surface of hematite can participate in these reactions, hematite microswimmers propel along substrates due to either symmetry breaking from surface imperfections or spontaneous instabilities that creates a difference in the chem-

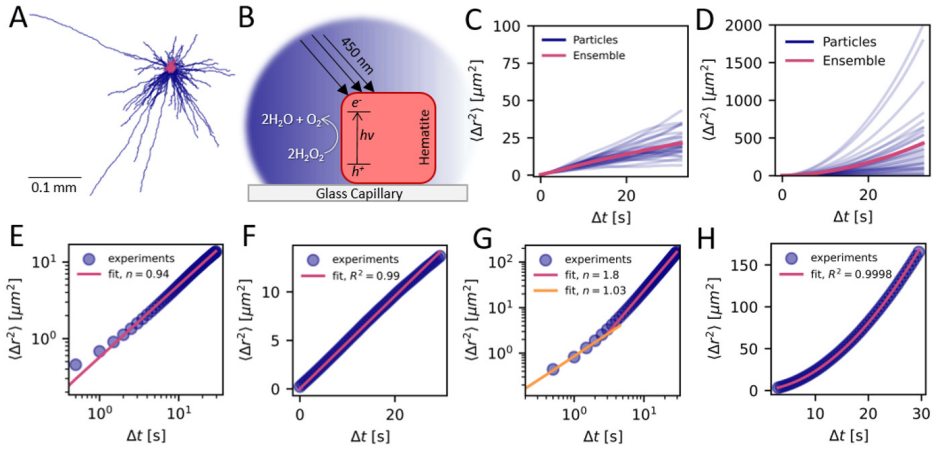


Figure 4.1: (A) All tracked particle paths are displayed from a common origin for as-prepared hematite microparticles in the absence and presence of UV light shown as pink and blue lines, respectively, over 30 seconds. (B) A schematic of the decomposition of fuel on the surface of hematite microparticles under 450 nm light which results in propulsion along the surface of the glass capillary. Mean-squared displacement (MSD) curves for particle trajectories (blue lines) in the absence (C) and presence (D) of UV light and the ensemble MSD curve (pink line). The ensemble MSD and appropriate fits for hematite micron-sized superballs: without calcination and without UV illumination in (E) log-log scaling fit to Equation 4.8 and (F) linear scaling fit to Equation 4.3. As well as, (G) without calcination and with UV illumination in log-log scaling fit piece-wise to Equation 4.8 and in (H) linear scaling fit to Equation 4.6.

ical gradient around the particle [119, 141]. The dynamics of our hematite superballs is further investigated by calculating the mean-squared displacement (MSD) curves of the particles. The MSD is obtained as:

$$\langle \Delta r^2 \rangle = \langle (\vec{r}(t + \Delta t) - \vec{r}(t))^2 \rangle \tag{4.2}$$

where $\vec{r}(t)$ is the position of the particle at time t. Ensemble MSD's are calculated by averaging over several hundred particles. As shown in Figure 4.1 C, the hematite particles display typical diffusive, linear MSD behavior which can be described by:

$$\langle \Delta r^2 \rangle = 4 D_0 \Delta t \tag{4.3}$$

where D_0 is the diffusion coefficent of the particle. We fit the linear ensemble MSD in Figure 4.1 F and found the diffusion coefficient to be $D_0 = 0.121\ \mu m^2/s$ with an $R^2 = 0.998$. We compare this value to the calculated value for a similarly size spherical particle from the Stokes-Einstein equation defined by [3]:

$$D_0 = \frac{k_B T}{6 \pi \eta r_p} \tag{4.4}$$

where k_B is the Boltzmann constant, η is the viscosity of the continuous medium, T is the temperature, and r_p is the radius of the spherical particle. For the case of a spherical

particle with a radius on the length scale of our particles, $r_p = 0.75\ \mu$m, and in the same conditions, the diffusion coefficient is calculated to be $0.293\ \mu m^2/s$. Indeed, simulations and experiments on the Brownian hydrodynamics of superball particles have shown that the diffusion coefficient is only minimally affected by the particle shape [142, 143]. When the UV light is turned on, the particles exhibit characteristic active motion from their MSD profiles as shown in Figure 4.1 D. The MSD for this type of motion in 2D at any time is described by the Ornstein-Uhlenbeck equation [144]:

$$\langle \Delta r^2 \rangle = 4D_0 \Delta t + \frac{v^2 \tau_r^2}{3}\left(\frac{2\Delta t}{\tau_r} + e^{-2\Delta t/\tau_r} - 1\right) \tag{4.5}$$

where v is the propulsion velocity and τ_r is the rotational diffusion time. Equation 4.5 is often reduced into three regimes depending on whether $\Delta t \ll \tau_r$, $\Delta t \approx \tau_r$, or $\Delta t \gg \tau_r$. In the first regime, at short time scales ($\Delta t \ll \tau_r$), the equation is reduced to Equation 4.3 where the motion is diffusive. In the second regime, when $\Delta t \approx \tau_r$, self-propulsion has a larger effect and Equation 4.5 is reduced to:

$$\langle \Delta r^2 \rangle = 4D_0 \Delta t + 2v^2 \Delta t^2. \tag{4.6}$$

In the final regime, where $\Delta t \gg \tau_r$, the rotational diffusion randomizes the direction of propulsion leading to [145]:

$$\langle \Delta r^2 \rangle = 4D_0 \Delta t + 2v^2 \tau_r \Delta t \tag{4.7}$$

Therefore, we can determine the regimes we have access to by fitting the MSD curves to a generalized equation of:

$$\langle \Delta r^2 \rangle = A \Delta t^n \tag{4.8}$$

where A is a constant and n dictates the power where $n = 1$ is indicative of the two diffusive regions and $n = 2$ the self-propulsion region. Interestingly in Figure 4.1 G, we only observe the first diffusive region and the propulsion region where $n = 2$ indicating that $\Delta t_{\text{Exp}} \approx \tau_r$. For a spherical particle, the rotational time from the Stokes relationship, where $\tau_r = 8\pi\eta R^3/k_B T$, can be calculated as $\tau_{\text{r,sphere}} \approx 6$ s. In these experiments, we measure time lags of up to $\Delta t = 30$ s. This indicates that $\tau_r \geq 30$ s for the hematite superballs. The large τ_r paired with the observed linear trajectories during active motion indicates that our particles' shape plays an important role during self-propulsion. This active-based behavior is supported by recent simulations of cubic micro-swimmers in micro-channels that show active cubes have linear trajectories inside micro-channels rather than the typical oscillatory behavior seen in spheres in ellipsoids [146].

4.3.2. Active Motion of Calcined Hematite

In order to improve the active motion of hematite micro-particles, we calcine hematite superball particles at 600°C for varying times from 2 to 10 hours as described in section 4.2. Figure 4.2 A shows the particle trajectories over the different calcination times as well as non-calcined particles indicated as 0 hours. Hematite calcined for 2 hours at 600°C already changes the average trajectory length to 151 μm from the 45 μm for non-calcined hematite. After 3 to 10 hours of calcination, the average length of the particles' trajectories

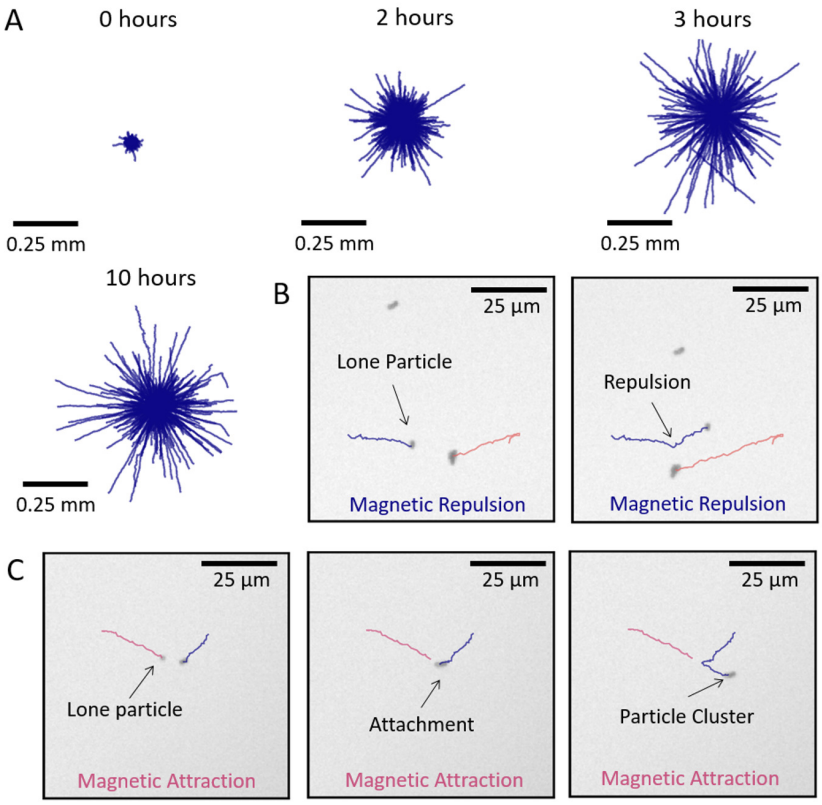


Figure 4.2: Active motion behavior of hematite microparticles in the presence of H_2O_2 fuel and UV irradiation. (A) All tracked particle paths from a common origin for samples of Non-calcined particles (0 hours) and particles calcined at 600°C for 2 hours, 3 hours, and 10 hours over 1 minute. (B) Still frames from a movie of 3 hr calcined particles showing magnetic (B) attraction and (C) repulsion of a lone particle (pink trajectory) and particle cluster (blue trajectory). (D) All tracked particles mean-squared displacement (MSD) curves (blue lines) and the ensemble MSD curve (dashed line) for samples of Non-calcined particles (0 hours) and particles calcined for 2 hours, 3 hours, and 10 hours. Inset displayed for non-calcined particles shows the MSD curves at a more suitable scaling.

increases again to 260 μm apparent from the long trajectories extending farther than particles calcined for 2 hours in Figure 4.2 A. While most of the particle trajectories follow a relatively straight path, some trajectories appear to suddenly turn and change direction. Further investigation of the optical microscopy movies, we observe two hematite particles approaching each other and deflecting in Figure 4.2 B, as well as two hematite particles approaching each other and attracting forming a cluster in Figure 4.2 C. The origin of these interactions is due to the particle's inherent magnetic moment and subsequent dipole-dipole interactions where in one case they are repulsive and in the other attractive [24]. Therefore, when two particles approach each other, they will experience attraction or repulsion based on their (dipole) orientation to each other which results in particle

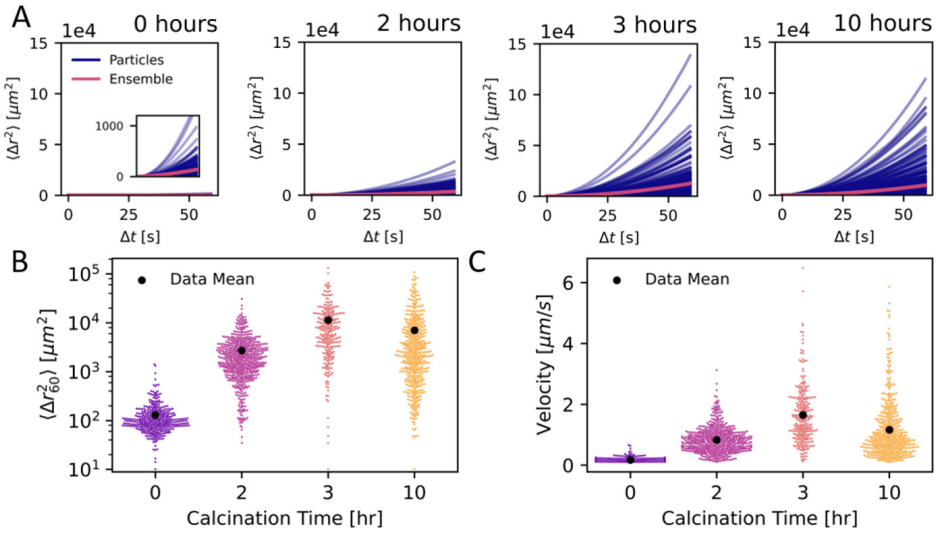


Figure 4.3: Comparison of sample calcination times corresponding to MSD curves displayed in Figure 4.2. (A) MSD, $\langle \Delta r^2 \rangle$, at $\Delta t = 60$ s displayed on a logarithmic y-scale. Larger lack dots correspond to the mean of the data set. (B) Extracted velocity in μm/s from MSD fitting to $\langle \Delta r \rangle = 4D_0 \Delta t + 2v^2 \Delta t^2$. Larger black dots correspond to the mean of the data set. SEM images of (C) non-calcined and (D) calcined for 6 hours hematite microparticles with a superball shape. Scale bars correspond to 5 μm.

tracks with sharp deflections. Figure 4.2 D shows the MSD curves as a function of the time lag for the samples with different calcination times for all individual particles observed (blue lines) and the ensemble MSD (pink lines). For all plots, the y-axis is scaled to 150000 μm^2. For the MSD curves of non-calcined particles, denoted as 0 hours, the inset shows the particles still have characteristic active Brownian curves which can reach up to 1400 μm^2 at $\Delta t = 60$ s. After two hours of calcination at 600°C, the MSD increases slightly while after 3 and 10 hours of calcination the MSD of several particles increases greatly within the observed Δt. In order to better compare samples with various calcination times, we extracted the MSD value at $\Delta t = 60$ s in Figure 4.3 A. Due to the presence of high and low tails in the distribution, we plot the data points for all values on a logarithmic scale which depicts the log-normal distribution of the MSD for all active hematite samples. It is clear that calcination improves the average for samples by at least 20-fold as seen for 2 hours of calcination at $\Delta t = 60$ s. At 3 hours of calcination time, we observe the highest obtained average mean squared-displacement of 11,344 μm^2 or an average 87-fold increase at $\Delta t = 60$ s. Finally, we can extract the velocity from the MSD curves of all particles by fitting the curves to Equation 4.6 with a fixed D_0 found for the Brownian motion in the absence of UV light ($D_0 = 0.121$ $\mu m^2/s$). The fitted velocity is shown in Figure 4.3 B. The average velocity fit for non-calcined hematite particles is 0.17 ± 0.06 μm/s which is on average increased by 5-, 10-, and 7-fold (0.8 ± 0.4, 1.6 ± 0.9, and 1.16 ± 0.9 μm/s) for particles calcined for 2, 3 and 10 hours, respectively.

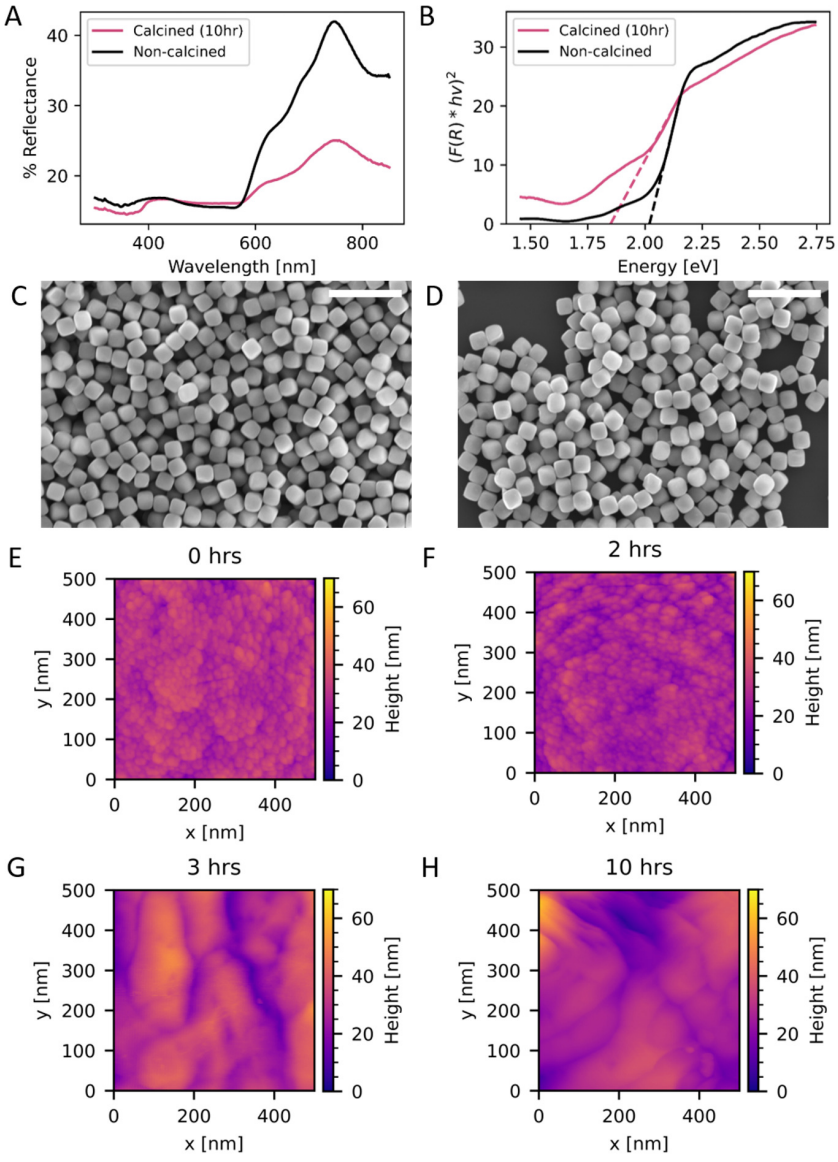


Figure 4.4: (A) Diffuse reflective spectroscopy (DRS) measurements for non-calcined superballs (blue line) and calcined for 10 hours (pink line). (B) Kubelka-Munk (K-M) plots for band gap calculations from the DRS measurements. Dashed lines represent the fit to the linear region of the K-M plots with intersections at 1.85 and 2.05 eV, for calcined and non-calcined superballs respectively. SEM images of (C) before calcination and (D) after 10 hours of calcination. AFM images of the surface of hematite superballs (E) before calcination and calcined for (F) 2 hours, (G) 3 hours, (H) 10 hours at 600°C.

4.3.3. Optical and Surface Properties

To quantitatively explain the improvement of photocatalytic activity, we measured the UV-Vis diffuse reflectance spectroscopy (DRS) of calcined and non-calcined hematite superballs (Figure 4.4 A). The non-calcined superballs show a strong absorption edge around 570 nm displaying their visible light absorption ability which persists when the superballs are calcined for 10 hours at 600°C. We estimate the band gap of the two samples based on the Kubelka-Munk formula as shown in Figure 4.4 B. According to the linear regions of the two samples, the band gap energy, E_g, of the non-calcined and 10 hour calcined superballs was calculated to be 2.05 and 1.85 eV, respectively. Other experiments have shown a similar trend of decreasing band gap for increasing calcination temperature [131, 147, 148]. Since we illuminate the hematite microparticles with 450 nm light, it is possible that reducing that bandgap to 1.85 eV allows hematite to more effectively utilize the illuminated light in our experiments.

In order to investigate the superball morphology during different calcination steps, we takes scanning electron microscopy (SEM) images and atomic force measurements (AFM) on the surface of the hematite particles. Ulfa *et al.* [149] show that calcination transforms hexagonal hematite platelets into cubic-like particles. This transformation also led to an overall reduction in the photocatalytic proprieties of their hematite particles. In our case, we don't observe any changes in the particle size and shape after calcination as shown in the SEM images of Figure 4.4 C and D for before and after calcination, respectively. We probe the faces of single particles directly with AFM in 500 × 500 nm areas to further explore the surface morphology as shown in Figure 4.4 E-H. Figure 4.4 E shows the surface of a non-calcined particle. We observe the presence of small (15± 3 nm) nodules that protrude on average 21±4 nm high. After calcination for 2 hours, we observe similar nodules throughout the particle faces as seen in Figure 4.4 F. After 3 hours of calcination in Figure 4.4 G, there is a dramatic change on the surface of the particle where nodules are no longer present and instead broad regions span across the surface. A similar pattern is also seen on particles calcined for 10 hours (Figure 4.4 H) where the height difference from the lower valleys to the surface peaks doubles, from 32 nm to 68 nm.

The crystallinity of prepared hematite samples was quantified via single particle x-ray diffraction (XRD) measurements, as explained in section 4.2. Single particle XRD patterns for different calcined hematite samples are shown in Figure 4.5 A. The resolved diffraction peaks match the typical α-Fe_2O_3 R3/c lattice (vertical lines) where $a = b = 5.035$ Å and $c = 13.74$ Å. For hematite superballs, the {012} plane family is expected to encapsulate the superball faces [151]. Therefore, we can probe the crystallite size of the (012) reflections at increasing calcination times as described in section 4.2. For non-calcined superballs (0 hours), we observe an average crystallite size of 25 ± 1 nm which is in good agreement with the previously reported crystallite size of the (012) plane of hematite superballs at 25.5 nm [151]. For all calcined samples, we observe a drastic increase of crystallite size for all measured particles to ≥ 200 nm as summarized in Figure 4.5 C. Though, we note that it is difficult to verify if the {012} family has the dominant influence on the photocatalytic proprieties of hematite superballs. Interestingly, experiments on the photocatalytic degradation of organic molecules with hematite nanoparticles have suggested that smaller crystallite and particle sizes are desired for enhanced photocataltyic activity [131, 152, 153]. However, all of these experiments already utilized a calcination step during

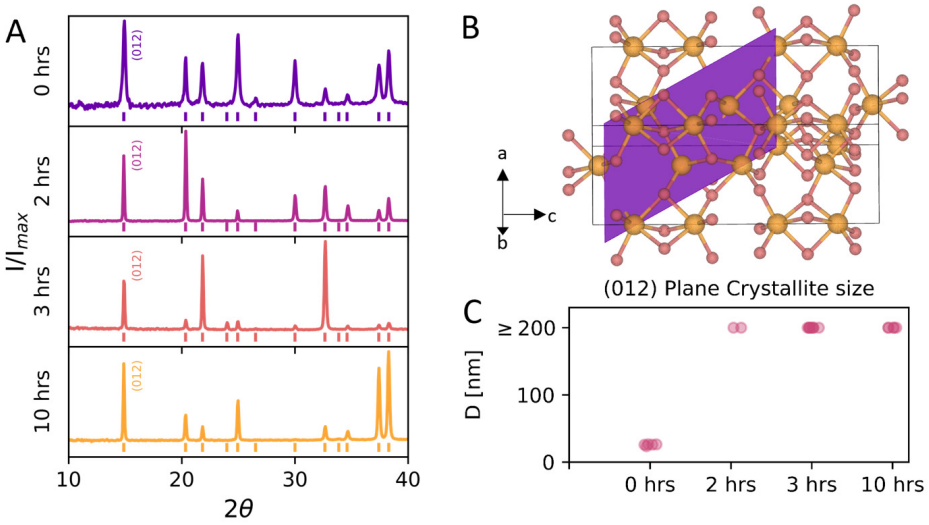


Figure 4.5: (A) 1D XRD patterns for a single superball particle at different calcination times: 0 hours, 2 hours, 3 hours, 10 hours. Straight vertical lines above each x-axis represent peak positions for bulk hematite. (B) Model of hematite's crystal structure with the (012) plane highlighted and orientated with the b* plane perpendicular. This model was generated with VESTA [150]. (C) Plot of calculated Scherrer's crystallite size from the full width at the half maximum (fwhm) of the (012) peak of superball particles at different calcination times. Multiple particles were analyzed to confirm crystallite sizes.

particle synthesis of at least 150°C and vary both the nanoparticle size and crystallite size from 8-100 nm. For WO_3 microparticles, Nandiyanto *et al.* [154] show that increasing the crystallite size from 19-42 nm while maintaining the same particle size drastically increases the photocataltyic performance of tungsten oxide microparticles in a photo-degradation test of curcumin which may reflect a more accurate depiction of our (micro-) hematite superball system.

4.4. Conclusions

In this chapter, we investigated the influence of calcination time at 600°C on the photocatalytically driven active motion of micron-sized hematite superballs. We show that calcination of at least 2 hours already improves the active motion observed by a 20-fold increase in the average MSD from non-calcined superballs. This can further improve to an 87-fold increase with 3 hours of calcination at 600°C. This large increase is obtained along with changes to the optical band gap as well as the crystallinity of the hematite particles, but only minimal changes occur to the overall particle morphology. Therefore, we provide a simple, scalable, and cost effective method to enhance the photocataltyic performance of hematite microparticles as an active swimmer which may easily be exploited by other key areas of photocatalysis research.

Acknowledgements

This chapter could not have been completed without the help of several people. I would like to specifically thank: Prof. Stefano Sacanna for invaluable discussions and guidance throughout the project, Silvana Andrea Caipa Cure for assistance with preparation and characterization of hematite active swimmers, Stefanie Neuber for assisting during analysis of XRD experiments, Prof. Atsushi Urakawa for advice on band-gap measurements and analysis, and Marcel Bus for assistance with the AFM measurements of hematite particles. I would also like to thank TUDelft's OM Group for access to DRS measurement equipment and their furnace for particle calcination. Finally, I would like to thank Asma Medjahed and Manfred Burghammer from the ID13 beamline at the ESRF as well as Andrei Petoukhov for assistance with and during single particle diffraction experiments.

Part III

Preparation of Magnetic Microparticles

Chapter 5

Preparation of Magnetic Polystyrene Microparticles via Emulsion Droplet Evaporation

ABSTRACT:

While polymeric particles are widely used in various applications and have established synthetic processes, incorporating other components into the polymeric matrix can endow desirable features. However, the limitations of traditional polymerization methods have become apparent in their inability to produce uniform composite particles, often resulting in issues such as phase separation within the particles. Therefore, alternative methods that can overcome these limitations and produce more uniform composite particles are needed to meet the demands of modern applications. This chapter investigates a straightforward yet adaptable synthetic technique for producing micron-sized polystyrene particles loaded with magnetic cobalt ferrite nanoparticles. A solvent-in-water emulsion is formed by emulsifying dissolved polystyrene plus lipophilic cobalt ferrite dispersed in a suitable solvent phase. When the solvent from the emulsion droplets evaporates, composite polystyrene and cobalt ferrite microparticles are formed. Further adjusting the polystyrene, cobalt ferrite, and stabilizing surfactant concentrations in the system results in spherical particles with internal or surface pores. The generated particles can be subsequently plasticized reducing the overall particle size by removing porosity. Overall, this approach produces tunable particles with easily adjustable magnetic concentration and particle size.

5.1. Introduction

Magnetic polymeric particles have been employed widely in a variety of fields. Magnetic polystyrene, for example, is used in cell separation and particle-based enzyme immunoassays [155–157]. Magnetic polystyrene has also been used in environmental remediation for oil and water separation and heavy metal and dye removal [158–160]. Several methods have been developed for the preparation of magnetic polymer particles. One common method is polymerization of a monomer in the presence of magnetic nanoparticles [157]; for example, via dispersion or (mini-)emulsion-based polymerization. These types of polymerization results in a two phase system with the polystyrene and the magnetic nanoparticles as the separate phases. The resulting composite particles internal structure depends on the polymerization technique where Janus-like and core-shell structures form for dispersion and mini-emulsion polymerization, respectively [158, 161–165]. However, limited loads and nanoparticle aggregation appear to be significant barriers during polymerization due to the difficulty controlling the nanoparticle dispersion stability in the monomer phase.

Viable alternatives to polymerization techniques are physical-based methods. Ugelstad *et al.* [166, 167] developed a swelling technique in which polymeric microparticles are swollen by an organic solvent to allow nucleation of inorganic nanoparticles uniformly throughout the polymeric matrix. However, the nucleation of inorganic nanoparticles inside a swollen polymeric matrix is restricted to nucleation mechanisms that preserve the polymeric matrix while producing nanoparticles smaller than the pore size of the swollen polymer, which is in general on the order of 10 nm [167]. Another swelling technique has also been used to encapsulate magnetic micron-size hematite via melting of polymeric beads to form a core-shell particle when the surfaces of two constituent particles posses opposite surface charges [58]. In a similar manner, magnetic nanoparticles attracted to an oppositely charged surface of a polymer are embedded into the surface by adding a plasticizer to the solution, physically trapping the nanoparticles under the polymeric surface [168, 169]. One promising new technique to prepare polymeric microparticles is through emulsion droplet evaporation. This method, which evaporates solvent from emulsion droplets containing dissolved polymers, has been used to form a variety of polymeric microparticles [170]. When coupled with block co-polymers, anisotropic microparticles can be formed when the evaporation conditions and surfactant selection is tuned [171] which is of interest for the design of self-assembled materials. Control over the emulsification method and evaporation time of the droplets resulted in dimpled and crumpled microparticle morphologies which provide higher surface areas than their spherical counterpart [172]. This is interesting for specific applications such as drug and cargo delivery. Specific drugs, can be loaded into the solvent phase of the emulsion, yielding polymeric microparticles with high drug loads [173]. When nanoparticles are used to stabilize the emulsion droplets, the nanoparticles are only present at the surface of the final polymeric microparticle [174–176]. To obtain nanomaterials internally, they or their precursors are bound to the (block co-)polymer before emulsification which provides the particles with specific internal locations and, in the case of a precursor, to be grown [177–179]. These methods for incorporating nanomaterials into polymeric microparticles are complex and usually require specific nanomaterial functionalization.

In this chapter, we present an emulsion droplet evaporation technique for prepa-

ration of polystyrene microparticles loaded with magnetic, cobalt ferrite nanoparticles. This technique allows control over various parameters such as the concentration of stabilizing surfactant in the aqueous phase, polystyrene and cobalt ferrite concentration in the solvent phase, and the solvent-to-water ratio. We investigate the effects these parameters have on the morphology of the resultant particles. We further explore the resulting particle sizes and morphologies using electron microscopy characterization techniques. The facile inclusion of magnetic nanoparticles within polymeric microparticles that we propose, may provide a simple and scalable alternative for products available commercially.

5.2. Materials and Experimental Methods

5.2.1. Materials

Styrene (with 4-tert-butylcatechol as stabilizer, ≥99%) was obtained from Sigma Aldrich and passed through basic alumina prior to use to remove inhibitor. Dibenzoyl peroxide (BPO, >75%), cobalt (II) chloride hexahydrate ($CoCl_2 \times 6H_2O$, ≥ 95%), iron (III) chloride hexahydrate ($FeCl_3 \times 6H_2O$, ≥ 98%), iron (III) nitrate nonahydrate ($Fe(NO_3)_3 \times 9H_2O$, ≥ 98%), sodium hydroxide (NaOH, ≥ 98%), hydrochloric acid (HCl, 37%), nitric acid (HNO_3, 60%), oleic acid (90%), sodium lauryl sulfate solution (SDS, 10%), and tetrahydrofuran (THF, 99.5%) were all used as received and purchased from Sigma Aldrich or TCI Europe.

5.2.2. Methods

Polymerization of Styrene

Polystyrene was synthesized by free radical polymerization of styrene monomer as follows. Styrene (27 g), Toluene (45 mL), and BPO (0.28 g) were combined in a 100 mL round bottom flask and connected to a condenser. The reaction mixture was deoxygenated by bubbling with argon for 30 minutes and the temperature was increased to 80°C for 37 hours to obtain polystyrene at an 84% conversion determined by ^{1}H NMR on an Agilent 400-MR DD2 spectrometer. The formed polystyrene was then diluted with 30 mL chloroform and precipitated dropwise into a stirring 500 mL solution of ice-cold methanol. The precipitate was then dried under vacuum to obtain a 99% pure polystyrene with trace styrene monomer and toluene (Figure 5.1 A).

Magnetic Nanoparticle Synthesis

Magnetic cobalt ferrite nanoparticles were prepared via a co-precipitation method [180, 181]. $CoCl_2 \times 6H_2O$ (2.40 g) was dissolved into a 5 mL aqueous solution of 7.5% HCl, and 5.50 g of $FeCl_3 \times 6H_2O$ was dissolved in 40 mL of water. The two solutions were briefly stirred together and then rapidly added to 200 mL of boiling NaOH (1M) solution where a black precipitate was quickly formed. The mixture was vigorously stirred with a magnetic stirrer at 100°C for 1 hour under reflux. The dispersion was cooled to room temperature and washed via magnetic sedimentation once. The particles were redispersed in 50 mL of water, and 30 mL of 2M HNO_3 was added. Under stirring, 30 mL of a 0.35 M $Fe(NO_3)_3 \times 9H_2O$ solution was added to the particle suspension and heated at 100°C for 1 hour. The dispersion was cooled again to room temperature, washed thrice via magnetic separation, and redispersed into 50 mL of water. The surface of the prepared cobalt ferrite

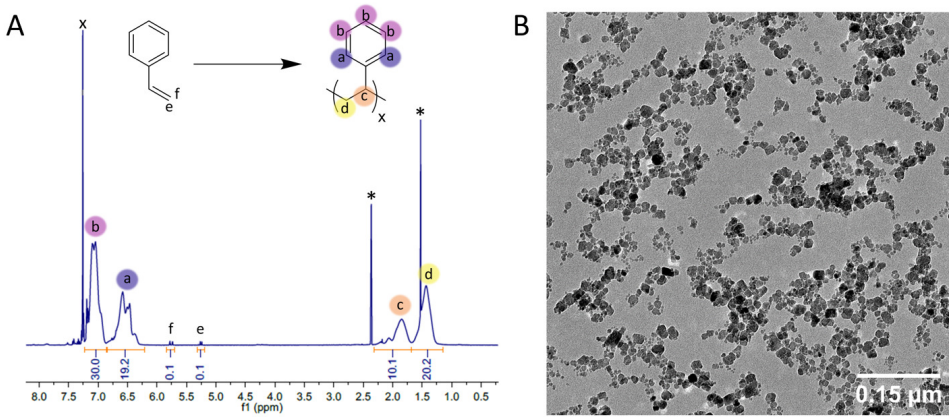


Figure 5.1: (A) ^{1}H NMR ($CDCl_3$) of polystyrene demonstrating successful purification (> 99%) of polystyrene. Starred peaks (*) indicate water and toluene impurities. (B) TEM image of as-prepared cobalt ferrite nanoparticles.

nanoparticles was modified with oleic acid: oleic acid (15 mL) was added dropwise to the prepared aqueous dispersion of cobalt ferrite and stirred for 18 hours. The resulting modified particles were separated from the remaining aqueous phase and washed several times with ethanol via magnetic separation.

Formation of Porous Polystyrene Magnetic Microparticles

Loaded magnetic polystyrene microparticles were prepared by an emulsification technique. We added 1 mL of a 0.1% SDS to a 2 mL Eppendorf tube. We added a 50 μL DCM solution containing (1.5 – 10 wt%) dissolved polystyrene and cobalt ferrite (0.03 – 1 wt%) dispersed cobalt ferrite. The dispersion was shaken by vortex for 20 s and placed in an ultrasonic bath for 1 minute. When the dispersion turned milky white, we diluted it with 3 mL of either pure water or 0.1% SDS in water. We then placed it under vacuum on a rotary evaporator at 40° C heating for 25 minutes to remove remaining DCM. The particles were washed via gravitational sedimentation thrice and redispersed into water.

Plasticization of Magnetic Polystyrene Particles

To remove hollow and porous polystyrene particles, the particles were plasticized as follows. A 3 mL aqueous solution of 40% THF was added to 1 mL of a particle dispersion and gently agitated by hand for 20 seconds. Immediately after, the solution was diluted with 20 mL of water and the particles were sedimented under gravity and washed with water.

Material Characterization

Transmission electron microscopy (TEM) measurements were preformed on a JEOL JEM-1400 plus TEM operated at 120 kV. Samples were prepared by placing 5 μL of a diluted particle dispersion onto carbon coated copper grids and allowed to dry.

Scanning electron microscopy (SEM) measurements were preformed on a JEOL JSM-6010LA with secondary electron and back-scattered electron detectors as well as energy dispersive x-ray spectroscopy (EDX) capabilities. Samples were prepared by placing 5 μL

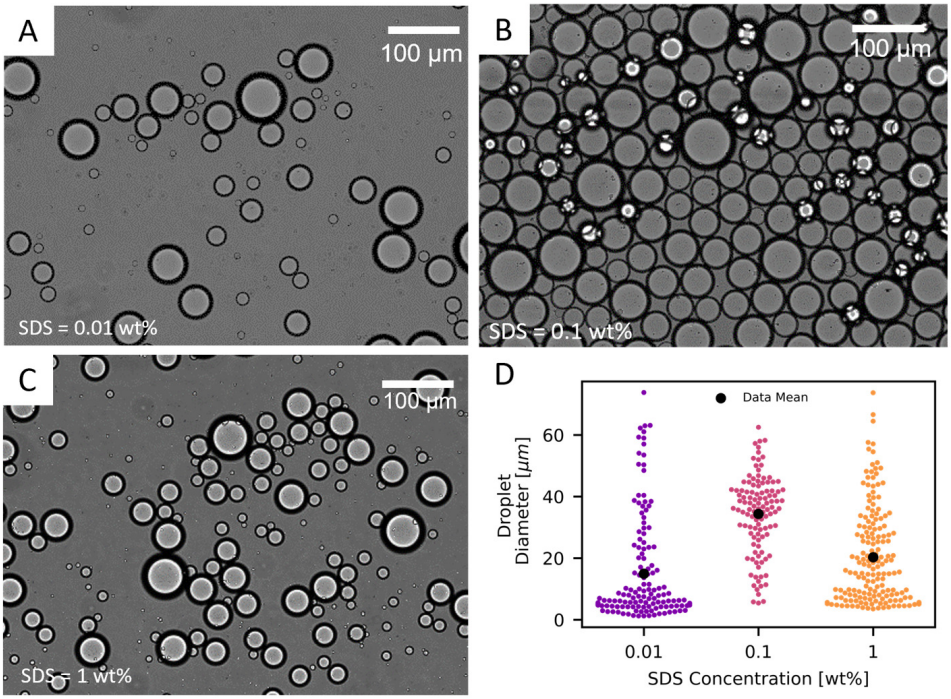


Figure 5.2: Optical microscopy images of DCM emulsion droplets containing 5 wt% polystyrene before evaporation with (A) 0.01 wt% SDS, (B) 0.1 wt% SDS, and (C) 1 wt% SDS in the aqueous phase. (D) Measured emulsion droplet diameters.

of a diluted particle dispersion onto a cut silica wafer and allowed to dry. Electron images and elemental distribution maps were collected of various samples.

Particle (and droplet) sizes and distributions were analyzed via the ImageJ software [182] from the microscopy images. Dispersity, Đ, of particle diameters was calculated as:

$$Đ = \frac{\sigma}{d} \times 100 \tag{5.1}$$

where σ is the standard deviation and d is the particle diameter.

5.3. Results and Discussion

5.3.1. Effect of Surfactant Concentration

To prepare stable emulsions that produce uniform particles, we first varied the surfactant concentration in the aqueous phase between 0.01 – 1 wt%. As described in section 5.2, we use sodium dodecyl sulfate (SDS) to stabilize the formed emulsion droplets, which contain 5 wt% polystyrene, as well as the resultant composite particles. Figure 5.2 A-C displays optical microscopy images of emulsion droplets before solvent evaporation. In Figure 5.2 A, there is 0.01 wt% SDS in the aqueous phase which is much lower than the critical micelle concentration (CMC_{SDS} = 0.22 wt%), and we observe the presence of large

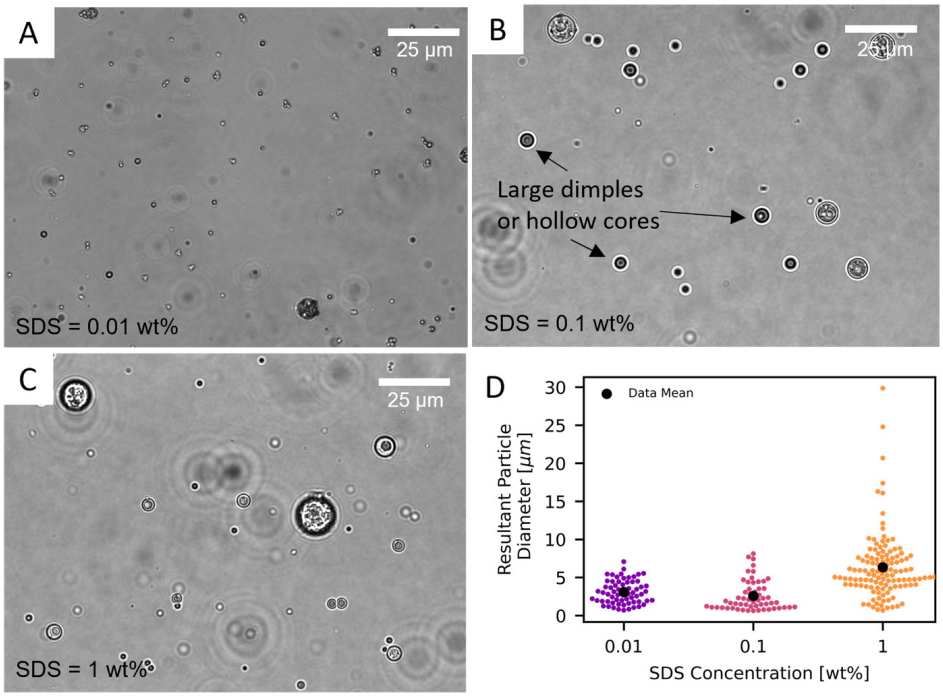


Figure 5.3: Optical microscopy images of resultant particles formed from DCM droplets with (A) 0.01 wt% SDS, (B) 0.1 wt% SDS, and (C) 1 wt% SDS in the aqueous phase and (D) resultant particle diameters.

and small droplets. Increasing the SDS concentration to 0.1 wt%, we see a larger concentration of droplets with diameters around $20-40$ μm as shown in Figure 5.2 B. Above the CMC_{SDS} at 1 wt%, Figure 5.2 C contains several emulsion droplets with diameters $2-10$ μm with some larger (>40 μm) droplets still present. We summarize the distributions of droplet diameters in Figure 5.2 D. At 0.01 wt%, the distribution of droplet sizes is skewed towards lower diameters while still forming droplets above 50 μm. For 0.1 wt%, the droplet diameter is well distributed around the mean droplet size, $\langle d_{0.1\%} \rangle = 32$ μm.

We investigate the effect of SDS concentration on the resultant particle after solvent evaporation in Figure 5.3. Characteristic optical microscope images of particles after DCM removal are shown in Figure 5.3 A-C. For particles prepared in 0.01 wt% SDS, we observe relatively small particles (<5 μm) that form aggregates of a couple particles as seen in Figure 5.3 A. However, not pictured are areas of higher particle concentration in which the sample is highly aggregated (Appendix A). At 0.1 wt% SDS concentration, the aggregation is no longer apparent and larger particles with large dimples or hollow cores are seen in Figure 5.3 B. Above the CMC, at 1 wt% (Figure 5.3 C), large particles above >20 μm can be prepared. However, we observe that the internal structure is not completely polymeric with the possible presence of bubbles or voids for the larger particles. We compare the particle sizes for the different surfactant concentrations in Figure 5.3 D. Below the CMC, at 0.01 wt%, there is a relatively narrow size range, $0.2-8.5$ μm, for particle sizes where on

average the diameter is 4.3 μm. This is similar for 0.1 wt% SDS concentration where the average diameter is decreased to 3.1 μm. Above the CMC, the average resultant particle diameter increases to 9.5 μm for 1 wt%. We note the lack of small (< 0.5 μm) particles is due to the particle washing method which utilizes gravitational settling. Therefore, for further experiments, we select the SDS concentration which provides a narrow size distribution for the resultant particles without aggregation which is 0.1 wt%. Wang *et al.* [183] found that altering the type of surfactant used and its concentration could create unique final particle shapes for poly(methylmethacrylate) (PMMA), such as acorns and ellipsoids, but SDS generally produced particles with spherical/dimpled shapes. Indeed, here we consistently obtained spherical particles at different surfactant concentration.

5.3.2. Effect of Solvent-to-Water Ratio and Polymer Concentration

To investigate the effect of the solvent-to-water ratio on the morphology of the microparticles, the volume of the added solvent (DCM) phase was varied from 1.25 – 20.0 vol %. We also varied the concentration of polystyrene in DCM from 1 – 10 wt%. SEM images of the prepared samples are shown in Figure 5.4. For the lowest amount of solvent added (1.25 vol%), a particle dispersion did not form for any polystyrene concentration. Instead, a thin film of polymer would normally form (pictured in Appendix A) which is likely caused by evaporation of the majority of solvent before a proper emulsion is formed. On the other side, we could not obtain microparticles with highest solvent amount (20.0 vol%) either. For all polymer concentrations, large films and aggregates would form during emulsification or not all of the solvent phase would form an emulsion (pictured in Appendix A). In Figure 5.4, we see the presence particles with diameters between 0.3 – 15 μm throughout the various samples. Bucket-like and dimpled particles were observed in a majority of samples, and particles with diameters larger than 5 μm often showed dimpled surfaces. There are two proposed methods for the formation of the microparticles via solvent evaporation from a droplet. In both methods, high concentrations of polymer act as a shell near the droplet interface. As the droplet evaporates, either the shell (i) recedes with the evaporating solvent and solidifies or (ii) remains at the initial droplet interface with solvent evaporating through the formed shell [184, 185]. In two-polymer systems with polystyrene and PMMA, denting or dimpling of the micro-particles occurred as the separated polystyrene phase began contracting inside the solvent droplet [186, 187]. Therefore, the presence of dimpled and bucket-like particles indicates that our system likely contains hollow or porous particles.

Examining the particles to a greater extent reveals that low solvent concentrations, at 2.5 vol%, promotes the formation of particles with high size dispersities where Đ> 150% for all polystyrene concentrations. Additionally, at 1 wt% polystyrene, we observe broken particle pieces throughout the samples which suggests the formation of thin polystyrene shells that cannot withstand solvent evaporation. For 5.0 vol% solvent concentration and polystyrene concentrations above 1 wt%, 90% of the formed particles are spherical, and 20 – 40% of the particle diameters are between 1 – 5 μm. For ≥ 10 vol% of solvent, polystyrene films and aggregated clumps are more likely to form during the emulsion droplet evaporation process (not pictured). Therefore, we use a solvent concentration of 5 vol% with polystyrene concentrations higher than 1 wt% for the remainder of this chapter.

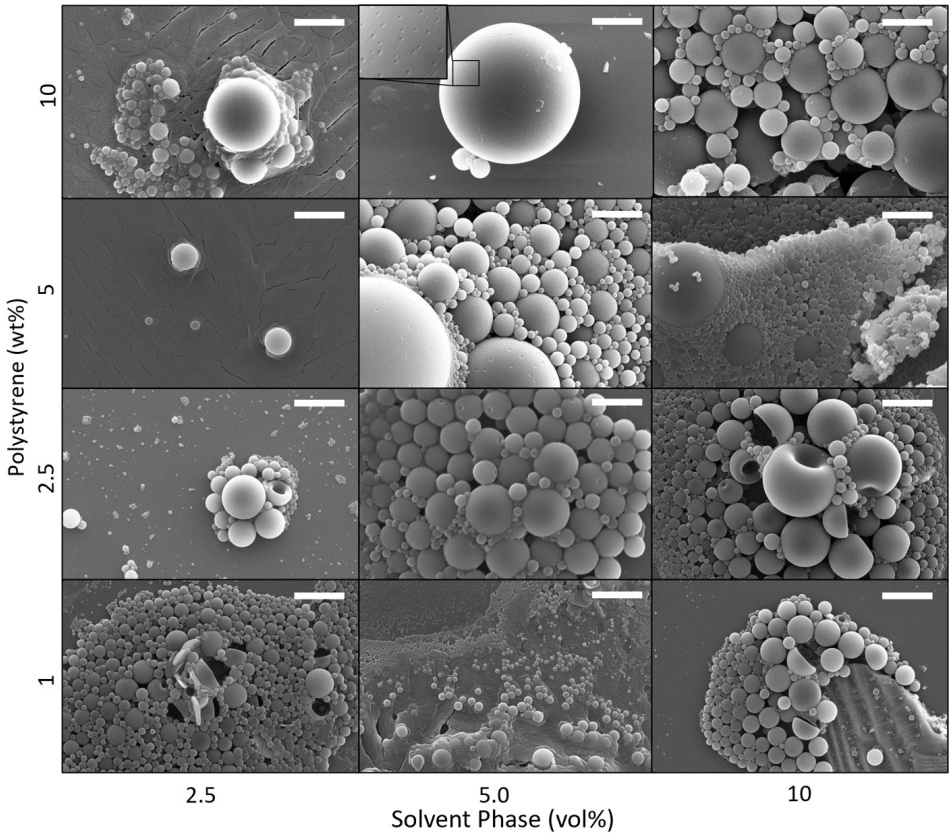


Figure 5.4: Representative SEM images of samples for 2.5, 5.0, and 10 vol% solvent in water concentrations with polystyrene concentrations of 10, 5, 2.5, and 1 wt% in the solvent phase. All scale bars correspond to 5 μm. Along the top of the SEM images distribution curves of particle diameters appear for varying polystyrene weight percents.

5.3.3. Effect of Polystyrene to Cobalt Ferrite Ratio

For particles loaded with cobalt ferrite, we noticed a change in particle morphology when the SDS concentration was kept at 0.1 wt% during evaporation under vacuum as shown in Figure 5.5. This behavior was not noticeable at polymer-to-nanoparticle ratios less than 25 : 1 or with only polystyrene present, as discussed in subsection 5.3.1. For polymer-to-nanoparticle ratios at and lower than 10 : 1, we see crumpled or highly porous particles throughout the sample. Witschi *et al.* [188] show that increased drug loading inside polymeric particles produced via a similar solvent evaporation method results in highly porous or dimpled particles. This effect was beneficial for drug delivery systems due to increased surface area from the pores. Therefore, it is worth noting the method explored throughout this chapter can be adapted to form a variety of particles with unique morphologies.

Rather than maintaining the concentration of SDS at 0.1 wt% before solvent evapora-

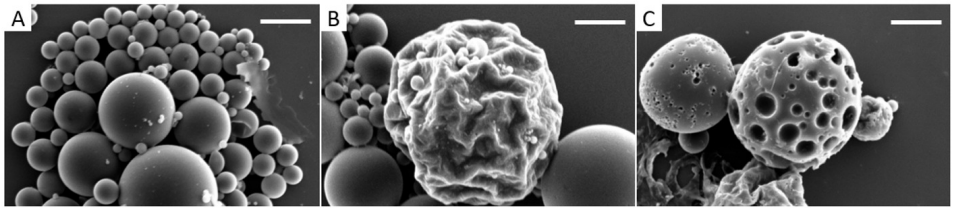


Figure 5.5: SEM images of loaded polystyrene particles evaporated in the presence of 0.1 wt% SDS with polystyrene to cobalt ferrite ratios of (A) 25 : 1, (B) 10 : 1, and (C) 5 : 1. All scale bars correspond to 10 μm.

tion as described in section 5.2, diluting the sample with pure water resulted in particles without this type of porous or crumpled surface. Figure 5.6 displays representative SEM images of particles prepared with varying polystyrene and cobalt ferrite ratios. In general, we observe a large distribution of particle sizes. Samples prepared with 1.5 wt% polystyrene resulted in particles with $d > 10$ μm which were all (partially) collapsed. At higher polystyrene concentrations, these large, collapsed particles only made up 4% of the samples until 7.5 wt% polystyrene in which there were only 5-10 particles visible per sample. As we decrease the polymer-to-nanoparticle ratio to 10 : 1, we do not observe significant differences in the resultant particle shape for polystyrene concentrations above 1.5 wt% where the majority of particles are spherical. At 1.5 wt%, we see that decreasing the polymer-to-nanoparticle ratio results in a decrease of large, collapsed particles from > 90% with no loading to < 50% for the 10 : 1 ratio. Figure 5.7 shows the correlations between our varied parameters and the resulting mean particle diameter and sample dispersity. We can see a slight trend of larger particle diameters for lower polymer-to-nanoparticle ratios especially for 2.5 wt% of polystyrene.

So far, we have extensively produced particles with polymer-to-nanoparticle ratios of 10 : 1. We can also prepare particles with lower polymer-to-nanoparticle ratios. Figure 5.8 shows SEM images of particles with ratios of 9 : 1 and 2.3 : 1. We see that the particles with a polymer-to-nanoparticle ratio of 9 : 1 (Figure 5.8 A) have small cobalt ferrite nanoparticle aggregates around the particle surface that appears like webbing. At a polymer-to-nanoparticle ratio of 2.3 : 1, Figure 5.8 B, cobalt ferrite aggregates are clearly seen along the particles surface forming large clusters or even strands spanning from the top to the bottom of the particle. This visible change in particle morphology is also paired with an increase in average particle size from 1.9 μm to 4.8 μm for polymer-to-nanoparticle ratios of 9 : 1 and 2.3 : 1, respectively. We note that the dispersity still remains similar at 32% and 35% in both cases. Witschi *et al.* [188] saw an increased particle size with increasing amount of loaded drug, but they correlated it to a change in preparation method needed for drug incorporation. Here, the preparation for all samples is consistent, and the resulting particle dispersity ranges between 26 – 54%.

To confirm that the loaded nanoparticles are well-dispersed throughout the polymeric particle, we utilize a SEM that detects backscattered electrons (BSE) and is equipped with energy-dispersive X-ray spectroscopy (EDX). In back-scattered electron composition (BEC) SEM images, changes in the apparent intensity represent changes in the material density, i.e., darker regions are less dense than brighter regions. This coupled with

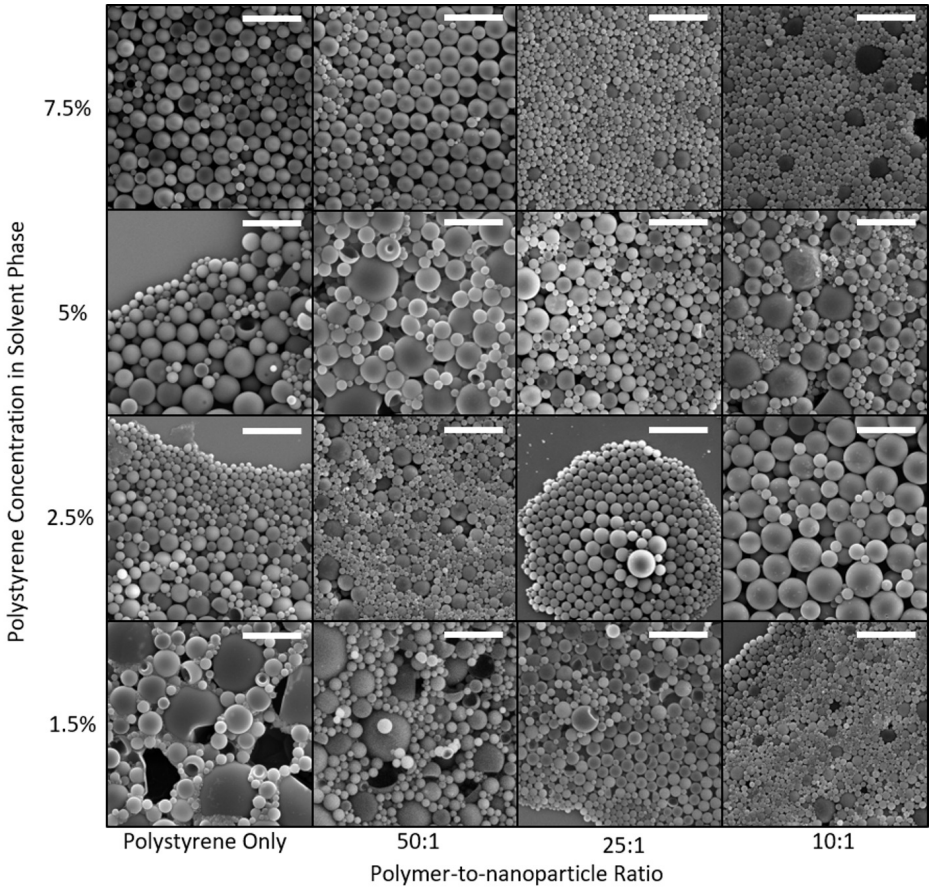


Figure 5.6: Representive SEM images for samples formed at varying the polystyrene weight percent to 7.5, 5, 2.5, and 1.5 wt% and the polystyrene to cobalt ferrite ratio from no polystyrene, 50 : 1, 25 : 1, and 10 : 1. All scale bars correspond to 10 μm.

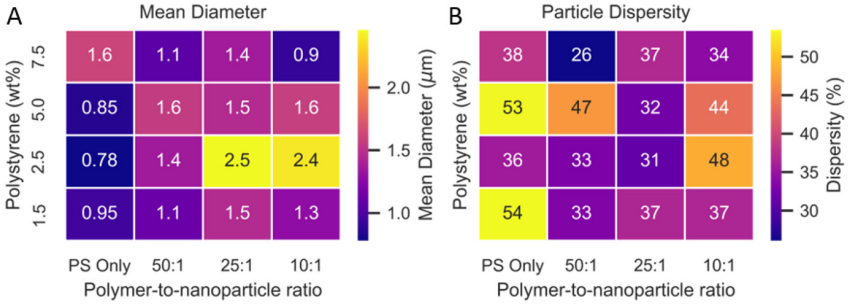


Figure 5.7: Matrix plots of the (A) particle diameter mean and (B) particle diameter dispersity, Đ, collected from corresponding SEM images in Figure 5.6. The column denoted 'PS Only' refers to non-loaded polystyrene particles.

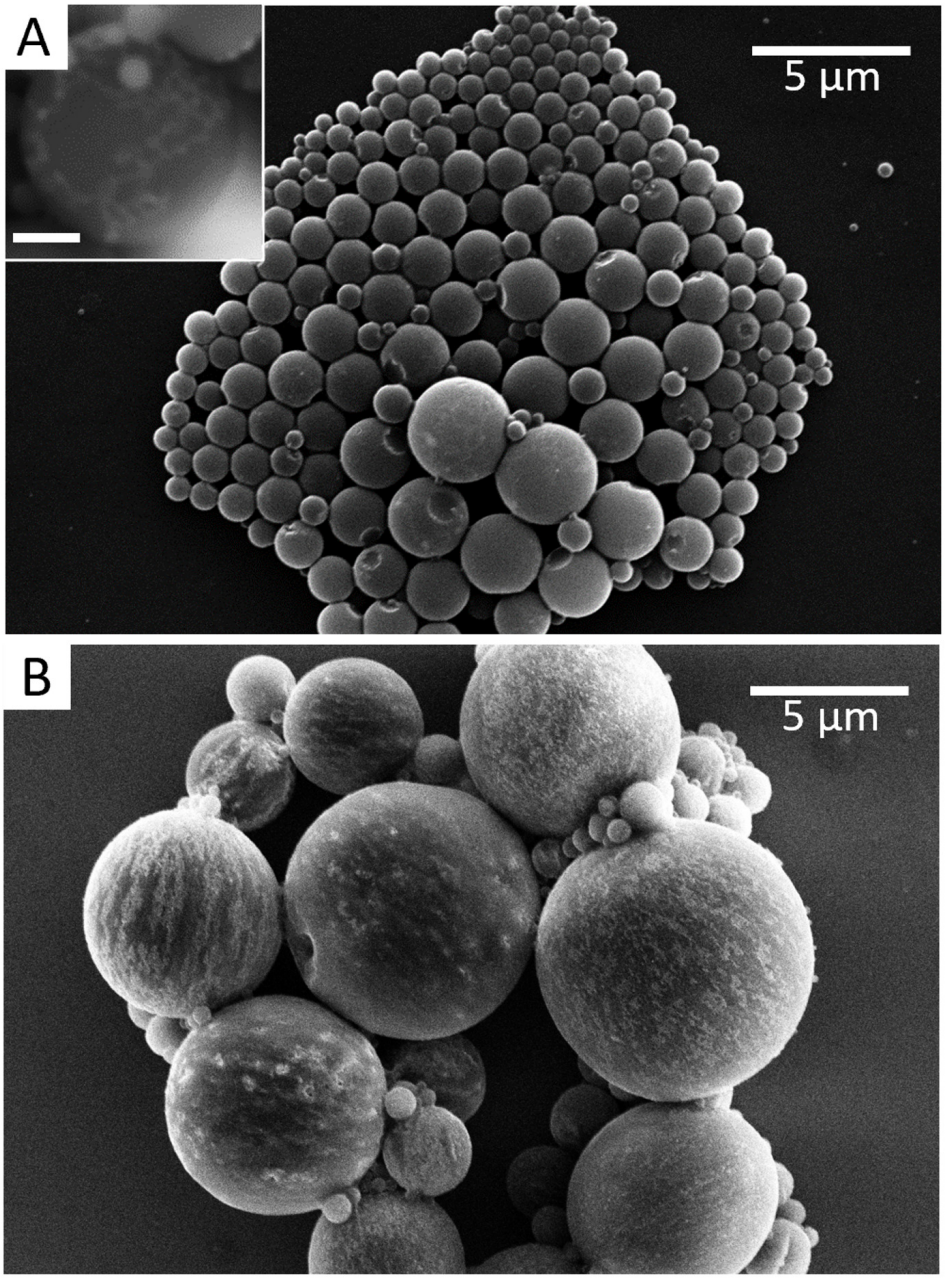


Figure 5.8: Representative SEM images of particles prepared with 2.5 wt% polystyrene and (A) 9 : 1 and (B) 2.3 : 1 polystyrene to cobalt ferrite. Inset in (A) is a BEC SEM image with a scale bar of 1 μm.

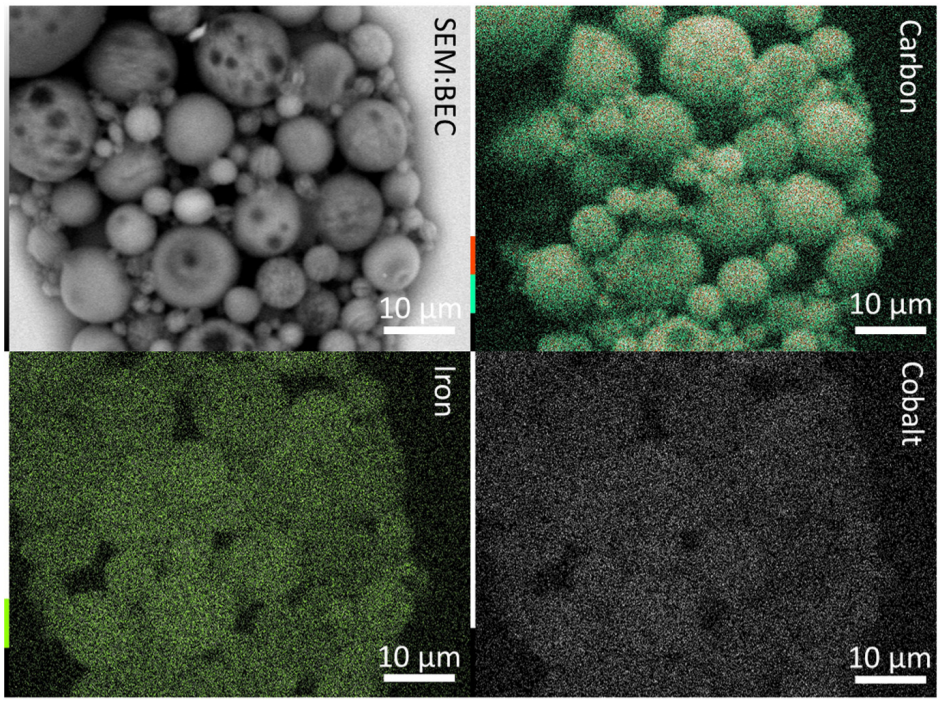


Figure 5.9: Energy-dispersive X-ray spectroscopy (EDX) of particles prepared with 5 wt% polystyrene in the solvent phase and a polymer-to-nanoparticle ratio of 9 : 1. The representative image of the sample, top left, is followed by the elemental maps related to the elements from the polymer, carbon, and nanoparticles, iron and cobalt.

EDX can determine elemental compositions of materials as shown in Figure 5.9. Based on the composition of polystyrene, C_8H_8, and cobalt ferrite, $CoFe_2O_4$, we observe the polystyrene matrix in the elemental carbon map and the nanoparticles in the elemental iron and cobalt maps. Since our sample substrate is a silica wafer, we can clearly distinguish the edges of the particles in all maps. It is apparent that our cobalt ferrite nanoparticles are evenly distributed throughout the polystyrene. Even so, we observe drastic density differences in the BEC SEM image not seen in the elemental maps. This indicates that the observed density difference is due to porosity present inside the composite particles.

5.3.4. Effect of Plasticization

In order to tune the internal structure from porous to solid, we add a plasticizer (tetrahydrofuran, THF) to the dispersion as described in section 5.2. When THF is added to a dispersion of composite particles, the particles become swollen allowing the polymer strands to minimize the interfacial energy between them and the surrounding medium [189] forming uniform spherical particles. After diluting the system and removing the THF, the particles re-solidify with a uniform, spherical shape. We explore the internal

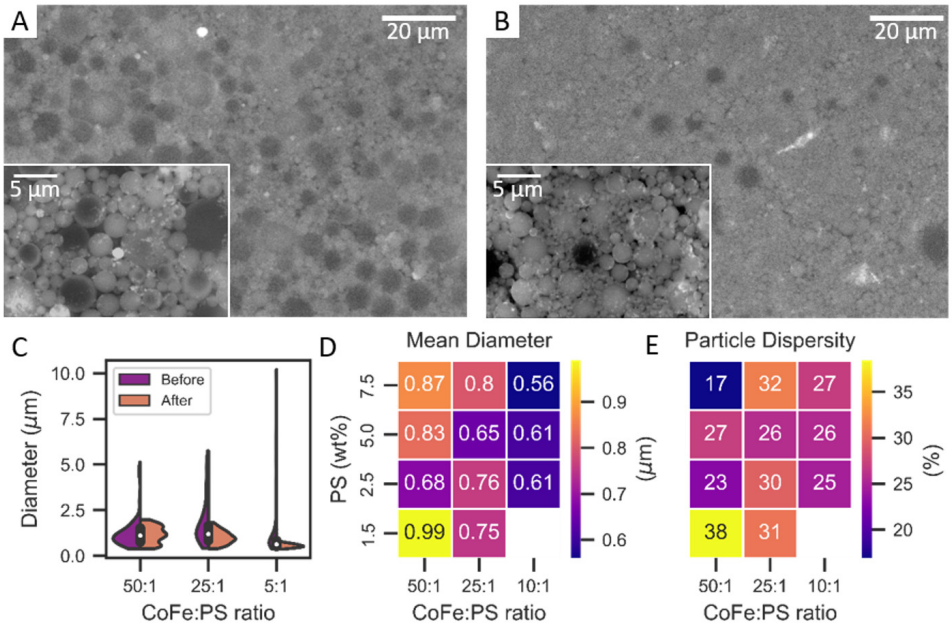


Figure 5.10: SEM images of back-scattered electrons (BEC) for 10:1 magnetic polystyrene particles (A) before and (B) after plasticization with THF. Insets in the bottom left of the images display BEC SEM images at higher magnifications to see individual particle details. (C) Violin plots of the particle diameter for samples at 2.5 wt% for various cobalt ferrite, CoFe, and polystyrene, PS, ratios before and after plasticization with THF. (D-E) Matrix plots over the PS concentration and component ratios (D) of the mean particle diameter and (E) the particle dispersity of each sample.

morphology using non-destructive BEC SEM. Figure 5.10 A is a BEC SEM image of loaded polystyrene particles before plasticization where you can see a disperse area of particles. Very bright objects are likely aggregates of the cobalt ferrite nanoparticles as iron and cobalt are much heavier than the polymeric components, carbon and oxygen, and appear brighter. Here, 94% of particles with diameters > 3 μm appear to have a hollow core where the middle of the particle is darker than the edges. The inset for Figure 5.10 A shows particles with a clear ring from the thicker shell wall. Figure 5.10 B shows particles after plasticization. Aside from the overall smaller particle size, darker patches are more often voids between particles that formed during SEM sample preparation which can be seen in the inset. In this case, the observed amount of particles with hollow cores has significantly decreased (< 5%).

To further compare samples before and after plasticization, we prepare several samples and collect SEM images before and after THF treatment. Representative sample images are found in Appendix A. We plot distributions of samples taken at 2.5 wt% polystyrene with different nanoparticle to polystyrene ratios in Figure 5.10 C. We see a dramatic shrinking of the distribution as well as the absence of diameters > 2.4 μm after plasticization. In fact, for a low polymer-to-nanoparticle ratio of 5:1, we find a very narrow particle distribution is present. In general, the mean particle diameter for all plas-

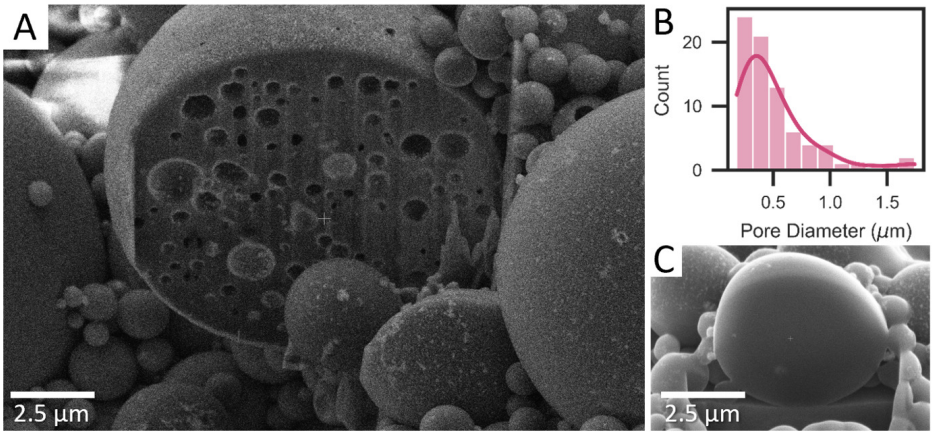


Figure 5.11: Internal structure of composite polystyrene particles. (A) Cross-section of a particle with a polymer-to-nanoparticle ratio of 5 : 1 without THF treatment. (B) Pore diameter analysis for the particle without THF treatment. (C) Cross-section of a particle with a polymer-to-nanoparticle ratio of 5 : 1 post THF treatment.

ticized samples is between 0.56 – 0.99 μm which is on average a decrease in diameter by half when compared to samples before plasticization. Similarly, the particle size dispersity decreases around 11% on average. This overall size decrease proves that the particles are not completely solid and that the voids are removed during plasticization.

We confirm the presence of pores inside the composite particles by imaging and slicing select particles with a focused ion beam (FIB) equipped SEM. Figure 5.11 A shows a SEM image of a polystyrene particle selectively sliced before THF treatment with a polymer-to-nanoparticle ratio of 5 : 1. We see the clear presence of pores throughout the particle cross-section. The internal pore diameter for this cross-section is on average 0.51 μm as described in Figure 5.11 B. After THF treatment, we observe an absence of pores throughout a particle cross-section as shown in Figure 5.11 C. This implies that the observed decrease in particle diameter corresponds to the removal of internal pores through the composite particles.

5.4. Conclusions

In this chapter, we present a facile method to produce composite polystyrene magnetic microparticles via an emulsion droplet evaporation technique. This technique creates solvent-in-water emulsion where the solvent phase is a relatively volatile solvent, DCM, containing various concentrations of polystyrene and cobalt ferrite nanoparticles and the continuous phase is an aqueous solution of SDS. We show this method results in spherical, hollow microparticles which can contain final concentrations of 30 wt% cobalt ferrite. Changing the SDS concentration during droplet evaporation can tune the particle morphology from spherical to crumpled and porous at high polystyrene to cobalt ferrite ratios. Uniform, spherical loaded microparticles are formed by adding a plasticizing agent, THF, to the sample in water which also reduces the overall particle dispersity. This

technique is a robust way to form loaded polymeric microparticles while also allowing control over the particle morphology. This is necessary for the preparation of magnetic polystyrene for further processing such as thermal stretching explored in chapter 6.

Acknowledgements

We thank Nitin Rajendra Madam for providing assistance with the preparation and characterization of loaded polystyrene samples throughout his MSc thesis. We also thank Duco Bosma for help characterizing loaded polystyrene with various SEM techniques as well as Hozanna Miro for assistance with FIB measurements.

Chapter 6

Anistropic Magnetic Polystyrene Particles Prepared via a Thermal Stretching Method

ABSTRACT:

Anisotropic magnetic particles are attracting great attention due to their unique properties and potential applications in microelectronics, cargo delivery, and medical imaging. However, the fabrication and control of anisotropic particles remain a challenging task. In this chapter, we use a thermal stretching method to produce magnetic anisotropic polystyrene particles. Magnetic polystyrene microspheres are embedded in a polymeric film that is subsequently stretched under heating. The recovered microparticles have elongated features in the stretching direction. During the stretching process, we apply a magnetic field to align the embedded magnetic nanoparticles while the polymer is pliable. We explore how the application of a magnetic field alters the behavior of the stretched microparticles via optical microscopy. Overall, this approach allows us to investigate the design of anisotropic particles with well-defined magnetic properties.

6.1. Introduction

Functional microparticles with embedded inorganic material are used in a wide range of applications from cosmetics [190], optics [191], and biotechnology [155, 156]. Microparticles containing magnetic components, in particular, are of interest due to their ability to be controlled remotely by magnetic fields [157–160]. The overall magnetic properties of these composite particles result from the type of embedded nanoparticle and their magnetic properties. Nanoparticles with a permanent magnetic moment, e.g., a single domain ferro- or ferri-magnetic particle, have properties that depend on the magnetocrystalline anisotropy (chapter 1) which determines the magnetic moments' reorientation rate. When nanoparticles are embedded inside a polymeric matrix, they are often oriented randomly (Figure 6.1 A) resulting in a ~ 0 net magnetization of the composite matrix [192]. When the magnetic nanoparticles have their magnetic moments similarly oriented inside the matrix, the composite material possesses a net magnetization dependent on the concentration of nanoparticles and orientation direction (Figure 6.1 B). Orientation of magnetic particles is possible under a magnetic field via two mechanisms. When the particle can move freely in its environment, the whole particle rotates such that the magnetic moment of the particle is parallel to the magnetic field direction as shown schematically in Figure 6.1 C. If a particle cannot rotate freely, i.e., it is bound in a solid matrix, the magnetic moment rotates internally with respect to the particles' crystallographic axis to be parallel to an applied field (Figure 6.1 D) [14, 21]. Depending on the situation, a particle can experience both types of realignment simultaneously, e.g., in a very viscous medium. Upon removal of the magnetic field, the particles relax back into their original state with relaxation times dependent on the particles' physical and material properties. Unbound particles generally experience Brownian relaxation where their thermal motion randomizes their orientation. On the other hand, Néel relaxation governs the internal realignment of the magnetic moment and is strongly dependent on the properties of the magnetic material[14]. For example, cobalt ferrite, a ferrimagnetic nanoparticle with a permanent magnetic moment, has a Néel relaxation time on the order of several years due to its large crystalline anisotropy [21] which makes it an ideal candidate for magnetization of composite materials.

These magnetic properties can be exploited to produce materials that posses a net magnetization. For example, recent advances in 3-D printing processes resulted in the production of composite materials with specific magnetization due to the application of a magnetic field at the extruder nozzle aligning the internal magnetic components before material solidification [193–195]. This 3D printing process can produce milimeter-sized robots capable of locomotion due to controlled deformation of the material under applied magnetic fields [196–198]. However, this method is not sustainable to go below the millimeter-scale. As a result, lithographic techniques are being investigated to form composite materials possessing a net magnetization on the micrometer-scale. Kim *et al.* [199] cross-link a magnetic composite photopolymer via a microscope set-up to form magnetic actuators on the scale of a few hundred microns. Recently, Zhang *et al.* [200] developed a method to form complex 3D magnetic actuators via cross-linking a composite photopolymer confined to a mold under a magnetic field. In general for these cases, the polymeric matrix is stationary contrary to typically colloidal systems which are often formed dispersed in an liquid medium under vigorous agitation, e.g., via emulsion

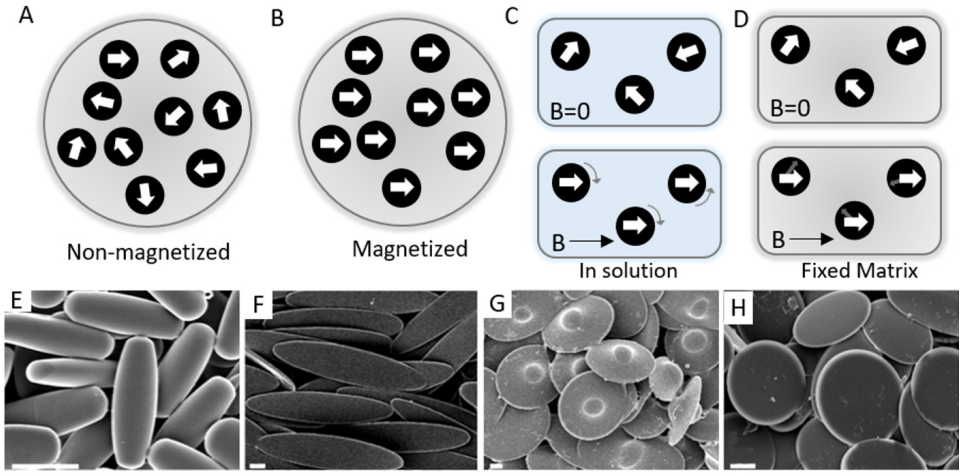


Figure 6.1: Diagram of a composite microparticle with embedded magnetic nanoparticles in a (A) non-magnetized and (B) magnetized state. Diagrams of different alignment mechanisms for particles in (C) a liquid medium and (D) a fixed matrix. SEM images of various particle shapes achievable via thermal stretching methods: (E) rods, (F) elliptical disks, (G) UFOs, and (H) circular disks. All the scale bars are 2 μm. Adapted from [201]. © Copyright 2007 National Academy of Sciences.

polymerization [157, 158, 163] or emulsion droplet evaporation techniques (chapter 5). For colloidal systems, magnetization of the microparticles during synthesis in a liquid medium is not yet possible.

One possible strategy to magnetize a colloidal system is to physically trap or embed the composite microparticles in a solid matrix. van Berkyum and Erné [192] trapped composite silica and cobalt ferrite microparticles by freezing the surrounding liquid medium in order to completely demagnetize the microparticles rather than magnetize them. Another interesting immobilization technique available not only restricts particle movement for (de)magnetization but also reforms the particles into anisotropic shapes. This technique is based on a thermal stretching method developed by Ho *et al.* [1, 202] who originally used pure polystyrene microspheres. In this method, polymeric films with embedded spherical polystyrene particles were stretched using biaxial forces and heated above the particle's glass transition temperature which forms ellipsoidal microparticles of specific axial ratios determined by the stretched films' draw ratio. The stretching of the particle is in part due to the fact that the polymer is un-crosslinked allowing for easier deformation. Champion *et al.* [201] refined this approach by varying the heating and stretching phases to obtain a wide range of shapes with some examples as rods, disks, and even UFOs (Figure 6.1 C-F). Recently, Lo *et al.* [189, 203] simplified the approach even further to generate ellipsoids with sharp or blunt ends by simply stretching the particle embedded films simply with a weight linked to a binder clip. When this approach is applied to composite microparticles, Güell *et al.* [204] fabricated Janus-like ellipsoids by applying a non-uniform magnetic field along the stretching direction. However, they only form the Janus-like particles in a small section of the stretching film limiting their particle production, and they utilize a solvent bath rather than heat to plasticize and

stretch the particles. This is due to the commercial based magnetic polystyrene spheres they use which are formed from a polystyrene core coated with magnetic nanoparticles finally coated by another polymeric material where the additional polymers on the surface limits the effectiveness of the thermal stretching method due to adhesion between the film and the added polymer coating [205, 206]. Recently, we developed a particle preparation method (chapter 5) to form composite magnetic un-crosslinked polystyrene microparticles with magnetic loading up to 30 wt%.

In this chapter, we embed the magnetic polystyrene microspheres designed in chapter 5 in poly (vinyl-alcohol) (PVA) films to form ellipsoidal particles through thermal stretching. The addition of a magnetic field during this process allows us to align the magnetic moments of the individual magnetic nanoparticles loaded inside the polystyrene matrix. When all of the nanoparticles are aligned, we potentially produce a polystyrene-based ellipsoidal microparticle with an overall magnetic moment. Removing the PVA film frees the particles for further use as a colloidal dispersion. Here, we explore the effects of the PVA film's draw ratio and application of a magnetic field during stretching on the resultant anisotropic microparticles. This procedure can be adopted to produce a variety of shapes achievable with any thermal stretching method and generate large quantities of magnetic anisotropic microparticles for a variety of soft matter applications.

6.2. Experimental Methods

6.2.1. Particle Synthesis

Magnetic polystyrene particles were synthesized following the procedure outlined in section 5.2. Briefly, 7.5 wt% polystyrene in dichloromethane (DCM) at a 10 : 1 and 50 : 1 polystyrene to cobalt ferrite ratio was sonicated to form an oil-in-water emulsion. DCM was evaporated from the formed emulsion droplets under low pressure. Tetrahydrofuran (THF) was added to the formed particle suspension for 20 s followed immediately by a 4-fold dillution to solidify the formed porous particles. The resulting particles were washed three times in water via centrifugation. For samples without cobalt ferrite, we followed the same procedure omitting the nanoparticles and using 7.5 wt% polystyrene in DCM.

6.2.2. PVA Film Preparation

Films with embedded polymeric particles were prepared following a method modified from Ref. [189]. A 20 mL aqueous dispersion containing 0.01 wt% (loaded) polystyrene particles was heated to 80°C. At temperature, 1 g of poly(vinyl alcohol) (PVA, 145,000 mW) was added and magnetically stirred until the PVA dissolved completely, typically 1 hour. The solution sat without stirring for at least 3 hours to remove bubbles. Inside a round 8.5 cm plastic petri dish, 10 mL of the solution was poured and placed on a level surface overnight for the water to evaporate. The films prepared as described resulted in films with thicknesses around 50 μm devoid of bubbles and lumps.

6.2.3. PVA film Stretching

Dry PVA films were cut into (3.5 × 1) cm^2 strips which provides a stretching area of (2 × 1) cm^2. Custom made clamps were attached to the ends of the film with a small piece of sandpaper and tightened. Films were placed in an oven at 140°C with a 380 g weight

Table 6.1: Particle morphology results for stretched magnetic microparticles. Here, "NP conc." denotes the concentration of cobalt ferrite nanoparticles within the particles.

NP conc.	Applied field	Draw ratio	Major axis (μm)	σ_{major}	Minor axis (μm)	σ_{minor}	Axial ratio$_{exp}$	Axial ratio$_{calc}$
No NP	No	2.3	4.5	2.2	1.3	0.7	3.8 (34%)	3.5
2 wt%	No	1.9	3.6	1.6	1.1	0.4	3.1 (26%)	2.6
2 wt%	Yes	1.8	3.5	1.4	0.9	0.6	3.9 (41%)	2.4
10 wt%	No	3.2	3.3	1.8	1.6	0.6	2.5 (48%)	5.7
10 wt%	Yes	2.5	2.5	1.4	1.5	0.6	1.7 (18%)	3.9

attached to the bottom and allowed to stretch for 25 minutes. In order to collect uniform stretching areas, the films were marked with lines every 0.25 cm before stretching.

6.2.4. Particle Recovery

Stretched films were trimmed to only their stretched regions and rinsed with isopropanol (IPA) to remove the marker from the surface. The strips were submerged in a 20 v/v% IPA and water mixture at 60°C to dissolve the PVA film. The dispersion of particles was washed via centrifugation at high speeds (13,000 rpm for 1 hour), and redispersed in the IPA-water mixture twice. A final wash cycle was done to redisperse the particles in distilled water.

6.2.5. Characterization

Scanning electron microscopy (SEM) measurements were preformed on a JEOL JSM-6010LA. SEM samples were prepared by placing 2.5 μL of a diluted particle dispersion onto a cut silica wafer, allowed to dry, and sputter coated with a $\approx$ 5 nm gold layer. Particle dynamics were followed via an optical microscope (Nikon Eclipse E600pol) equipped with a 50x objective and a CCD camera. Optical microscopy samples were prepared inside flat rectangular capillaries (Vitrocom 0.05 x 1.00 mm) and sealed with wax on a microscope slide. A uniform magnetic field was applied to the sample with a custom magnetic set-up. Image analysis was preformed with ImageJ Fiji [182]. We fit images of the stretched particles to an ellipse with a major axis, a, and minor axis, b, and determine the axial ratio by $\frac{a}{b}$. The reported angle is defined as the angle between the major axis and a line parallel to the x-axis of the image. A table of various sample parameters is provided in Table 6.1.

6.3. Results and Discussion

To prepare anisotropic polystyrene particles, we use a thermal stretching method outlined in Figure 6.2. In this method, we first prepare PVA films loaded with polystyrene spheres by drying a PVA solution mixed with polystyrene microspheres with average diameter of 1.6 μm. We then fix the film with two clamps, load it with 380 g of weight, and allow it to stretch in an oven at 140°C for 25 minutes. As a result, the PVA film is elongated along the direction of stretching. Since the glass transition temperature of polystyrene is approximately 100°C, the polystyrene particles deform with the film. For polystyrene particles loaded with magnetic nanoparticles, such as 30 nm cobalt ferrite, application of a strong magnetic field during their confinement in the PVA film while stretching may

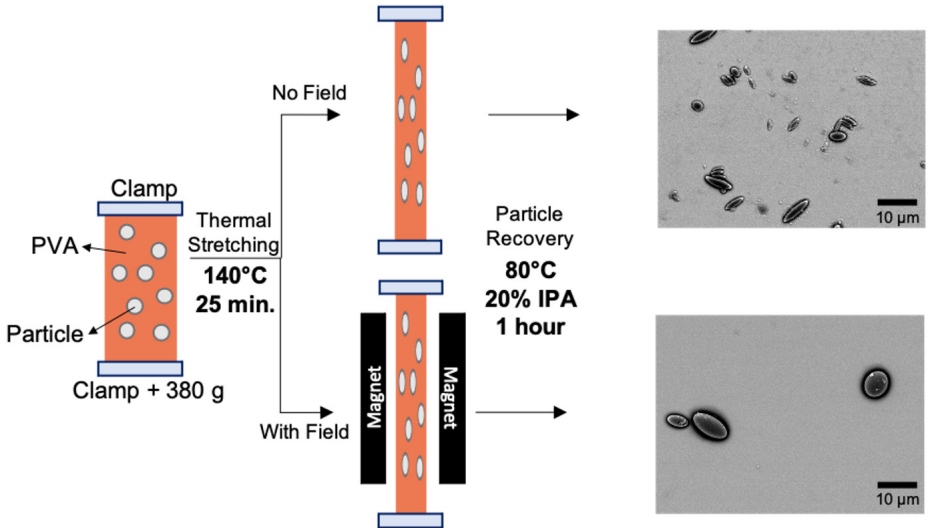


Figure 6.2: Schematic illustration (not to scale) of the applied thermal stretching method to generate anisotropic (loaded) polystyrene particles with two pathways: with and without an applied magnetic field. Particle recovery is seen from the SEM images of two samples prepared following the schematic.

allow for an overall magnetization of the particles [192]. After the stretching process, the particles are recovered by selectively removing the PVA film in an IPA/water solution.

To investigate the shape of the particles obtained by the thermal stretching process, we first investigate how pure polystyrene microparticles behave. Figure 6.3 A shows an SEM image of initial, un-stretched polystyrene particles prepared as described in chapter 5. This method produces a spread of particle diameters with an average of 1.6 μm and a dispersity of Đ= 31% (Equation 5.1). We stretch a film containing the particles for 25 minutes which results in a draw ratio of 2.3. Where the draw ratio is defined as:

$$draw\ ratio = \frac{final\ film\ length}{initial\ film\ length}. \tag{6.1}$$

Figure 6.3 B shows the resultant particles from the stretching process. We clearly observe the presence of ellipsoidal particles with sharp tips throughout the sample. In contrast, Lo *et al.* [189] observed the formation of sharp-tipped ellipsoids only when a pre-annealing step was implemented before stretching. Without the pre-annealing step, only blunt-tipped particles formed. Since the driving effect of the thermal stretching process stems from the differences in glass transition temperature of polystyrene and PVA [189, 202], we speculate that the molecular weight of our polystyrene (40,000) and PVA (145,000) polymers is the main cause of the formation of sharp-tipped particles without an annealing step due to the slower deformation of the PVA film under stretching. Additionally, there is a large spread of particle sizes which we further characterize by by fitting the particles to 2D ellipses with a major and minor axis length defined by:

$$\frac{x^2}{a^2} + \frac{y^2}{b^2} = 1 \tag{6.2}$$

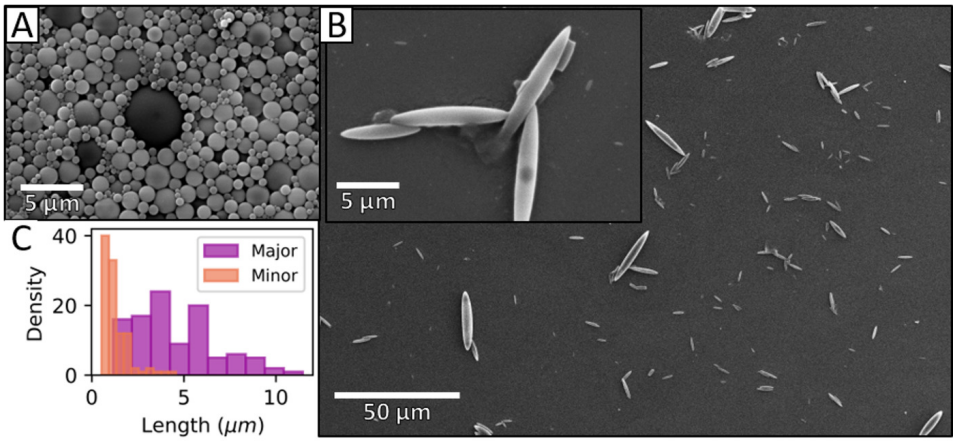


Figure 6.3: (A) SEM image of non-magnetic polystyrene particles prepared via the emulsion droplet evaporation method. (B) SEM image of stretched non-magnetic particles with inset of higher magnification. (C) Distribution of the a and b axial lengths for stretched particles.

where $2a$ and $2b$ is the length of the major and minor axis, respectively. We measure the axial lengths of 150 particles and plot the histogram in Figure 6.3 C. We observe a large distribution (Đ= 48%) of the major axial length for the particles with an average of 4.5 μm and a minor axial length of 1.3 μm. This observed increase in $Đ$ after stretching is attributed to the non-uniform stretching of the PVA film. In general, the center of the film stretches more than near the clamps which in turn creates a gradient in the particle stretching [202]. Additionally, we can further observe the non-uniform stretching of the particles by comparing the draw ratio of the film to the axial ratio. For polystyrene particles, Lo *et al.* [189, 203] show that the draw ratio, n can be closely correlated to the resultant axial ratio by:

$$\frac{a}{b} = n\sqrt{n}. \tag{6.3}$$

For our non-magnetic polystyrene, we find an average experimental axial ratio of 3.8 (Đ= 38%) compared to the calculated ratio of 3.5. While our experimental range encompasses the calculated axial ratio, we observe a large dispersity within the experiment which is likely due to the non-uniform stretching throughout the film.

To investigate the stretching process for magnetic composite particles, we prepare two types of particles with low and high magnetic contents of 2 wt% and 10 wt% cobalt ferrite inside the polystyrene. Figure 6.4 A-B shows stretched particles containing 2 wt% and 10 wt% cobalt ferrite. Similar to the non-magnetic particles, we achieve a higher dispersity in the major axial length after stretching occurs where Đ= 44% and 54% for particles with 2 wt% and 10 wt% cobalt ferrite, respectively. Due to slight differences in the film thicknesses, the draw ratios were difficult to standardize during the thermal stretching process where n = 1.9 and 3.2 for particles with 2 wt% and 10 wt% cobalt ferrite (Table 6.1). In contrast to their non-magnetic counterparts, the stretched magnetic particles no longer fell within the predicted axial ratio range, with low concentrations of

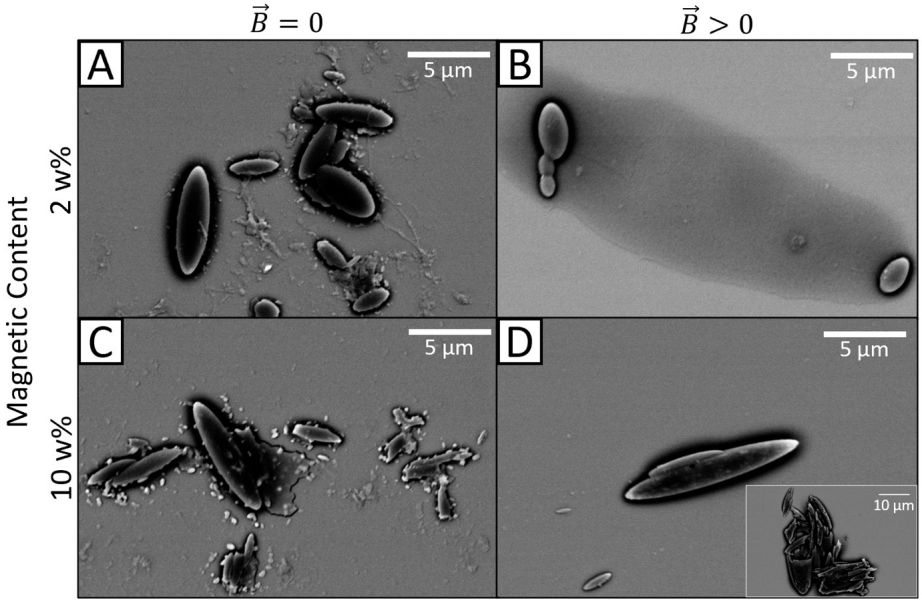


Figure 6.4: Representative SEM images for the four different stretched magnetic polystyrene samples with magnetic contents of (A) 2 wt% and (B) 10 wt% in the absence of an external field, and (C) 2 wt% and (D) 10 wt% in the presence of an external field. Inset image at a different scaling to highlight anomalies in the samples with higher magnetic content.

cobalt ferrite in the particles resulting in axial ratios greater than the predicted value, and high concentrations of cobalt ferrite in the particles resulting in axial ratios lower than the predicted value. It is possible that this results from the presence of the cobalt ferrite filler in the polystyrene matrix. At a 10 wt% concentration of cobalt ferrite, the added composite can raise the overall glass transition temperature of the microparticle [207]. Additionally, if nanoparticles are present on the microparticle surface, this can increase the thermal stability of the PVA matrix directly surrounding the microparticle [208], which reduces the overall effectiveness of the thermal stretch.

To produce composite microparticles with a permanent magnetic moment, we apply a strong magnetic field by sandwiching the film between two permanent magnets. In general, magnetic nanoparticles rotate their magnetic moments via either Brownian, Néel, or a combination of the two processes. In zero-field environments, the time scales for Brownian relaxation of the magnetic moment, τ_B, is defined by :

$$\tau_B = \frac{3\eta V_H}{kT} \tag{6.4}$$

where η is the surrounding viscosity, V_H is the hydrodynamic volume, k is the Boltzmann constant, and T is temperature. In this case, the relaxation time is then restricted in highly viscous systems. For example, polystyrene melts have a viscosity on the order of $\eta = 1.3 \times 10^5$ Pas [209] where the τ_B is then on the order of several years. Additionally, Trisnanto *et al.* [210] show that nanoclusters in viscous glycerol solutions align first with

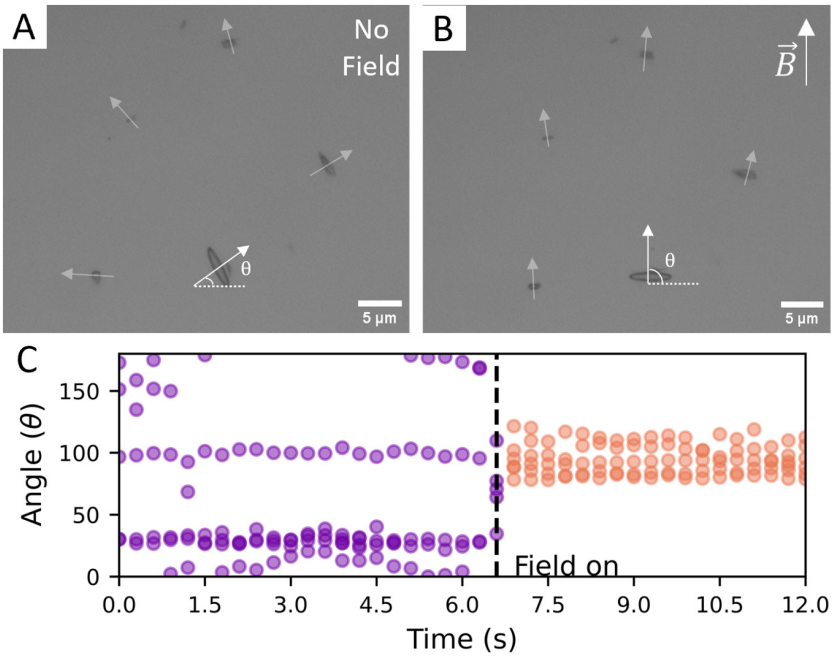


Figure 6.5: Optical microscopy stills from a movie of ellipsoids stretched in the presence of an applied field. (A) Particles in the absence of an external applied field and (B) with an applied magnetic field of 3.5 mT along the y-axis. Arrows are drawn along the minor axis of the ellipses to guide the eye. The angle, θ, is determined from the angle of the minor axis to a line parallel to the x-axis as shown schematically on top of the images. (C) The measured angle, θ, for at least 6 particles over time where a 4 mT magnetic field is applied at 7 s for the particles in the move stills.

the magnetic field via Néel processes followed by the slower Brownian process. Therefore, we note that for the microparticles to obtain a net magnetization, we rely on the rotation of cobalt ferrite nanoparticles magnetic moments as we apply a magnetic field. Furthermore, the selection of cobalt ferrite nanoparticles, rather than alternative magnetic materials, is due to its large crystalline anisotropy [21] which allows for a significantly large Néel relaxation time, τ_N, on the scale of several years in zero field environments. Figure 6.4 C-D displays SEM images of the resultant ellipsoidal particles obtained after thermal stretching under an applied magnetic field perpendicular to the stretching direction. We find that the films stretch less when between the magnets under the same stretching conditions. We note that for film strips cut from the same dried PVA film the thickness varied minimally, between 2-4 μm. Therefore, the decrease in the ratio is likely due to the restriction of stretching when sandwiched between the two magnets. We also observe that for microparticles with a higher magnetic content, the draw ratio is larger, but the resultant axial ratio decreases. In Figure 6.4 D, we find the presence of fractured and broken ellipsoidal particles which is highlighted in the inset. Therefore, it is possible that particles with high axial ratios fractured during particle recovery due to the high

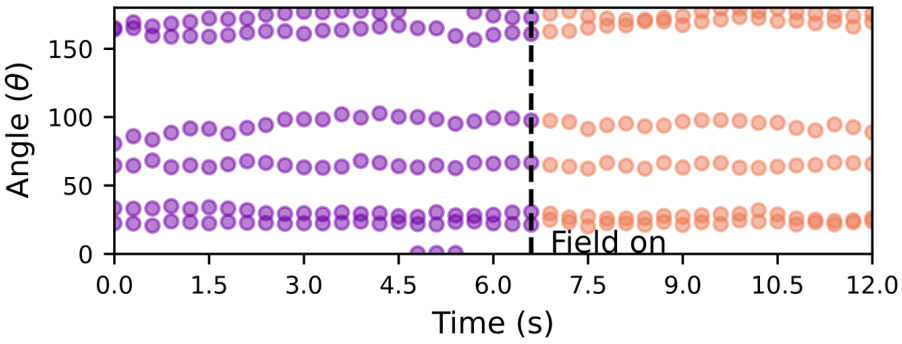


Figure 6.6: The measured angle for particles, stretched in the absence of an applied field, over time where a 3.5 mT magnetic field is applied at 7 s.

centrifugal speeds or breakage during the PVA film dissolution. This would contribute to a lower measured axial ratio for those samples.

In order to investigate the internal alignment of the magnetic content of the microparticles, we apply a low uniform magnetic field to particle dispersions and track their rotational behavior. Specifically, we prepared an aqueous dispersion of particles with 10 wt% magnetic content and applied a low magnetic field (3.5 mT) along the positive y-direction. We followed the particle dynamics via a particle tracking algorithm paired with the ImageJ Fiji software [182] as described in the methods. Figure 6.5 A shows a still frame from a movie of magnetic ellipsoids in the absence of an applied magnetic field. In general, the particles are all randomly oriented in the frame. When a magnetic field of 3.5 mT is applied, all of the particles orient parallel to each other as shown in Figure 6.5 B. We can track the effect of the magnetic field by measuring the angle, θ, of the particles' minor axis with respect to a line parallel to the x-axis indicated by the white arrows in the images. In Figure 6.5 C, we can see the various angles of the five particles and how they all orient. When the magnetic field is applied at 7 seconds, all particles rotate such that their minor axis is approximately at a 90° angle with the x-axis. This suggests that there is a preferential orientation of magnetic moments parallel to the minor axis of the particle which corresponds well to our field orientation applied perpendicular to the stretching direction. To confirm that this occurs only for particles stretched under an applied field, we track the behavior of ellipsoids with 10 wt% magnetic content stretched in the absence of a magnetic field. Figure 6.6 shows the angular alignments of a set of particles from optical microscopy with a 3.5 mT magnetic field applied after 7 s. Here, we did not observe any alignment behavior and the particles instead remained relatively with the same orientation.

6.4. Conclusions

In this chapter, we successfully fabricate anisotropic magnetic polystyrene particles via a thermal stretching method. PVA films embedded with polystyrene microspheres are

thermally stretched resulting in embedded ellipsoidal magnetic polystyrene particles. Anisotropic particles with and without internal magnetic alignment can be prepared depending on whether the embedded PVA film is exposed to a magnetic field during the thermal stretching process. Afterwards, the anisotropic magnetic polystyrene can be released from the PVA films for further use. In the future, the ability to scale up this process and apply magnetic fields along different orientations during stretching could result in a facile way to create micron-sized particles imbued with a controllable permanent magnetic moment which would extend the potential applications of these particles. We explore further the outlook for these types of magnetic microparticles in chapter 7.

Acknowledgements

We thank Nitin Rajendra Madam for providing assistance with the preparation and characterization of loaded polystyrene samples throughout his MSc thesis. We also thank Giovanna Bruscia for preliminary investigation into polystyrene stretching mechanisms.

Chapter 7

General Conclusions and Outlook

ABSTRACT:

In this chapter, we summarize the major topics and findings of this thesis. We also explore some additional topics, limitations, and outlooks that did not get a place in the previous chapters.

7.1. Conclusions

This thesis delves into the optimization and utilization of magnetic microparticles as functional materials, demonstrating how our current repertoire can be amplified for enhanced performance. In one case, we examine spherical assemblies of microparticles via the evaporation of a dispersion droplet. Spherical assemblies are well-studied for non-magnetic, isotropic microparticles and find applications in opto-electronics and photonics [66], but anisotropic microparticles assemble into diverse structures dependent on their shape [30]. Within this thesis, we utilize a prominent anisotropic particle shape, called the superball, which can be formed during the synthesis of hematite microparticles [24, 67, 108]. Since hematite microparticles have a permanent magnetic dipole moment, additional inter-particle interactions occur during their assembly. Therefore, in order to decouple the effect of particle shape from dipole-dipole interactions, we synthesized a non-magnetic superball by coating the magnetic hematite with silica and etching away the hematite core particle. In chapter 2, we assembled hollow superball shells with different shape parameters inside an evaporating droplet. We found that the hollow superballs assembled into spherical macrostructures with a paracrystalline internal structure reflecting their expected rhombohedral C_1 bulk packing. Retaining the hematite core of the superball particle allows us to further direct particle assembly via application of a magnetic field. In chapter 3, we assemble magnetic superballs in the presence and absence of an external magnetic field. Interestingly, the additional inter-particle interactions due to the magnetic core do not hinder the formation of the rhombohedral structure. However, application of a magnetic field forces the formed structure into a base-centered monoclinic (BCM) lattice whose crystallinity can be tuned with the magnetic field strength. Additionally, hematite is a photocatalyst; a bulk propriety that can be exploited for a variety of applications from water splitting [123] to pollutant degradation [36]. Furthermore, colloidal-scale photocatalysts propelled through a fuel containing solution and may serve as controllable micro-robots [39]. In chapter 4, we enhance the active motion of hematite superballs via particle calcination. After one minute of photo-catalysis induced propulsion, we found calcination increases the mean-squared displacement up to 87-fold.

In general, composite magnetic microparticles have a wide range of applications such as in environmental remediation [158–160] or in bio-medicine [155–157]. In this regard, there is a large desire for complete control over the particle design especially in regards to particle shape and the addition of a net magnetization. In the last part of this thesis, we focus on the preparation of magnetic microparticles in an attempt to provide this desirable tunability. In chapter 5, we fabricate composite polymeric micro-spheres that contain magnetic nanoparticles distributed throughout the polymeric matrix. The combination of polymer and nanoparticles allows the formation of large ($> 5\ \mu$m) magnetic particles. While this method imbued tunability to the particle size, porosity, and magnetic content, we still lack control over shape anisotropy and net magnetization of the particle. In chapter 6, we introduce a thermal stretching technique to elongate the magnetic micro-spheres into ellipsoidal shapes. We speculate that the addition of a magnetic field during particle stretching allows the magnetic nanoparticles to align parallel to the field lines while the polymer is in a malleable state. We have shown the ability to form particles with easy control over various proprieties of the microparticle, i.e., shape, porosity, and

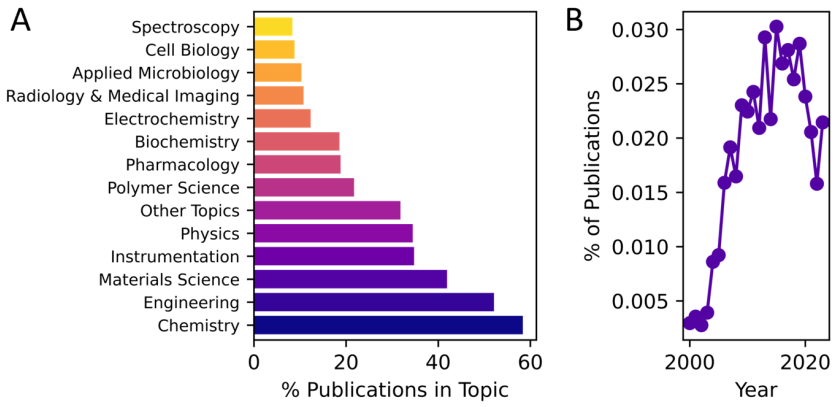


Figure 7.1: Publications regarding "Magnetic Microparticles" collected from Clarivate Web of Science publication database. (A) Publications organized by tagged topic in percent out of total publications. (B) Percentage of publications over the last 50 years cross-referenced and normalized to the number of published papers in the "Chemistry" topic. Certain data included herein are derived from Clarivate Web of Science. ©Copyright Clarivate 2023. All rights reserved.

magnetic content.

7.2. Outlook

7.2.1. Self-assembly of Anisotropic Superball Particles

Droplet-based superball particle assemblies show great promise in the design of functional materials, as their shape parameter greatly controls their resultant assembled structure (chapter 2 ,3). Opal-like materials formed from assembled spheres have already found applications in photonics and micro-electronics due to the uniform arrangement of monodisperse spheres [29, 95, 102]. In a similar vein, assembled hollow superballs could act as alternative structured wave-guides or photonic crystals with a much larger structural diversity than what can currently be achieved by isotropic spheres. This could have unique implications in areas of research such as counterfeit detection which commonly applies photonic "holograms" on banknotes used around the world today [211, 212]. However, the method we employed to produce freestanding hollow superball assembles still results in polycrystalline structures which may hinder potential applications in precision-based photonics. One possible solution to counteract the polycrystallinity is to tune the inter-particle interactions during assembly inside the droplet by reducing the Debye screening length at the particle surface through salt addition. Though, this may have undesired consequences, such as salt crystals throughout the assembly, due to the increasing salt concentration during droplet evaporation [213]. On the other hand, we show that retaining a permanent magnetic moment inside the superball core results in droplet-based assemblies with tunable structures related to the particle shape and the application of a magnetic field. While this still forms photonic crystal-like structures, the potential magnetic applications may prove more fruitful. If the overall assembled

structure is imbued with a net magnetic moment, these freestanding assemblies could have potential to serve as miniature magnetic stirring bars in restricted systems, such as microfluidic channels or wells.

7.2.2. Active Hematite Microswimmers

Hematite microparticles are of interest due to their ability to propel themselves when activated by a light source in a fuel solution. Peanuts [120], superballs [119, 141], and ellipsoids [214] have all been show to have the ability to perform complex tasks with a focus on cargo delivery with steering done by an external magnetic field. While we developed a method to increase their propulsion power significantly, their current functionality is mainly restricted to simple cargo transport. However, decorating the surface of hematite with gold nanoparticles could provide a pathway for more complex tasks due to gold's ability to easily functionalize with nucleic acids. Then, active hematite could find strong roles in the biomedical field as, for example, DNA- or RNA-based vaccine carriers which has recently become a very popular topic [215–218]. To achieve this, further exploration of the attachment and stability of gold nanoparticles on calcined hematite is required as well as the active performance of these particles in biological conditions.

7.2.3. Anisotropic and Magnetic Particle Preparation

So far, the applications and preparation methods explored in the previous chapters represent only a small window into the world of anisotropic and magnetic colloidal particles. In order to explore the topic further, we carried out a search for publications related to magnetic microparticles through the Clarivate Web of Science publication database. Figure 7.1 A provides a summary of publications relating to these topics over the last 50 years contained in this database. Here, we observe the variety of different topics and fields tagged in at least 7% of publications. This already highlights the broad range of applications available for magnetic microparticles even when ignoring more niche research areas. Additionally, we observe an increase in the number of publications since the early 2000s in Figure 7.1 B. However, the literature reviewed for this thesis revealed one common theme regarding magnetic microparticles: there is no standard synthetic method to produce particles with tunable shape and magnetization. Even though we have shown potential strategies to provide this desired control during particle preparation, we are still hindered by the scalability and control over the magnetization. As discussed in chapter 6, we rely on a thermal stretching method to deform spherical magnetic polystyrene particles embedded in a film under high (140°C) temperatures which limits the amount of stretching we can achieve before the film itself becomes deformed. One alternative possibility could be to use an alternating magnetic field to generate localized heating of the magnetic nanomaterials, as the nanomaterials experience friction due to the re-alignment of their internal spins[219, 220]. This would fully utilize the composite microparticles as the polymer becomes malleable around the nanomaterials and can then deform with the stretched film. Additionally, localized heating inside the microparticles would allow for the preparation of much thicker or layered films to increase the overall yield of anisotropic microparticles.

Another limitation our current approach has is the specific shapes achievable via stretching mechanisms, e.g., ellipsoids, discs, and spheres. Therefore, the ability to design

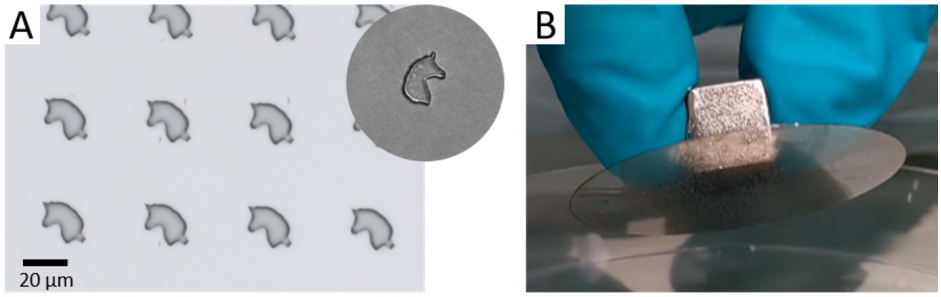


Figure 7.2: Colloidal particles generated via lithographic techniques. (A) Unicorn shaped particles as prepared on a substrate where the inset shows a particle free in an aqueous solution. (B) Inclusion of high concentrations of magnetic nanoparticles inside the photopolymer film of < 100 μm which provide enough magnetic strength to hold the weight of the glass substrate to the magnetic.

functional, anisotropic, and magnetic colloidal particles that can complete complex tasks in various environments required for different research areas has not yet been achieved. One possible route to provide ample control over the prepared particle is via lithographic techniques. In this process, a thin layer (< 10 μm) of a photoresist on a removable substrate is exposed to patterned light to systematically cross-link the photoresist. The now cross-linked particles can be freed from the substrate for use as a colloid. Indeed, the recent appearance of so-called "lithoparticles" demonstrates the broad range of achievable shapes via this technique [221–223]. We have also previously explored this technique as shown in Figure 7.2 A. Here, we present unicorn-shaped particles generated using this lithographic approach, with the maximum size dimension being roughly 30 μm. It is clear that we already have great control over a particle's 2D structure, although there is not yet a magnetic contribution. As a result, the capacity to embed homogeneous dispersions of magnetic nanomaterials in photopolymers would make a significant contribution to achieving full control over particle features. Recently, various tests have been carried out to create homogeneous films of composite photoresists in our lab (Figure 7.2 B) along with others [16, 224–226]. Even so, these films still contain nanomaterial aggregates ($d_{\text{aggregate}} \geq 100$ nm) close to the scale of a microparticle which hinders the cross-linking process. Therefore, well-defined micron-sized, composite particles are not yet achievable with the current techniques. One of the largest limitations of this method is the aggregation of the incorporated material before cross-linking can be preformed. A possible strategy to mitigate this aggregation would be to bind the incorporated material directly to the backbone of the photopolymer, but this may prove synthetically intensive. An alternative could be to dissolve the photopolymer and incorporated material in a suitable solvent where controlled evaporation of the solvent does not induce significant aggregation of the incorporated materials. Overall, we can easily produce magnetic and anisotropic colloidal particles with specific functionalities in mind, and we may soon be able to develop a comprehensive library of particles with any shape and property we can imagine.

Bibliography

1. Ho, C. C., Keller, A., Odell, J. A. & Ottewill, R. H. Preparation of monodisperse ellipsoidal polystyrene particles. en. *Colloid and Polymer Science* **271,** 469–479. ISSN: 1435-1536 (May 1993).
2. Green, A. E., Chiang, C.-Y., Greer, H. F., Waller, A., Ruszin, A., Webster, J., Niu, Z., Self, K. & Zhou, W. Growth Mechanism of Dendritic Hematite via Hydrolysis of Ferricyanide. *Crystal Growth & Design* **17,** 800–808. ISSN: 1528-7483 (Feb. 2017).
3. Jones, R. A. L. *Soft Condensed Matter* en. ISBN: 978-0-19-850589-1 (OUP Oxford, June 2002).
4. *Principles of Colloid and Surface Chemistry, Revised and Expanded* 3rd. en (eds Hiemenz, P. C. & Rajagopalan) ISBN: 978-1-315-27428-7 (CRC Press, 1997).
5. Derjaguin, B. V. A theory of the heterocoagulation, interaction and adhesion of dissimilar particles in solutions of electrolytes. en. *Discussions of the Faraday Society* **18,** 85–98. ISSN: 0366-9033 (Jan. 1954).
6. Verwey, E. J. W. Theory of the Stability of Lyophobic Colloids. *The Journal of Physical and Colloid Chemistry* **51,** 631–636. ISSN: 0092-7023 (Mar. 1947).
7. Li, Q., Jonas, U., Zhao, X. S. & Kappl, M. The forces at work in colloidal self-assembly: a review on fundamental interactions between colloidal particles. de. *Asia-Pacific Journal of Chemical Engineering* **3,** 255–268. ISSN: 1932-2143 (2008).
8. Lekkerkerker, H. N. & Tuinier, R. *Colloids and the Depletion Interaction* en. ISBN: 978-94-007-1222-5 (Springer Netherlands, Dordrecht, 2011).
9. Burger, S. & Bartsch, E. Influence of the polymer size on depletion attraction–induced gel and glass transitions of microgel colloids. en. *Colloids and Surfaces A: Physicochemical and Engineering Aspects. Selected papers from the 26th European Colloid and Interface Society conference (26th ECIS 2012)* **442,** 6–15. ISSN: 0927-7757 (Feb. 2014).
10. Hunter, R. J., White, L. R. & Chan, D. Y. C. *Foundations of Colloid Science* en. ISBN: 978-0-19-855188-1 (Clarendon Press, 1987).
11. Lyklema, J. *Fundamentals of Interface and Colloid Science: Particulate Colloids* en. ISBN: 978-0-08-045439-9 (Elsevier, Mar. 2005).
12. Lyklema, J. *Fundamentals of Interface and Colloid Science: Soft Colloids* en. ISBN: 978-0-08-045740-6 (Elsevier, Mar. 2005).
13. Lyklema, J. *Fundamentals of Interface and Colloid Science: Fundamentals* en. ISBN: 978-0-12-460525-1 (Elsevier Science, Feb. 1991).
14. Coey, J. M. D. *Magnetism and Magnetic Materials* ISBN: 978-0-521-81614-4 (Cambridge University Press, Cambridge, 2010).

15. Durán, J. D. G., Arias, J. L., Gallardo, V. & Delgado, A. V. Magnetic colloids as drug vehicles. eng. *Journal of Pharmaceutical Sciences* **97,** 2948–2983. ISSN: 1520-6017 (Aug. 2008).

16. Feldmann, M. & Buttgenbach, S. Novel Microrobots and Micromotors Using Lorentz Force Driven Linear Microactuators Based on Polymer Magnets. *IEEE Transactions on Magnetics* **43,** 3891–3895. ISSN: 1941-0069 (Oct. 2007).

17. Thananukul, K., Kaewsaneha, C., Opaprakasit, P., Lebaz, N., Errachid, A. & Elaissari, A. Smart gating porous particles as new carriers for drug delivery. en. *Advanced Drug Delivery Reviews* **174,** 425–446. ISSN: 0169-409X (July 2021).

18. Qin, S., Yin, H., Yang, C., Dou, Y., Liu, Z., Zhang, P., Yu, H., Huang, Y., Feng, J., Hao, J., Hao, J., Deng, L., Yan, X., Dong, X., Zhao, Z., Jiang, T., Wang, H.-W., Luo, S.-J. & Xie, C. A magnetic protein biocompass. en. *Nature Materials* **15,** 217–226. ISSN: 1476-4660 (Feb. 2016).

19. Langmuir, I. The Arrangement of Electrons in Atoms and Molecules. *Journal of the American Chemical Society* **41,** 868–934. ISSN: 0002-7863 (June 1919).

20. Morrish, A. H. *Canted Antiferromagnetism: Hematite* ISBN: 978-981-02-2007-5 (World Scientific, Jan. 1995).

21. Stein, C. R., Bezerra, M. T. S., Holanda, G. H. A., André-Filho, J. & Morais, P. C. Structural and magnetic properties of cobalt ferrite nanoparticles synthesized by co-precipitation at increasing temperatures. *AIP Advances* **8,** 056303 (May 2018).

22. Karaagac, O., Yildiz, B. B. & Köçkar, H. The influence of synthesis parameters on one-step synthesized superparamagnetic cobalt ferrite nanoparticles with high saturation magnetization. en. *Journal of Magnetism and Magnetic Materials* **473,** 262–267. ISSN: 0304-8853 (Mar. 2019).

23. Dunlop, D. J. Superparamagnetic and single-domain threshold sizes in magnetite. en. *Journal of Geophysical Research (1896-1977)* **78,** 1780–1793. ISSN: 2156-2202 (1973).

24. Rossi, L., Donaldson, J. G., Meijer, J.-M., Petukhov, A. V., Kleckner, D., Kantorovich, S. S., Irvine, W. T. M., Philipse, A. P. & Sacanna, S. Self-organization in dipolar cube fluids constrained by competing anisotropies. en. *Soft Matter* **14,** 1080–1087. ISSN: 1744-6848 (Feb. 2018).

25. Boles, M. A., Engel, M. & Talapin, D. V. Self-Assembly of Colloidal Nanocrystals: From Intricate Structures to Functional Materials. *Chemical Reviews* **116,** 11220–11289. ISSN: 0009-2665 (Sept. 2016).

26. Deng, K., Luo, Z., Tan, L. & Quan, Z. Self-assembly of anisotropic nanoparticles into functional superstructures. en. *Chemical Society Reviews* **49,** 6002–6038 (2020).

27. Li, F., Josephson, D. P. & Stein, A. Colloidal Assembly: The Road from Particles to Colloidal Molecules and Crystals. en. *Angewandte Chemie International Edition* **50,** 360–388. ISSN: 1521-3773 (2011).

28. Li, Z., Fan, Q. & Yin, Y. Colloidal Self-Assembly Approaches to Smart Nanostructured Materials. *Chemical Reviews* **122,** 4976–5067. ISSN: 0009-2665 (Mar. 2022).

29. Waterhouse, G. I. N. & Waterland, M. R. Opal and inverse opal photonic crystals: Fabrication and characterization. en. *Polyhedron. Modern Inorganic Chemistry in Australia and New Zealand* **26,** 356–368. ISSN: 0277-5387 (Jan. 2007).

30. Teich, E. G., Van Anders, G., Klotsa, D., Dshemuchadse, J. & Glotzer, S. C. Clusters of polyhedra in spherical confinement. *Proceedings of the National Academy of Sciences of the United States of America* **113,** E669–E678. ISSN: 10916490 (Feb. 2016).

31. Damasceno, P. F., Engel, M. & Glotzer, S. C. Predictive Self-Assembly of Polyhedra into Complex Structures. *Science* **337,** 453–457. ISSN: 0036-8075 (2012).

32. Wang, D., Hermes, M., Kotni, R., Wu, Y., Tasios, N., Liu, Y., De Nijs, B., Van Der Wee, E. B., Murray, C. B., Dijkstra, M. & Van Blaaderen, A. Interplay between spherical confinement and particle shape on the self-assembly of rounded cubes. *Nature Communications* **9,** 1–10. ISSN: 20411723 (Dec. 2018).

33. Agthe, M., Plivelic, T. S., Labrador, A., Bergström, L. & Salazar-Alvarez, G. Following in Real Time the Two-Step Assembly of Nanoparticles into Mesocrystals in Levitating Drops. *Nano Letters* **16,** 6838–6843. ISSN: 1530-6984 (Nov. 2016).

34. Tang, Y., Gomez, L., Lesage, A., Marino, E., Kodger, T. E., Meijer, J.-M., Kolpakov, P., Meng, J., Zheng, K., Gregorkiewicz, T. & Schall, P. Highly Stable Perovskite Supercrystals via Oil-in-Oil Templating. *Nano Letters* **20,** 5997–6004 (2020).

35. Debata, S., Alam Kherani, N., Kumar Panda, S. & Pratap Singh, D. Light-driven microrobots: capture and transport of bacteria and microparticles in a fluid medium. en. *Journal of Materials Chemistry B* **10,** 8235–8243 (2022).

36. Sajjadi, S. H. & Goharshadi, E. K. Highly monodispersed hematite cubes for removal of ionic dyes. en. *Journal of Environmental Chemical Engineering* **5,** 1096–1106. ISSN: 2213-3437 (Feb. 2017).

37. Alp, E., İmamoğlu, R., Savacı, U., Turan, S., Kazmanlı, M. K. & Genç, A. Plasmon-enhanced photocatalytic and antibacterial activity of gold nanoparticles-decorated hematite nanostructures. en. *Journal of Alloys and Compounds* **852,** 157021. ISSN: 0925-8388 (Jan. 2021).

38. Yuan, M., Gong, M., Huang, H., Zhao, Y., Ying, Y. & Wang, S. Bubble-Propelled Plasmon-Reinforced Pt-ZnIn 2 S 4 Micromotors for Stirring-Free Photocatalytic Water Purification. en. *Inorganic Chemistry Frontiers* (2022).

39. Wu, J., Folio, D., Zhu, J., Jang, B., Chen, X., Feng, J., Gambardella, P., Sort, J., Puigmartí-Luis, J., Ergeneman, O., Ferreira, A. & Pané, S. Motion Analysis and Real-Time Trajectory Prediction of Magnetically Steerable Catalytic Janus Micromotors. en. *Advanced Intelligent Systems* **n/a,** 2200192. ISSN: 2640-4567.

40. Zhang, Z., Boxall, C. & Kelsall, G. H. en. in *Colloids in the Aquatic Environment* (eds Tadros, T. F. & Gregory, J.) 145–163 (Elsevier, Oxford, Jan. 1993). ISBN: 978-1-85861-038-2.

41. Heckel, S., Hübner, J., Leutzgen, A., Jung, G. & Simmchen, J. Progress Report on pH-Influenced Photocatalysis for Active Motion. en. *Catalysts* **11,** 599. ISSN: 2073-4344 (May 2021).

42. Lei, T., Zhao, C., Yan, R. & Zhao, N. Collective behavior of chiral active particles with anisotropic interactions in a confined space. en. *Soft Matter* **19,** 1312–1329 (2023).

43. Schyck, S., Meijer, J.-M., Baldauf, L., Schall, P., Petukhov, A. V. & Rossi, L. Self-assembly of colloidal superballs under spherical confinement of a drying droplet. en. *JCIS Open* **5,** 100037. ISSN: 2666-934X (Apr. 2022).

44. Schyck, S., Meijer, J.-M., Baldauf, L., Schall, P., Petukhov, A. V. & Rossi, L. *Data for: Self-assembly of colloidal superballs under spherical confinement of a drying droplet* 2022.

45. Manoharan, V. N. Colloidal matter: Packing, geometry, and entropy. *Science* **349.** ISSN: 0036-8075 (2015).

46. Zhao, T. H., Jacucci, G., Chen, X., Song, D.-P., Vignolini, S. & Parker, R. M. Angular-Independent Photonic Pigments via the Controlled Micellization of Amphiphilic Bottlebrush Block Copolymers. *Advanced Materials* **32,** 2002681 (2020).

47. Vogel, N., Retsch, M., Fustin, C.-A., del Campo, A. & Jonas, U. Advances in Colloidal Assembly: The Design of Structure and Hierarchy in Two and Three Dimensions. *Chemical Reviews* **115,** 6265–6311 (2015).

48. Marín, Á. G., Gelderblom, H., Susarrey-Arce, A., van Houselt, A., Lefferts, L., Gardeniers, J. G. E., Lohse, D. & Snoeijer, J. H. Building microscopic soccer balls with evaporating colloidal fakir drops. *Proceedings of the National Academy of Sciences* **109,** 16455–16458. ISSN: 0027-8424 (2012).

49. Wang, T., LaMontagne, D., Lynch, J., Zhuang, J. & Cao, Y. C. Colloidal superparticles from nanoparticle assembly. *Chem. Soc. Rev.* **42,** 2804–2823 (2013).

50. Vogel, N., Utech, S., England, G. T., Shirman, T., Phillips, K. R., Koay, N., Burgess, I. B., Kolle, M., Weitz, D. A. & Aizenberg, J. Color from hierarchy: Diverse optical properties of micron-sized spherical colloidal assemblies. *Proceedings of the National Academy of Sciences* **112,** 10845–10850 (Sept. 2015).

51. Wintzheimer, S., Granath, T., Oppmann, M., Kister, T., Thai, T., Kraus, T., Vogel, N. & Mandel, K. Supraparticles: Functionality from Uniform Structural Motifs. *ACS Nano* **12,** 5093–5120 (2018).

52. Rastogi, V., Melle, S., Calderón, O. G., García, A. A., Marquez, M. & Velev, O. D. Synthesis of Light-Diffracting Assemblies from Microspheres and Nanoparticles in Droplets on a Superhydrophobic Surface. *Advanced Materials* **20,** 4263–4268. ISSN: 1521-4095 (2008).

53. Rastogi, V., García, A. A., Marquez, M. & Velev, O. D. Anisotropic Particle Synthesis Inside Droplet Templates on Superhydrophobic Surfaces. en. *Macromolecular Rapid Communications* **31,** 190–195. ISSN: 1521-3927 (2010).

54. De Nijs, B., Dussi, S., Smallenburg, F., Meeldijk, J. D., Groenendijk, D. J., Filion, L., Imhof, A., van Blaaderen, A. & Dijkstra, M. Entropy-driven formation of large icosahedral colloidal clusters by spherical confinement. en. *Nature Materials* **14,** 56–60. ISSN: 1476-4660 (Jan. 2015).

55. Wang, D., Dasgupta, T., van der Wee, E. B., Zanaga, D., Altantzis, T., Wu, Y., Coli, G. M., Murray, C. B., Bals, S., Dijkstra, M. & van Blaaderen, A. Binary icosahedral clusters of hard spheres in spherical confinement. en. *Nature Physics* **17,** 128–134. ISSN: 1745-2481 (Jan. 2021).

56. Wang, J., Mbah, C. F., Przybilla, T., Apeleo Zubiri, B., Spiecker, E., Engel, M. & Vogel, N. Magic number colloidal clusters as minimum free energy structures. en. *Nature Communications* **9,** 5259. ISSN: 2041-1723 (Dec. 2018).

57. Pauchard, L. & Couder, Y. Invagination during the collapse of an inhomogeneous spheroidal shell. en. *Europhysics Letters* **66,** 667. ISSN: 0295-5075 (June 2004).

58. Hueckel, T., Hocky, G. M. & Sacanna, S. Total synthesis of colloidal matter. *Nature Reviews Materials*. ISSN: 2058-8437 (2021).

59. Van Damme, R., Coli, G. M., van Roij, R. & Dijkstra, M. Classifying Crystals of Rounded Tetrahedra and Determining Their Order Parameters Using Dimensionality Reduction. *ACS Nano* **14,** 15144–15153. ISSN: 1936-0851 (Nov. 2020).

60. Yuan, Y., Liu, L., Deng, W. & Li, S. Random-packing properties of spheropolyhedra. *Powder Technology* **351,** 186–194. ISSN: 00325910 (June 2019).

61. Jacucci, G., Longbottom, B. W., Parkins, C. C., Bon, S. A. F. & Vignolini, S. Anisotropic silica colloids for light scattering. *J. Mater. Chem. C* **9,** 2695–2700 (2021).

62. Jiao, Y., Stillinger, F. H. & Torquato, S. Optimal packings of superballs. *Physical Review E* **79,** 041309 (Apr. 2009).

63. Batten, R. D., Stillinger, F. H. & Torquato, S. Phase behavior of colloidal superballs: Shape interpolation from spheres to cubes. *Physical Review E* **81,** 061105 (June 2010).

64. Ni, R., Gantapara, A. P., Graaf, J. d., Roij, R. v. & Dijkstra, M. Phase diagram of colloidal hard superballs: from cubes via spheres to octahedra. en. *Soft Matter* **8,** 8826–8834. ISSN: 1744-6848 (Aug. 2012).

65. Zhang, Y., Lu, F., van der Lelie, D. & Gang, O. Continuous Phase Transformation in Nanocube Assemblies. *Physical Review Letters* **107,** 135701 (Sept. 2011).

66. Brunner, J., Baburin, I. A., Sturm, S., Kvashnina, K., Rossberg, A., Pietsch, T., Andreev, S., Sturm (née Rosseeva), E. & Cölfen, H. Self-Assembled Magnetite Mesocrystalline Films: Toward Structural Evolution from 2D to 3D Superlattices. en. *Advanced Materials Interfaces* **4,** 1600431. ISSN: 2196-7350 (2017).

67. Rossi, L., Sacanna, S., Irvine, W. T. M., Chaikin, P. M., Pine, D. J. & Philipse, A. P. Cubic crystals from cubic colloids. en. *Soft Matter* **7,** 4139–4142. ISSN: 1744-6848 (Apr. 2011).

68. Meijer, J.-M., Pal, A., Ouhajji, S., Lekkerkerker, H. N. W., Philipse, A. P. & Petukhov, A. V. Observation of solid–solid transitions in 3D crystals of colloidal superballs. en. *Nature Communications* **8,** 14352. ISSN: 2041-1723 (Feb. 2017).

69. Rossi, L., Soni, V., Ashton, D. J., Pine, D. J., Philipse, A. P., Chaikin, P. M., Dijkstra, M., Sacanna, S. & Irvine, W. T. M. Shape-sensitive crystallization in colloidal superball fluids. *Proceedings of the National Academy of Sciences* **112,** 5286–5290 (Apr. 2015).

70. Meijer, J.-M., Meester, V., Hagemans, F., Lekkerkerker, H., Philipse, A. P. & Petukhov, A. V. Convectively Assembled Monolayers of Colloidal Cubes: Evidence of Optimal Packings. *Langmuir* **35,** 4946–4955 (2019).

71. Meijer, J.-M., Hagemans, F., Rossi, L., Byelov, D. V., Castillo, S. I., Snigirev, A., Snigireva, I., Philipse, A. P. & Petukhov, A. V. Self-Assembly of Colloidal Cubes via Vertical Deposition. *Langmuir* **28,** 7631–7638. ISSN: 0743-7463 (May 2012).

72. Sen, D., Bahadur, J., Mazumder, S., Santoro, G., Yu, S. & V. Roth, S. Probing evaporation induced assembly across a drying colloidal droplet using in situ small-angle X-ray scattering at the synchrotron source. en. *Soft Matter* **10,** 1621–1627 (2014).

73. Marino, E., Kodger, T. E., Wegdam, G. H. & Schall, P. Revealing Driving Forces in Quantum Dot Supercrystal Assembly. *Advanced Materials* **30,** 1803433. ISSN: 09359648 (Oct. 2018).

74. Montanarella, F., Geuchies, J. J., Dasgupta, T., Prins, P. T., van Overbeek, C., Dattani, R., Baesjou, P., Dijkstra, M., Petukhov, A. V., van Blaaderen, A. & Vanmaekelbergh, D. Crystallization of Nanocrystals in Spherical Confinement Probed by in Situ X-ray Scattering. *Nano Letters* **18,** 3675–3681. ISSN: 1530-6984 (June 2018).

75. Sugimoto, T. & Sakata, K. Preparation of monodisperse pseudocubic α-Fe2O3 particles from condensed ferric hydroxide gel. en. *Journal of Colloid and Interface Science* **152,** 587–590. ISSN: 0021-9797 (Sept. 1992).

76. Graf, C., Vossen, D. L. J., Imhof, A. & van Blaaderen, A. A General Method To Coat Colloidal Particles with Silica. *Langmuir* **19,** 6693–6700. ISSN: 0743-7463 (Aug. 2003).

77. Stöber, W., Fink, A. & Bohn, E. Controlled growth of monodisperse silica spheres in the micron size range. *Journal of Colloid and Interface Science* **26,** 62–69. ISSN: 00219797 (Jan. 1968).

78. Chen, S. .-. Preparation of monosize silica spheres and their crystalline stack. en. *Colloids and Surfaces A: Physicochemical and Engineering Aspects* **142,** 59–63. ISSN: 0927-7757 (Nov. 1998).

79. Deng, X., Mammen, L., Butt, H.-J. & Vollmer, D. Candle Soot as a Template for a Transparent Robust Superamphiphobic Coating. *Science* **335,** 67–70 (Jan. 2012).

80. Bras, W., Dolbnya, I., Detollenaere, D., Van Tol, R., Malfois, M., Greaves, G., Ryan, A. & Heeley, E. Recent experiments on a small-angle/wide-angle X-ray scattering beam line at the ESRF. en. *Journal of Applied Crystallography* **36,** 791–794. ISSN: 1600-5767 (2003).

81. Petukhov, A. V., Meijer, J.-M. & Vroege, G. J. Particle shape effects in colloidal crystals and colloidal liquid crystals: Small-angle X-ray scattering studies with microradian resolution. en. *Current Opinion in Colloid & Interface Science* **20,** 272–281. ISSN: 1359-0294 (Aug. 2015).

82. Snigirev, A., Kohn, V., Snigireva, I. & Lengeler, B. A compound refractive lens for focusing high-energy X-rays. en. *Nature* **384,** 49–51. ISSN: 1476-4687 (Nov. 1996).

83. Elkies, N. D., Odlyzko, A. M. & Rush, J. A. On the packing densities of superballs and other bodies. en. *Inventiones mathematicae* **105,** 613–639. ISSN: 1432-1297 (Dec. 1991).

84. Dekker, F., Kuipers, B. W. M., González García, Á., Tuinier, R. & Philipse, A. P. Scattering from colloidal cubic silica shells: Part II, static structure factors and osmotic equation of state. en. *Journal of Colloid and Interface Science* **571,** 267–274. ISSN: 0021-9797 (July 2020).

85. Pedersen, J. S. Analysis of small-angle scattering data from colloids and polymer solutions: modeling and least-squares fitting. en. *Advances in Colloid and Interface Science* **70,** 171–210. ISSN: 0001-8686 (July 1997).

86. Rieker, T., Hanprasopwattana, A., Datye, A. & Hubbard, P. Particle Size Distribution Inferred from Small-Angle X-ray Scattering and Transmission Electron Microscopy (1999).

87. Meijer, J.-M., Byelov, D. V., Rossi, L., Snigirev, A., Snigireva, I., Philipse, A. P. & Petukhov, A. V. Self-assembly of colloidal hematite cubes: a microradian X-ray diffraction exploration of sedimentary crystals. en. *Soft Matter* **9,** 10729–10738. ISSN: 1744-6848 (Oct. 2013).

88. Olivero, J. J. & Longbothum, R. L. Empirical fits to the Voigt line width: A brief review. en. *Journal of Quantitative Spectroscopy and Radiative Transfer* **17,** 233–236. ISSN: 0022-4073 (Feb. 1977).

89. Patterson, A. L. The scherrer formula for X-ray particle size determination. *Physical Review* **56,** 978–982. ISSN: 0031899X (1939).

90. Petukhov, A. V., Dolbnya, I. P., Aarts, D. G. A. L., Vroege, G. J. & Lekkerkerker, H. N. W. Bragg Rods and Multiple X-Ray Scattering in Random-Stacking Colloidal Crystals. *Physical Review Letters* **90,** 4. ISSN: 10797114 (Jan. 2003).

91. Förster, S., Timmann, A., Schellbach, C., Frömsdorf, A., Kornowski, A., Weller, H., Roth, S. V. & Lindner, P. Order causes secondary Bragg peaks in soft materials. *Nature Materials* **6,** 888–893. ISSN: 14764660 (Aug. 2007).

92. Kralchevsky, P. A. & Nagayama, K. Capillary forces between colloidal particles. en. *Langmuir* **10,** 23–36. ISSN: 0743-7463, 1520-5827 (Jan. 1994).

93. Wang, J., Kang, E., Sultan, U., Merle, B., Inayat, A., Graczykowski, B., Fytas, G. & Vogel, N. Influence of Surfactant-Mediated Interparticle Contacts on the Mechanical Stability of Supraparticles. *The Journal of Physical Chemistry C* **125,** 23445–23456. ISSN: 1932-7447 (Oct. 2021).

94. Schyck, S., Meijer, J.-M., Schelling, M. P. M., Petukhov, A. V. & Rossi, L. *Data for Droplet-based Assembly of Magnetic Superballs* en. June 2023.

95. Bigdeli, M. B. & Tsai, P. A. Making Photonic Crystals via Evaporation of Nanoparticle-Laden Droplets on Superhydrophobic Microstructures. *Langmuir* **36,** 4835–4841. ISSN: 0743-7463 (May 2020).

96. Quan, Z. & Fang, J. Superlattices with non-spherical building blocks. en. *Nano Today* **5,** 390–411. ISSN: 1748-0132 (Jan. 2010).

97. Glotzer, S. C. & Solomon, M. J. Anisotropy of building blocks and their assembly into complex structures. en. *Nature Materials* **6,** 557–562. ISSN: 1476-4660 (Aug. 2007).

98. Lee, Y. H., Lay, C. L., Shi, W., Lee, H. K., Yang, Y., Li, S. & Ling, X. Y. Creating two self-assembly micro-environments to achieve supercrystals with dual structures using polyhedral nanoparticles. en. *Nature Communications* **9,** 2769. ISSN: 2041-1723 (July 2018).

99. Ahniyaz, A., Sakamoto, Y. & Bergström, L. Magnetic field-induced assembly of oriented superlattices from maghemite nanocubes. *Proceedings of the National Academy of Sciences* **104,** 17570–17574 (Nov. 2007).

100. Yadav, A. & Tirumkudulu, M. S. Free-standing monolayer films of ordered colloidal particles. en. *Soft Matter* **13,** 4520–4525. ISSN: 1744-6848 (June 2017).

101. Yu, Y., Yang, X., Liu, M., Nishikawa, M., Tei, T. & Miyako, E. Amphipathic Nanodiamond Supraparticles for Anticancer Drug Loading and Delivery. *ACS Applied Materials & Interfaces* **11,** 18978–18987. ISSN: 1944-8244 (May 2019).

102. Liu, J., Xiao, M., Li, C., Li, H., Wu, Z., Zhu, Q., Tang, R., Bo Xu, A. & He, L. Rugby-ball-like photonic crystal supraparticles with non-close-packed structures and multiple magneto-optical responses. en. *Journal of Materials Chemistry C* **7,** 15042–15048 (2019).

103. Kapuscinski, M., Agthe, M., Lv, Z.-P., Liu, Y., Segad, M. & Bergström, L. Temporal Evolution of Superlattice Contraction and Defect-Induced Strain Anisotropy in Mesocrystals during Nanocube Self-Assembly. *ACS Nano* **14,** 5337–5347. ISSN: 1936-0851 (May 2020).

104. Kim, J., Hwang, H., Butt, H.-J. & Wooh, S. Designing the shape of supraparticles by controlling the apparent contact angle and contact line friction of droplets. en. *Journal of Colloid and Interface Science* **588,** 157–163. ISSN: 0021-9797 (Apr. 2021).

105. Tirumkudulu, M. S. Buckling of a drying colloidal drop. en. *Soft Matter* **14,** 7455–7461. ISSN: 1744-6848 (Sept. 2018).

106. Seyfert, C., Berenschot, E. J. W., Tas, N. R., Susarrey-Arce, A. & Marin, A. Evaporation-driven colloidal cluster assembly using droplets on superhydrophobic fractal-like structures. en. *Soft Matter* **17,** 506–515. ISSN: 1744-6848 (Jan. 2021).

107. Lv, Z.-P., Kapuscinski, M. & Bergström, L. Tunable assembly of truncated nanocubes by evaporation-driven poor-solvent enrichment. en. *Nature Communications* **10,** 4228. ISSN: 2041-1723 (Sept. 2019).

108. Meijer, J. M. & Rossi, L. Preparation, properties, and applications of magnetic hematite microparticles. en. *Soft Matter* **17,** 2354–2368. ISSN: 1744-6848 (Mar. 2021).

109. Donaldson, J. G., Schall, P. & Rossi, L. Magnetic Coupling in Colloidal Clusters for Hierarchical Self-Assembly. *ACS Nano* **15,** 4989–4999. ISSN: 1936-0851 (Mar. 2021).

110. Baldauf, L., Teich, E. G., Schall, P., van Anders, G. & Rossi, L. Shape and interaction decoupling for colloidal preassembly. *Science Advances* **8,** eabm0548 (May 2022).

111. Disch, S., Wetterskog, E., Hermann, R. P., Salazar-Alvarez, G., Busch, P., Brückel, T., Bergström, L. & Kamali, S. Shape Induced Symmetry in Self-Assembled Mesocrystals of Iron Oxide Nanocubes. *Nano Letters* **11,** 1651–1656. ISSN: 1530-6984 (Apr. 2011).

112. Disch, S., Wetterskog, E., Hermann, R. P., Korolkov, D., Busch, P., Boesecke, P., Lyon, O., Vainio, U., Salazar-Alvarez, G., Bergström, L. & Brückel, T. Structural diversity in iron oxide nanoparticle assemblies as directed by particle morphology and orientation. *Nanoscale* **5,** 3969–3975. ISSN: 20403364 (May 2013).

113. Schulz, F., Lokteva, I., Parak, W. J. & Lehmkühler, F. Recent Notable Approaches to Study Self-Assembly of Nanoparticles with X-Ray Scattering and Electron Microscopy. en. *Particle & Particle Systems Characterization* **38,** 2100087. ISSN: 1521-4117 (2021).

114. PETOUKHOV, A., ROSSI, L. & SCHYCK, S. *Unraveling the peculiar internal structure of hematite microparticles* en. 2025.

115. MEDJAHED, A. A., PETOUKHOV, A., ROSSI, L., BURGHAMMER, M. & SCHYCK, S. *Follow up on unraveling the peculiar internal structure of hematite microparticles* en. 2025.

116. Wittmann, M., Ali, A., Gemming, T., Stavale, F. & Simmchen, J. Semiconductor-Based Microswimmers: Attention to Detail Matters. *The Journal of Physical Chemistry Letters* **12,** 9651–9656 (Oct. 2021).

117. Zhao, G., Ambrosi, A. & Pumera, M. Self-propelled nanojets via template electrodeposition. en. *Nanoscale* **5,** 1319–1324. ISSN: 2040-3372 (Feb. 2013).

118. Sridhar, V., Park, B.-W. & Sitti, M. Light-Driven Janus Hollow Mesoporous TiO2–Au Microswimmers. en. *Advanced Functional Materials* **28,** 1704902. ISSN: 1616-3028 (2018).

119. Palacci, J., Sacanna, S., Kim, S.-H., Yi, G.-R., Pine, D. J. & Chaikin, P. M. Light-activated self-propelled colloids. *Philosophical transactions. Series A, Mathematical, physical, and engineering sciences* **372,** 20130372. ISSN: 1364-503X (Nov. 2014).

120. Palacci, J., Sacanna, S., Vatchinsky, A., Chaikin, P. M. & Pine, D. J. Photoactivated Colloidal Dockers for Cargo Transportation. *Journal of the American Chemical Society* **135,** 15978–15981. ISSN: 0002-7863 (Oct. 2013).

121. Massana-Cid, H., Codina, J., Pagonabarraga, I. & Tierno, P. Active apolar doping determines routes to colloidal clusters and gels. eng. *Proceedings of the National Academy of Sciences of the United States of America* **115,** 10618–10623. ISSN: 1091-6490 (Oct. 2018).

122. Aubret, A., Martinet, Q. & Palacci, J. Metamachines of pluripotent colloids. en. *Nature Communications* **12,** 6398. ISSN: 2041-1723 (Nov. 2021).

123. Tamirat, A. G., Rick, J., Dubale, A. A., Su, W.-N. & Hwang, B.-J. Using hematite for photoelectrochemical water splitting: a review of current progress and challenges. en. *Nanoscale Horizons* **1,** 243–267. ISSN: 2055-6764 (June 2016).

124. Kormann, C., Bahnemann, D. W. & Hoffmann, M. R. Environmental photochemistry: Is iron oxide (hematite) an active photocatalyst? A comparative study: α-Fe2O3, ZnO, TiO2. en. *Journal of Photochemistry and Photobiology A: Chemistry* **48,** 161–169. ISSN: 1010-6030 (July 1989).

125. Cendula, P., Steier, L., Losio, P. A., Grätzel, M. & Schumacher, J. O. Analysis of Optical Losses in a Photoelectrochemical Cell: A Tool for Precise Absorptance Estimation. en. *Advanced Functional Materials* **28,** 1702768. ISSN: 1616-3028 (2018).

126. Phromma, S., Wutikhun, T., Kasamechonchung, P., Eksangsri, T. & Sapcharoenkun, C. Effect of Calcination Temperature on Photocatalytic Activity of Synthesized TiO2 Nanoparticles via Wet Ball Milling Sol-Gel Method. en. *Applied Sciences* **10,** 993. ISSN: 2076-3417 (Jan. 2020).

127. Tsubota, S., Nakamura, T., Tanaka, K. & Haruta, M. Effect of calcination temperature on the catalytic activity of Au colloids mechanically mixed with TiO2 powder for CO oxidation. en. *Catalysis Letters* **56,** 131–135. ISSN: 1572-879X (Dec. 1998).

128. Bharathi, S., Nataraj, D., Mangalaraj, D., Masuda, Y., Senthil, K. & Yong, K. Highly mesoporous α-Fe2O3 nanostructures: preparation, characterization and improved photocatalytic performance towards Rhodamine B (RhB). en. *Journal of Physics D: Applied Physics* **43,** 015501. ISSN: 0022-3727 (Dec. 2009).

129. Cui, X., Liu, T., Zhang, Z., Wang, L., Zuo, S. & Zhu, W. Hematite nanorods with tunable porous structure: Facile hydrothermal-calcination route synthesis, optical and photocatalytic properties. en. *Powder Technology* **266,** 113–119. ISSN: 0032-5910 (Nov. 2014).

130. Ding, J., Zhong, Q. & Zhang, S. Catalytic efficiency of iron oxides in decomposition of H2O2 for simultaneous NOX and SO2 removal: Effect of calcination temperature. en. *Journal of Molecular Catalysis A: Chemical* **393,** 222–231. ISSN: 1381-1169 (Nov. 2014).

131. Mimouni, I., Bouziani, A., Naciri, Y., Boujnah, M., El Belghiti, M. A. & El Azzouzi, M. Effect of heat treatment on the photocatalytic activity of α-Fe2O3 nanoparticles: towards diclofenac elimination. en. *Environmental Science and Pollution Research* **29,** 7984–7996. ISSN: 1614-7499 (Jan. 2022).

132. Zeng, P., Zhao, Y., Lin, Y., Wang, X., Li, J., Wang, W. & Fang, Z. Enhancement of Electrochemical Performance by the Oxygen Vacancies in Hematite as Anode Material for Lithium-Ion Batteries. *Nanoscale Research Letters* **12,** 13. ISSN: 1556-276X (Jan. 2017).

133. Piccinin, S. The band structure and optical absorption of hematite (α-Fe2O3): a first-principles GW-BSE study. en. *Physical Chemistry Chemical Physics* **21,** 2957–2967. ISSN: 1463-9084 (Feb. 2019).

134. Duret, A. & Grätzel, M. Visible Light-Induced Water Oxidation on Mesoscopic α-Fe2O3 Films Made by Ultrasonic Spray Pyrolysis. *The Journal of Physical Chemistry B* **109,** 17184–17191. ISSN: 1520-6106 (Sept. 2005).

135. Landi, S., Segundo, I. R., Freitas, E., Vasilevskiy, M., Carneiro, J. & Tavares, C. J. Use and misuse of the Kubelka-Munk function to obtain the band gap energy from diffuse reflectance measurements. en. *Solid State Communications* **341,** 114573. ISSN: 00381098 (Jan. 2022).

136. Zevenhuizen, S. *SPIEPy: SPIEPy (Scanning Probe Image Enchanter using Python) is a Python library to improve automatic processing of SPM images.*

137. Scholder, O. *scholi/pySPM v0.2.20* Apr. 2019.

138. Kieffer, J., Valls, V., Blanc, N. & Hennig, C. New tools for calibrating diffraction setups. en. *Journal of Synchrotron Radiation* **27,** 558–566. ISSN: 1600-5775 (2020).

139. Kieffer, J., Valls, V., deschila, VINCENT, T., picca, payno, Wright, J., Huder, L., Pandolfi, R., Ashiotis, G., dodogerstlin, Faure, B., Wright, C. J. '., Weninger, C., gbenecke, jbhopkins, Hov, A., Prestat, E., Flucke, G., jangarrevoet, Märdian, L., mstorm, Hans, P., SigmundNeher, Caswell, T. A., woutdenolf & Plaswig, F. *silx-kit/pyFAI: PyFAI v0.21.3* Mar. 2022.

140. Allan, D. B., Caswell, T., Keim, N. C., van der Wel, C. M. & Verweij, R. W. *soft-matter/trackpy: Trackpy v0.5.0* Apr. 2021.

141. Palacci, J., Sacanna, S., Steinberg, A. P., Pine, D. J. & Chaikin, P. M. Living Crystals of Light-Activated Colloidal Surfers. *Science* **339,** 936–940 (Feb. 2013).

142. Audus, D. J., Hassan, A. M., Garboczi, E. J. & Douglas, J. F. Interplay of particle shape and suspension properties: a study of cube-like particles. en. *Soft Matter* **11,** 3360–3366. ISSN: 1744-6848 (Apr. 2015).

143. Royer, J. R., Burton, G. L., Blair, D. L. & Hudson, S. D. Rheology and dynamics of colloidal superballs. en. *Soft Matter* **11,** 5656–5665. ISSN: 1744-6848 (July 2015).

144. Howse, J. R., Jones, R. A. L., Ryan, A. J., Gough, T., Vafabakhsh, R. & Golestanian, R. Self-Motile Colloidal Particles: From Directed Propulsion to Random Walk. en. *Physical Review Letters* **99,** 048102. ISSN: 0031-9007, 1079-7114 (July 2007).

145. Bechinger, C., Di Leonardo, R., Löwen, H., Reichhardt, C., Volpe, G. & Volpe, G. Active Particles in Complex and Crowded Environments. en. *Reviews of Modern Physics* **88,** 045006. ISSN: 0034-6861, 1539-0756 (Nov. 2016).

146. Kaiser, M. & Kantorovich, S. S. The importance of being a cube: Active cubes in a microchannel. en. *Journal of Molecular Liquids* **360,** 119318. ISSN: 0167-7322 (Aug. 2022).

147. Bouziani, A., Park, J. & Ozturk, A. Synthesis of α-Fe2O3/TiO2 heterogeneous composites by the sol-gel process and their photocatalytic activity. en. *Journal of Photochemistry and Photobiology A: Chemistry* **400,** 112718. ISSN: 1010-6030 (Sept. 2020).

148. Sayed, F. N. & Polshettiwar, V. Facile and Sustainable Synthesis of Shaped Iron Oxide Nanoparticles: Effect of Iron Precursor Salts on the Shapes of Iron Oxides. en. *Scientific Reports* **5,** 9733. ISSN: 2045-2322 (May 2015).

149. Ulfa, M., Prasetyoko, D., Bahruji, H. & Nugraha, R. E. Green Synthesis of Hexagonal Hematite (α-Fe2O3) Flakes Using Pluronic F127-Gelatin Template for Adsorption and Photodegradation of Ibuprofen. *Materials* **14,** 6779. ISSN: 1996-1944 (Nov. 2021).

150. Momma, K. & Izumi, F. VESTA 3 for three-dimensional visualization of crystal, volumetric and morphology data. *Journal of Applied Crystallography* **44,** 1272–1276. ISSN: 00218898 (Dec. 2011).

151. Sugimoto, T., Muramatsu, A., Sakata, K. & Shindo, D. Characterization of Hematite Particles of Different Shapes. en. *Journal of Colloid and Interface Science* **158,** 420–428. ISSN: 0021-9797 (July 1993).

152. Li, Z., Sheng, J., Wang, Y. & Xu, Y. Enhanced photocatalytic activity and stability of alumina supported hematite for azo-dye degradation in aerated aqueous suspension. en. *Journal of Hazardous Materials* **254-255,** 18–25. ISSN: 0304-3894 (June 2013).

153. Wang, Y., Du, W. & Xu, Y. Effect of Sintering Temperature on the Photocatalytic Activities and Stabilities of Hematite and Silica-Dispersed Hematite Particles for Organic Degradation in Aqueous Suspensions. *Langmuir* **25,** 2895–2899. ISSN: 0743-7463 (Mar. 2009).

154. Nandiyanto, A. B. D., Zaen, R. & Oktiani, R. Correlation between crystallite size and photocatalytic performance of micrometer-sized monoclinic WO3 particles. en. *Arabian Journal of Chemistry* **13,** 1283–1296. ISSN: 1878-5352 (Jan. 2020).

155. Yassine, O., Gooneratne, C. P., Abu Smara, D., Li, F., Mohammed, H., Merzaban, J. & Kosel, J. Isolation of cells for selective treatment and analysis using a magnetic microfluidic chip. *Biomicrofluidics* **8,** 034114. ISSN: 1932-1058 (June 2014).

156. Zhang, H. & Meyerhoff, M. E. Gold-Coated Magnetic Particles for Solid-Phase Immunoassays: Enhancing Immobilized Antibody Binding Efficiency and Analytical Performance. *Analytical Chemistry* **78,** 609–616. ISSN: 0003-2700 (Jan. 2006).

157. Zhang, B., Xing, J. & Liu, H. Preparation and application of magnetic microsphere carriers. en. *Frontiers of Chemical Engineering in China* **1,** 96–101. ISSN: 1673-7474 (Feb. 2007).

158. Tempesti, P., Bonini, M., Ridi, F. & Baglioni, P. Magnetic polystyrene nanocomposites for the separation of oil and water. en. *Journal of Materials Chemistry A* **2,** 1980–1984. ISSN: 2050-7496 (Jan. 2014).

159. Baresel, C., Schaller, V., Jonasson, C., Johansson, C., Bordes, R., Chauhan, V., Sugunan, A., Sommertune, J. & Welling, S. Functionalized magnetic particles for water treatment. en. *Heliyon* **5,** e02325. ISSN: 2405-8440 (Aug. 2019).

160. Liu, Q., Wang, L., Xiao, A., Gao, J., Ding, W., Yu, H., Huo, J. & Ericson, M. Templated preparation of porous magnetic microspheres and their application in removal of cationic dyes from wastewater. en. *Journal of Hazardous Materials* **181,** 586–592. ISSN: 0304-3894 (Sept. 2010).

161. Baharvand, H. A new method for preparation of magnetic polymer particles. en. *Colloid and Polymer Science* **292,** 3311–3318. ISSN: 1435-1536 (Dec. 2014).

162. Wichaita, W., Polpanich, D., Kaewsaneha, C., Jangpatarapongsa, K. & Tangboriboonrat, P. Fabrication of functional hollow magnetic polymeric nanoparticles with controllable magnetic location. en. *Colloids and Surfaces B: Biointerfaces* **184,** 110557. ISSN: 0927-7765 (Dec. 2019).

163. Rahman, M. M., Montagne, F., Fessi, H. & Elaissari, A. Anisotropic magnetic microparticles from ferrofluid emulsion. en. *Soft Matter* **7,** 1483–1490. ISSN: 1744-6848 (Feb. 2011).

164. Braconnot, S., Eissa, M. M. & Elaissari, A. Morphology control of magnetic latex particles prepared from oil in water ferrofluid emulsion. en. *Colloid and Polymer Science* **291,** 193–203. ISSN: 1435-1536 (Jan. 2013).

165. Zhang, H., Zhang, Q., Zhang, B. & Guo, F. Preparation of magnetic composite microspheres by surfactant free controlled radical polymerization: Preparation and characteristics. en. *Journal of Magnetism and Magnetic Materials* **321,** 3921–3925. ISSN: 0304-8853 (Dec. 2009).

166. Ugelstad, J., Söderberg, L., Berge, A. & Bergström, J. Monodisperse polymer particles — a step forward for chromatography. en. *Nature* **303,** 95–96. ISSN: 1476-4687 (May 1983).

167. Ugelstad, J., Stenstad, P., Kilaas, L., Prestvik, W. S., Herje, R., Berge, A. & Hornes, E. Monodisperse Magnetic Polymer Particles. *Blood Purification* **11,** 349–369. ISSN: 0253-5068, 1421-9735 (1993).

168. Li, Y.-H., Song, T., Liu, J.-Q., Zhu, S.-J. & Chang, J. An efficient method for preparing high-performance multifunctional polymer beads simultaneously incorporated with magnetic nanoparticles and quantum dots. en. *Journal of Materials Chemistry* **21,** 12520–12528. ISSN: 1364-5501 (Aug. 2011).

169. Chung, T.-H. & Lee, W.-C. Preparation of styrene-based, magnetic polymer microspheres by a swelling and penetration process. en. *Reactive and Functional Polymers* **68,** 1441–1447. ISSN: 1381-5148 (Oct. 2008).

170. Ku, K. H., Shin, J. M., Yun, H., Yi, G.-R., Jang, S. G. & Kim, B. J. Multidimensional Design of Anisotropic Polymer Particles from Solvent-Evaporative Emulsion. en. *Advanced Functional Materials* **28,** 1802961. ISSN: 1616-3028 (2018).

171. Jeon, S.-J., Yi, G.-R. & Yang, S.-M. Cooperative Assembly of Block Copolymers with Deformable Interfaces: Toward Nanostructured Particles. *Advanced Materials* **20,** 4103–4108. ISSN: 1521-4095 (2008).

172. Liu, S., Deng, R., Li, W. & Zhu, J. Polymer Microparticles with Controllable Surface Textures Generated through Interfacial Instabilities of Emulsion Droplets. en. *Advanced Functional Materials* **22,** 1692–1697. ISSN: 1616-3028 (2012).

173. Iqbal, M., Zafar, N., Fessi, H. & Elaissari, A. Double emulsion solvent evaporation techniques used for drug encapsulation. en. *International Journal of Pharmaceutics* **496,** 173–190. ISSN: 0378-5173 (Dec. 2015).

174. Jang, S. G., Audus, D. J., Klinger, D., Krogstad, D. V., Kim, B. J., Cameron, A., Kim, S.-W., Delaney, K. T., Hur, S.-M., Killops, K. L., Fredrickson, G. H., Kramer, E. J. & Hawker, C. J. Striped, Ellipsoidal Particles by Controlled Assembly of Diblock Copolymers. *Journal of the American Chemical Society* **135,** 6649–6657. ISSN: 0002-7863 (May 2013).

175. Ku, K. H., Shin, J. M., Kim, M. P., Lee, C.-H., Seo, M.-K., Yi, G.-R., Jang, S. G. & Kim, B. J. Size-Controlled Nanoparticle-Guided Assembly of Block Copolymers for Convex Lens-Shaped Particles. *Journal of the American Chemical Society* **136,** 9982–9989. ISSN: 0002-7863 (July 2014).

176. Ku, K. H., Yang, H., Shin, J. M. & Kim, B. J. Aspect ratio effect of nanorod surfactants on the shape and internal morphology of block copolymer particles. en. *Journal of Polymer Science Part A: Polymer Chemistry* **53,** 188–192. ISSN: 1099-0518 (2015).

177. Kim, M. P., Kang, D. J., Jung, D.-W., Kannan, A. G., Kim, K.-H., Ku, K. H., Jang, S. G., Chae, W.-S., Yi, G.-R. & Kim, B. J. Gold-Decorated Block Copolymer Microspheres with Controlled Surface Nanostructures. *ACS Nano* **6,** 2750–2757. ISSN: 1936-0851 (Mar. 2012).

178. Kim, M. P., Ku, K. H., Kim, H. J., Jang, S. G., Yi, G.-R. & Kim, B. J. Surface Intaglio Nanostructures on Microspheres of Gold-Cored Block Copolymer Spheres. *Chemistry of Materials* **25,** 4416–4422. ISSN: 0897-4756 (Nov. 2013).

179. Connal, L. A., Lynd, N. A., Robb, M. J., See, K. A., Jang, S. G., Spruell, J. M. & Hawker, C. J. Mesostructured Block Copolymer Nanoparticles: Versatile Templates for Hybrid Inorganic/Organic Nanostructures. *Chemistry of Materials* **24,** 4036–4042. ISSN: 0897-4756 (Nov. 2012).

180. Tourinho, F. A., Franck, R. & Massart, R. Aqueous ferrofluids based on manganese and cobalt ferrites. en. *Journal of Materials Science* **25,** 3249–3254. ISSN: 1573-4803 (July 1990).

181. Wagner, J., Autenrieth, T. & Hempelmann, R. Core shell particles consisting of cobalt ferrite and silica as model ferrofluids [CoFe2O4–SiO2 core shell particles]. en. *Journal of Magnetism and Magnetic Materials. Proceedings of the 9th International Conference on Magnetic Fluids* **252,** 4–6. ISSN: 0304-8853 (Nov. 2002).

182. Schindelin, J., Arganda-Carreras, I., Frise, E., Kaynig, V., Longair, M., Pietzsch, T., Preibisch, S., Rueden, C., Saalfeld, S., Schmid, B., Tinevez, J.-Y., White, D. J., Hartenstein, V., Eliceiri, K., Tomancak, P. & Cardona, A. Fiji: an open-source platform for biological-image analysis. en. *Nature Methods* **9,** 676–682. ISSN: 1548-7105 (July 2012).

183. Wang, Y., Guo, B.-H., Wan, X., Xu, J., Wang, X. & Zhang, Y.-P. Janus-like polymer particles prepared via internal phase separation from emulsified polymer/oil droplets. en. *Polymer* **50,** 3361–3369. ISSN: 0032-3861 (July 2009).

184. Li, W.-I., Anderson, K. W. & Deluca, P. P. Kinetic and thermodynamic modeling of the formation of polymeric microspheres using solvent extraction/evaporation method. en. *Journal of Controlled Release* **37,** 187–198. ISSN: 0168-3659 (Dec. 1995).

185. Li, M., Rouaud, O. & Poncelet, D. Microencapsulation by solvent evaporation: State of the art for process engineering approaches. en. *International Journal of Pharmaceutics* **363,** 26–39. ISSN: 0378-5173 (Nov. 2008).

186. Saito, N., Kagari, Y. & Okubo, M. Effect of Colloidal Stabilizer on the Shape of Polystyrene/Poly(methyl methacrylate) Composite Particles Prepared in Aqueous Medium by the Solvent Evaporation Method. *Langmuir* **22,** 9397–9402. ISSN: 0743-7463 (Oct. 2006).

187. Okubo, M., Saito, N. & Fujibayashi, T. Preparation of polystyrene/poly(methyl methacrylate) composite particles having a dent. en. *Colloid and Polymer Science* **283,** 691–698. ISSN: 1435-1536 (Mar. 2005).

188. Witschi, C. & Doelker, E. Influence of the microencapsulation method and peptide loading on poly(lactic acid) and poly(lactic-co-glycolic acid) degradation during in vitro testing. en. *Journal of Controlled Release* **51,** 327–341. ISSN: 0168-3659 (Feb. 1998).

189. Lo, Y.-C., Tseng, H.-F., Chiu, Y.-J., Wu, B.-H., Li, J.-W. & Chen, J.-T. Solvent-Induced Shape Recovery of Anisotropic Polymer Particles Prepared by a Modified Thermal Stretching Method. *Langmuir* **34,** 8326–8332. ISSN: 0743-7463 (July 2018).

190. Murray, M. J. & Snowden, M. J. The preparation, characterisation and applications of colloidal microgels. en. *Advances in Colloid and Interface Science* **54,** 73–91. ISSN: 0001-8686 (Jan. 1995).

191. Nisisako, T., Torii, T., Takahashi, T. & Takizawa, Y. Synthesis of Monodisperse Bicolored Janus Particles with Electrical Anisotropy Using a Microfluidic Co-Flow System. *Advanced Materials* **18,** 1152–1156. ISSN: 1521-4095 (2006).

192. Van Berkum, S. & Erné, B. H. Demagnetization Treatment of Remanent Composite Microspheres Studied by Alternating Current Susceptibility Measurements. *International Journal of Molecular Sciences* **14,** 18093–18109. ISSN: 1422-0067 (Sept. 2013).

193. Song, H., Spencer, J., Jander, A., Nielsen, J., Stasiak, J., Kasperchik, V. & Dhagat, P. Inkjet printing of magnetic materials with aligned anisotropy. *Journal of Applied Physics* **115,** 17E308. ISSN: 0021-8979 (May 2014).

194. Gao, M., Kuang, M., Li, L., Liu, M., Wang, L. & Song, Y. Printing 1D Assembly Array of Single Particle Resolution for Magnetosensing. en. *Small* **14,** 1800117. ISSN: 1613-6829 (2018).

195. Wang, Y., Deng, R., Yang, L. & Bain, C. D. Fabrication of monolayers of uniform polymeric particles by inkjet printing of monodisperse emulsions produced by microfluidics. en. *Lab on a Chip* **19,** 3077–3085. ISSN: 1473-0189 (Sept. 2019).

196. Ansari, M. H. D., Iacovacci, V., Pane, S., Ourak, M., Borghesan, G., Tamadon, I., Vander Poorten, E. & Menciassi, A. 3D Printing of Small-Scale Soft Robots with Programmable Magnetization. en. *Advanced Functional Materials* **n/a,** 2211918. ISSN: 1616-3028.

197. Xu, T., Zhang, J., Salehizadeh, M., Onaizah, O. & Diller, E. Millimeter-scale flexible robots with programmable three-dimensional magnetization and motions. *Science Robotics* **4,** eaav4494 (2019).

198. Hu, W., Lum, G. Z., Mastrangeli, M. & Sitti, M. Small-scale soft-bodied robot with multimodal locomotion. en. *Nature* **554,** 81–85. ISSN: 1476-4687 (Feb. 2018).

199. Kim, J., Chung, S. E., Choi, S.-E., Lee, H., Kim, J. & Kwon, S. Programming magnetic anisotropy in polymeric microactuators. en. *Nature Materials* **10,** 747–752. ISSN: 1476-4660 (Oct. 2011).

200. Zhang, J., Ren, Z., Hu, W., Soon, R. H., Yasa, I. C., Liu, Z. & Sitti, M. Voxelated three-dimensional miniature magnetic soft machines via multimaterial heterogeneous assembly. *Science Robotics* **6,** eabf0112 (Apr. 2021).

201. Champion, J. A., Katare, Y. K. & Mitragotri, S. Making polymeric micro- and nanoparticles of complex shapes. *Proceedings of the National Academy of Sciences* **104,** 11901–11904 (July 2007).

202. Ho, C. C., Ottewill, R. H., Keller, A. & Odell, J. A. Monodisperse ellipsoidal polystyrene latex particles: Preparation and characterisation. en. *Polymer International* **30,** 207–211. ISSN: 1097-0126 (1993).

203. Lo, Y.-C., Chiu, Y.-J., Tseng, H.-F. & Chen, J.-T. Thermal-Annealing-Induced Self-Stretching: Fabrication of Anisotropic Polymer Particles on Polymer Films. *Langmuir* **33,** 12300–12305. ISSN: 0743-7463 (Oct. 2017).

204. Güell, O., Sagués, F. & Tierno, P. Magnetically Driven Janus Micro-Ellipsoids Realized via Asymmetric Gathering of the Magnetic Charge. *Advanced Materials* **23,** 3674–3679. ISSN: 1521-4095 (2011).

205. Gabrielson, L. & Folkes, M. J. Manufacture of colloidal polymer ellipsoids for anisotropic conducting nano-composites. en.

206. Kim, H., Bauer, J. L., Vasquez, P. A. & Furst, E. M. Structural coarsening of magnetic ellipsoid particle suspensions driven in toggled fields. en. *Journal of Physics D: Applied Physics* **52,** 184002. ISSN: 0022-3727 (Mar. 2019).

207. Peyser, P. & Bascom, W. D. Effect of filler and cooling rate on the glass transition of polymers. *Journal of Macromolecular Science, Part B* **13,** 597–610. ISSN: 0022-2348 (May 1977).

208. Guo, Z., Zhang, D., Wei, S., Wang, Z., Karki, A. B., Li, Y., Bernazzani, P., Young, D. P., Gomes, J. A., Cocke, D. L. & Ho, T. C. Effects of iron oxide nanoparticles on polyvinyl alcohol: interfacial layer and bulk nanocomposites thin film. en. *Journal of Nanoparticle Research* **12,** 2415–2426. ISSN: 1572-896X (Sept. 2010).

209. Miller, A. A. Analysis of the melt viscosity and glass transition of polystyrene. en. *Journal of Polymer Science Part A-2: Polymer Physics* **6,** 1161–1175. ISSN: 1542-9377 (1968).

210. Trisnanto, S. B., Ota, S. & Takemura, Y. Two-step relaxation process of colloidal magnetic nanoclusters under pulsed fields. en. *Applied Physics Express* **11,** 075001. ISSN: 1882-0786 (June 2018).

211. Xu, C., Huang, C., Yang, D., Luo, L. & Huang, S. Photo-Luminescent Photonic Crystals for Anti-Counterfeiting. *ACS Omega* **7,** 7320–7326 (Mar. 2022).

212. Lee, H. S., Shim, T. S., Hwang, H., Yang, S.-M. & Kim, S.-H. Colloidal Photonic Crystals toward Structural Color Palettes for Security Materials. *Chemistry of Materials* **25,** 2684–2690. ISSN: 0897-4756 (July 2013).

213. Ma, W. & Wang, Y. Effect of Salt Concentration on the Pattern Formation of Colloidal Suspension. en. *Physics Procedia* **24,** 122–126. ISSN: 18753892 (2012).

214. Martinez-Pedrero, F., Navarro-Argemí, E., Ortiz-Ambriz, A., Pagonabarraga, I. & Tierno, P. Emergent hydrodynamic bound states between magnetically powered micropropellers. *Science Advances* **4,** eaap9379 (Jan. 2018).

215. Hawman, D. W., Ahlén, G., Appelberg, K. S., Meade-White, K., Hanley, P. W., Scott, D., Monteil, V., Devignot, S., Okumura, A., Weber, F., Feldmann, H., Sällberg, M. & Mirazimi, A. A DNA-based vaccine protects against Crimean-Congo haemorrhagic fever virus disease in a Cynomolgus macaque model. en. *Nature Microbiology* **6,** 187–195. ISSN: 2058-5276 (Feb. 2021).

216. Mulligan, M. J., Lyke, K. E., Kitchin, N., Absalon, J., Gurtman, A., Lockhart, S., Neuzil, K., Raabe, V., Bailey, R., Swanson, K. A., Li, P., Koury, K., Kalina, W., Cooper, D., Fontes-Garfias, C., Shi, P.-Y., Türeci, Ö., Tompkins, K. R., Walsh, E. E., Frenck, R., Falsey, A. R., Dormitzer, P. R., Gruber, W. C., Şahin, U. & Jansen, K. U. Phase I/II study of COVID-19 RNA vaccine BNT162b1 in adults. en. *Nature* **586,** 589–593. ISSN: 1476-4687 (Oct. 2020).

217. Mateu Ferrando, R., Lay, L. & Polito, L. Gold nanoparticle-based platforms for vaccine development. en. *Drug Discovery Today: Technologies* **38,** 57–67. ISSN: 1740-6749 (Dec. 2020).

218. Trabbic, K. R., Kleski, K. A. & Barchi, J. J. J. Stable Gold-Nanoparticle-Based Vaccine for the Targeted Delivery of Tumor-Associated Glycopeptide Antigens. *ACS Bio & Med Chem Au* **1,** 31–43 (Dec. 2021).

219. Hunyadi Murph, S. E., Schyck, S. & Lawrence, K. *Engineered Nano-antenna Susceptor as Efficient Platforms For Efficient Uptake and Release of Analytes* en. in *Metal-Matrix Composites* (eds Srivatsan, T. S., Rohatgi, P. K. & Hunyadi Murph, S.) (Springer International Publishing, Cham, 2022), 351–365. ISBN: 978-3-030-92567-3.

220. Liu, X., Zhang, Y., Wang, Y., Zhu, W., Li, G., Ma, X., Zhang, Y., Chen, S., Tiwari, S., Shi, K., Zhang, S., Fan, H. M., Zhao, Y. X. & Liang, X.-J. Comprehensive understanding of magnetic hyperthermia for improving antitumor therapeutic efficacy. en. *Theranostics* **10,** 3793 (2020).

221. Hernandez, C. J. & Mason, T. G. Colloidal Alphabet Soup: Monodisperse Dispersions of Shape-Designed LithoParticles. *The Journal of Physical Chemistry C* **111,** 4477–4480. ISSN: 1932-7447 (Mar. 2007).

222. Hernandez, C. J., Zhao, K. & Mason, T. G. Well-Deposition Particle Templating: Rapid Mass-Production of LithoParticles Without Mechanical Imprinting. *Soft Materials* **5,** 13–31. ISSN: 1539-445X (June 2007).

223. Samuel, J. & Chowdhury, S. R. *Novel Lithographic Techniques for the Production of Monodisperse Colloids: LithoParticles* PhD thesis (Jan. 2007).

224. Baghdadi, Y. N., Youssef, L., Bouhadir, K., Harb, M., Mustapha, S., Patra, D. & Tehrani-Bagha, A. R. Thermal and mechanical properties of epoxy resin reinforced with modified iron oxide nanoparticles. en. *Journal of Applied Polymer Science* **138,** 50533. ISSN: 1097-4628 (2021).

225. Palfreyman, J. J., Beldon, P., Hong, B., Vyas, K. N., Cooper, J. F. K., Mitrelias, T. & Barnes, C. H. W. Fabrication of Magnetic Barcoded Microcarriers for Biomolecular Labeling: SU-8 Encapsulated Magnetic Tags. *AIP Conference Proceedings* **1311,** 184–191. ISSN: 0094-243X (Dec. 2010).

226. Peters, C., Ergeneman, O., Sotiriou, G. A., Choi, H., Nelson, B. J. & Hierold, C. Visible light curing of Epon SU-8 based superparamagnetic polymer composites with random and ordered particle configurations. eng. *ACS applied materials & interfaces* **7,** 193–200. ISSN: 1944-8252 (Jan. 2015).

Appendix A

Additional Sample Images

A.1. Additional Images for Chapter 5

Table A.1: Brief description of the SEM samples from Chapter 5 shown in this appendix.

Figure Name	wt% Polystyrene in DCM	Polymer-to-nanoparticle Ratio	THF Treatment
Figure A.1	1.5	–	False
Figure A.2	2.5	–	False
Figure A.3	5.0	–	False
Figure A.4	7.5	–	False
Figure A.5	7.5	50 : 1	False
Figure A.6	7.5	10 : 1	False
Figure A.7	7.5	50 : 1	True
Figure A.8	7.5	10 : 1	True
Figure A.9	1.5	50 : 1	False
Figure A.10	1.5	10 : 1	False
Figure A.11	1.5	50 : 1	True
Figure A.12	1.5	10 : 1	True

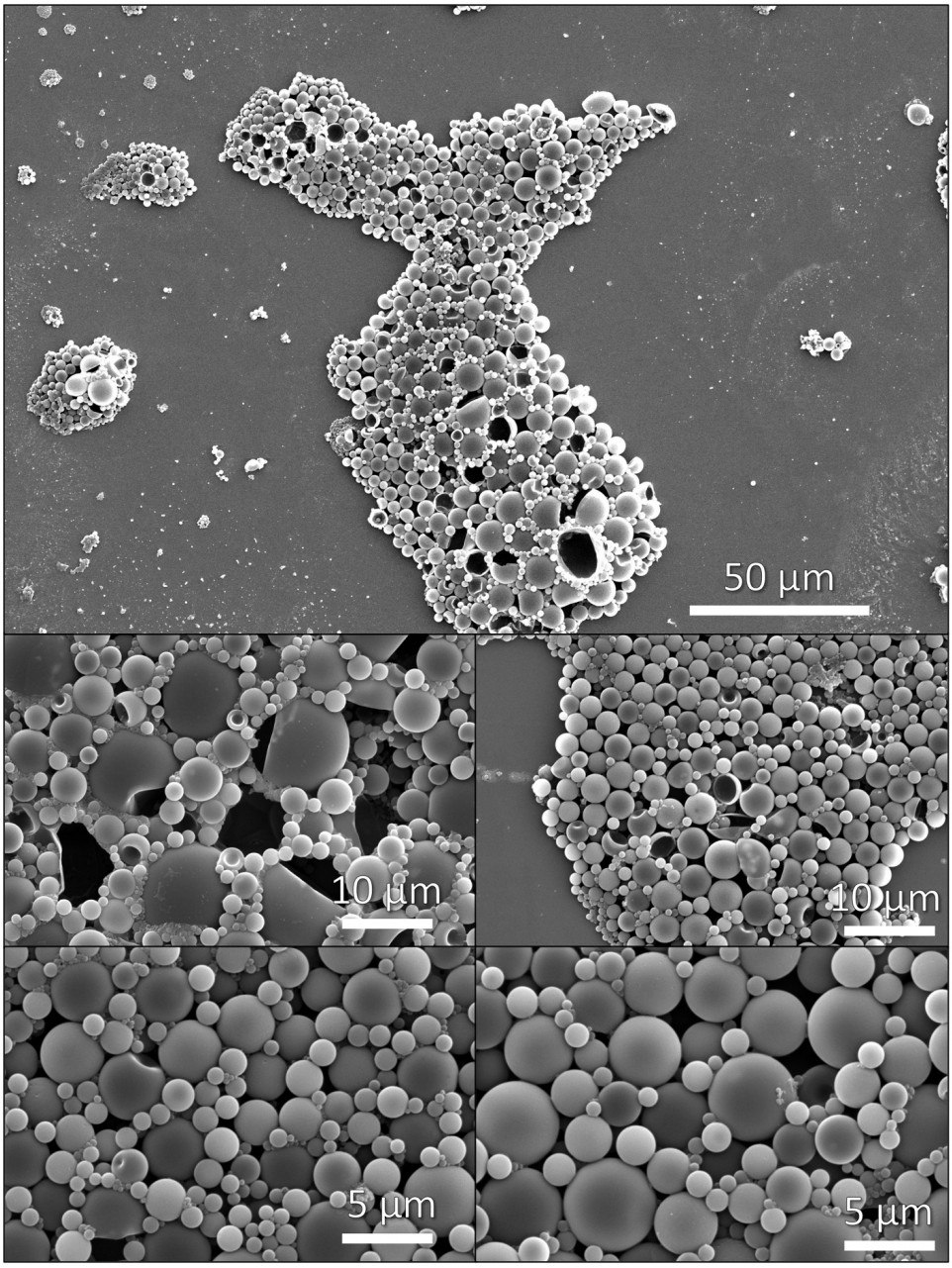


Figure A.1: SEM images of polystyrene microparticles prepared from 1.5 wt% polystyrene in DCM.

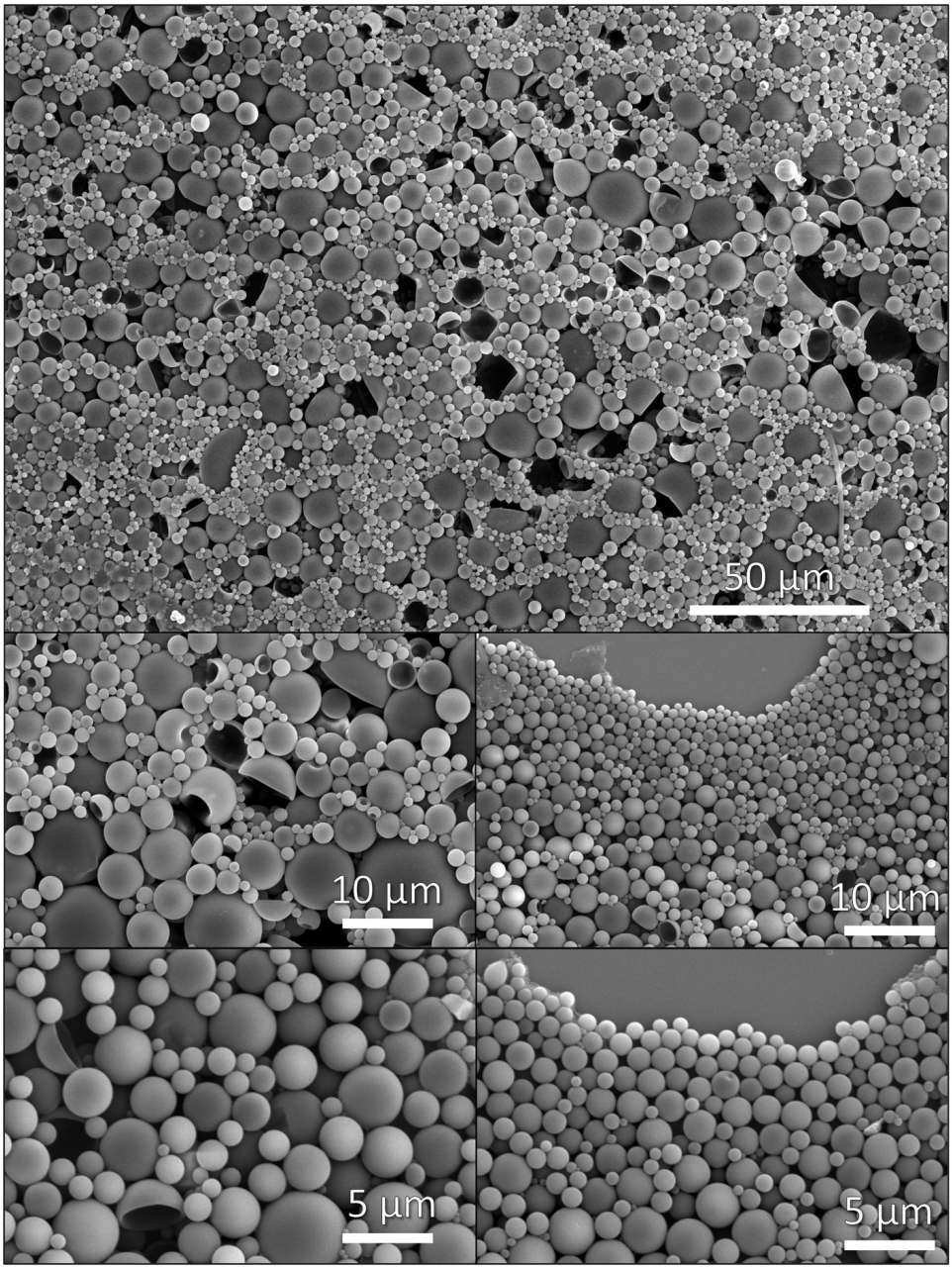


Figure A.2: SEM images of polystyrene microparticles prepared from 2.5 wt% polystyrene in DCM.

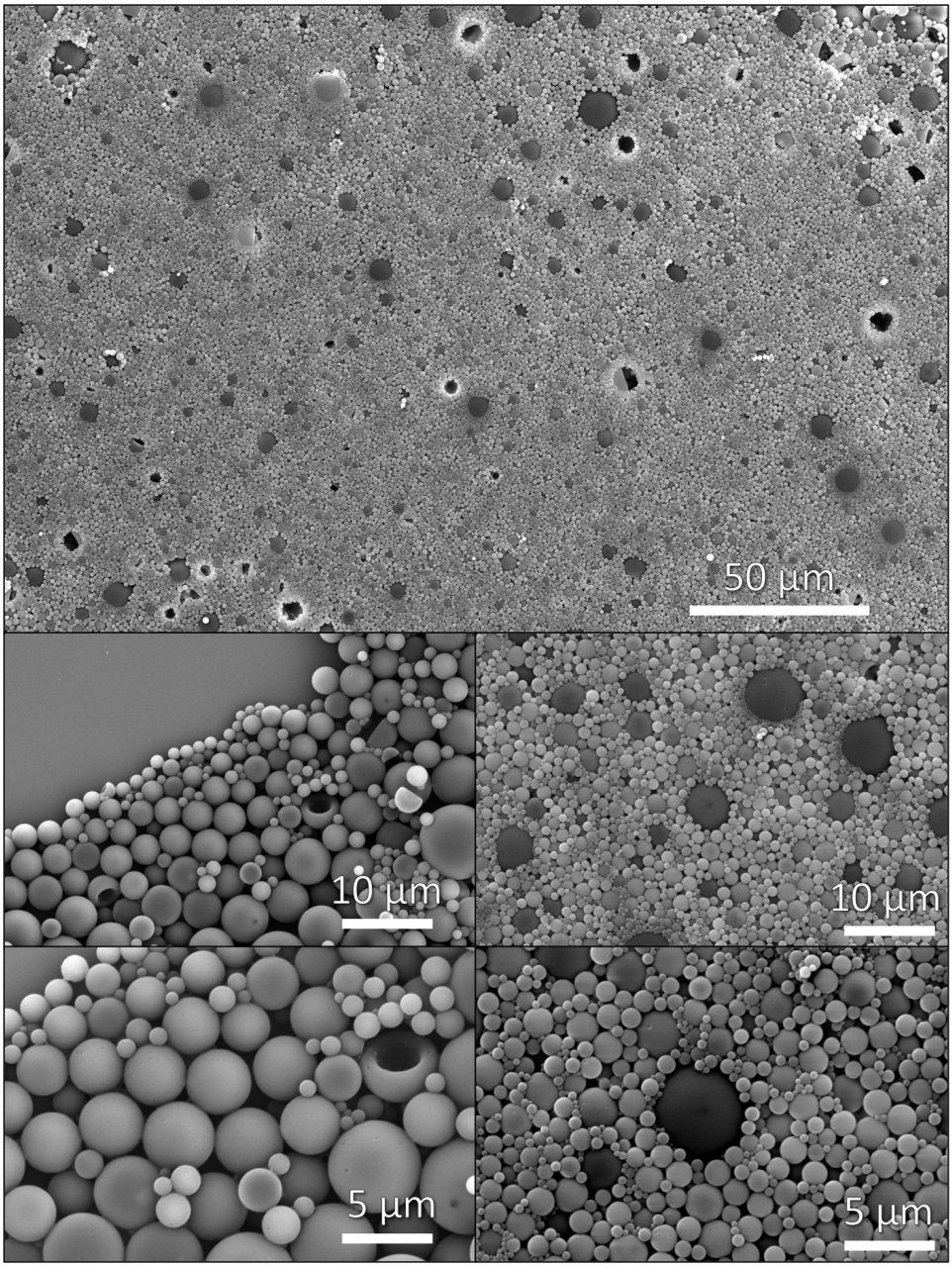


Figure A.3: SEM images of polystyrene microparticles prepared from 5 wt% polystyrene in DCM.

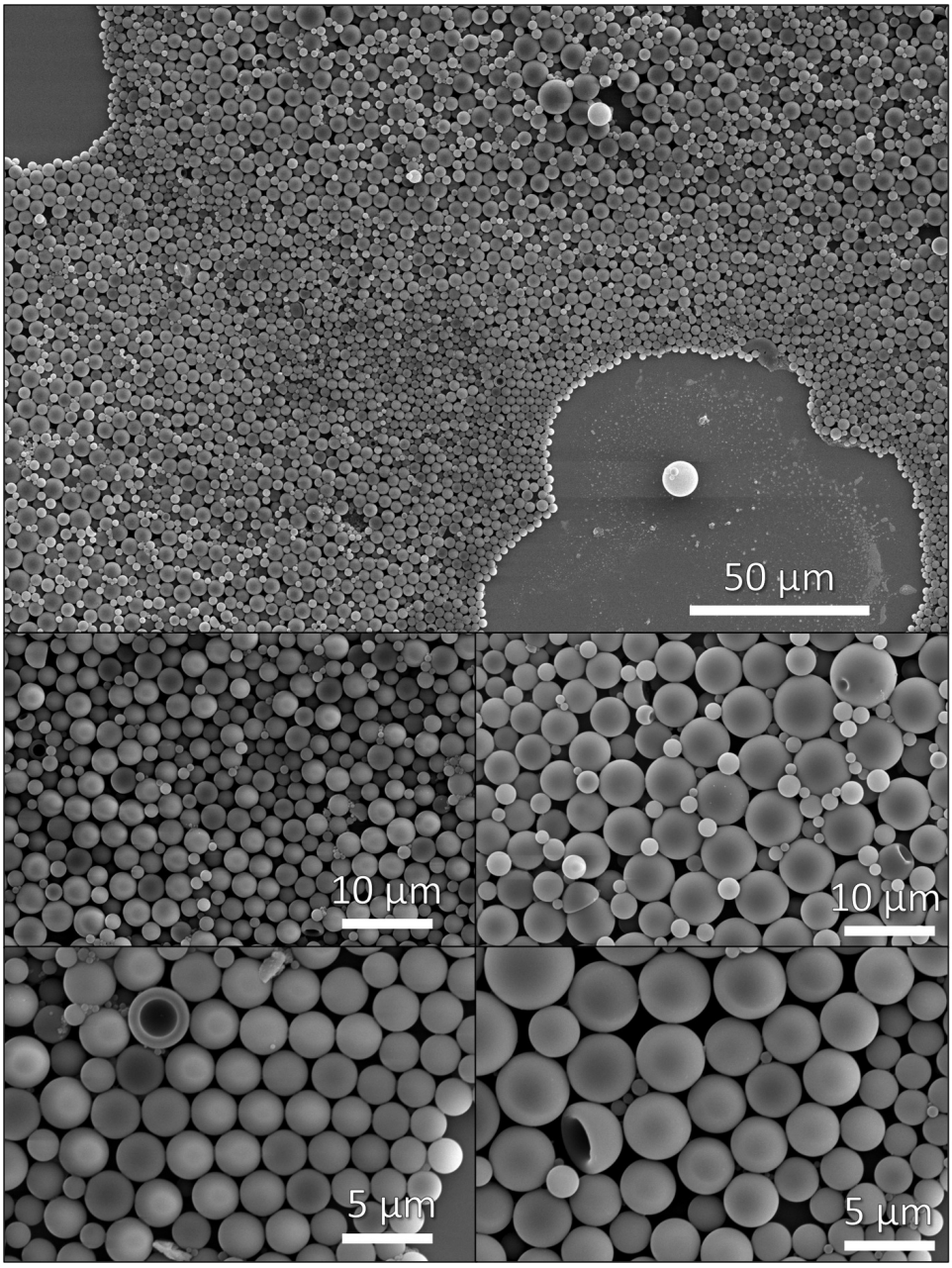


Figure A.4: SEM images of polystyrene microparticles prepared from 7.5 wt% polystyrene in DCM.

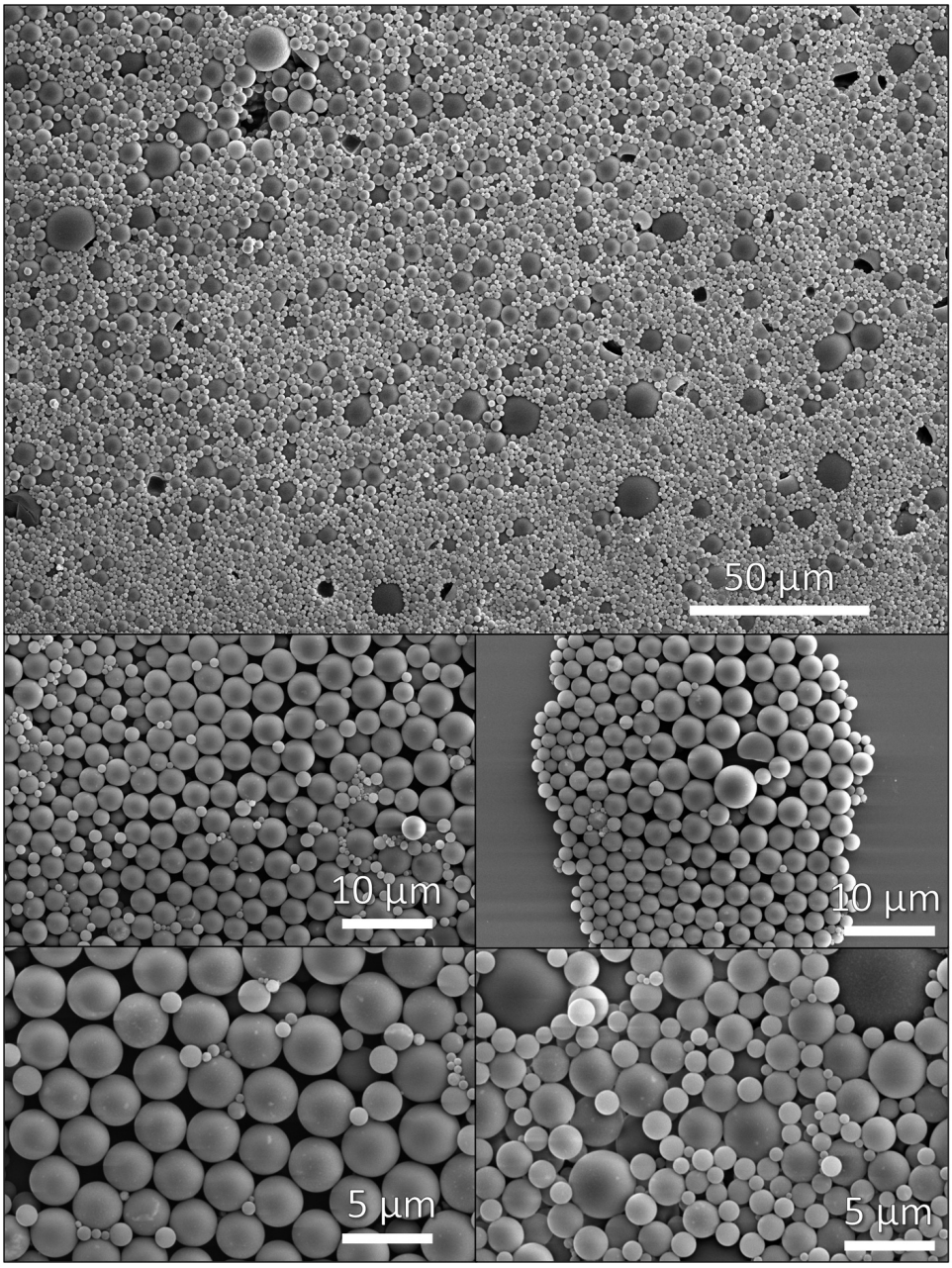


Figure A.5: SEM images of polystyrene microparticles prepared from a DCM solution containing 50:1 polymer-to-nanoparticle ratio with 7.5 wt% polystyrene in DCM.

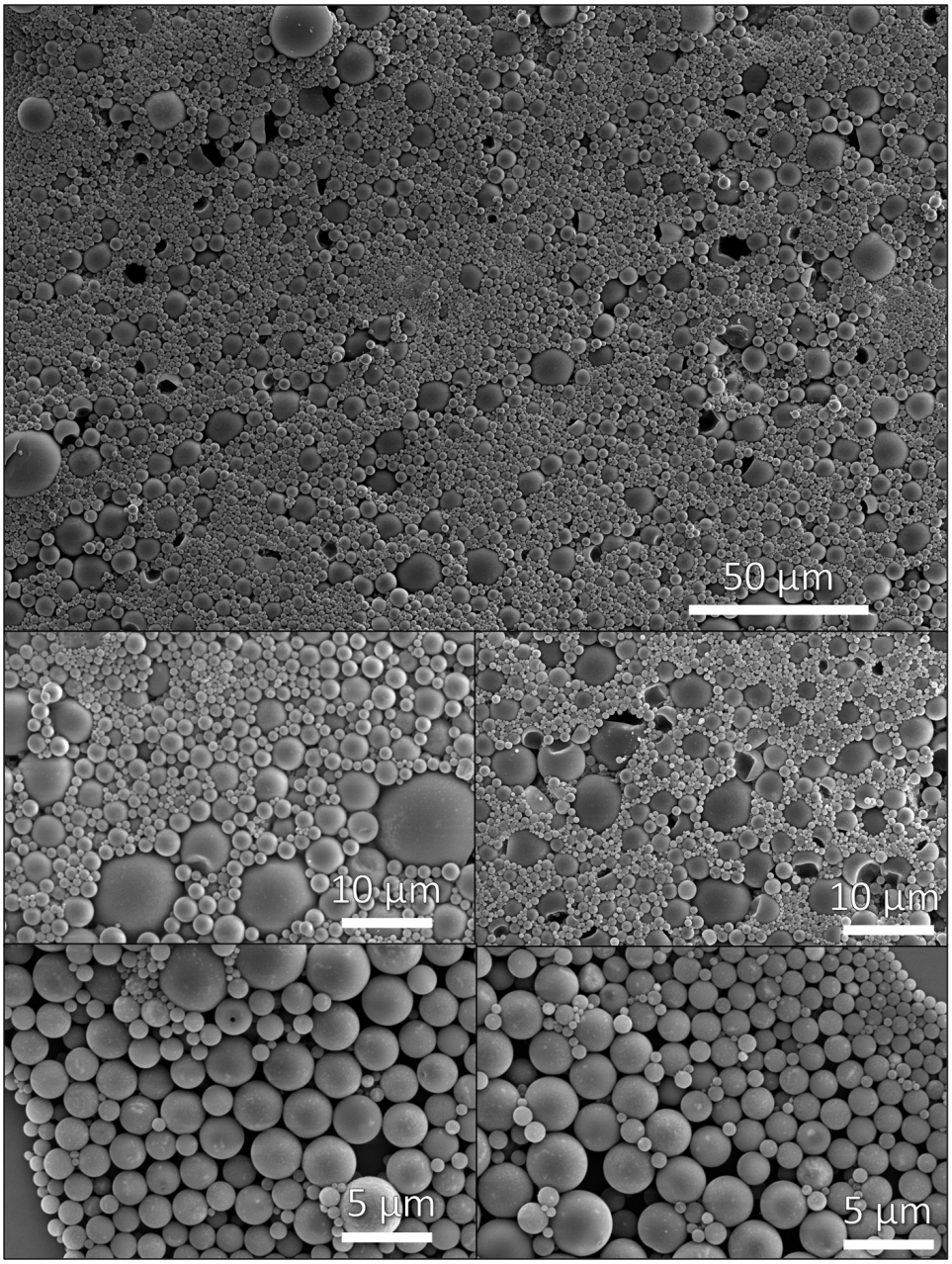


Figure A.6: SEM images of polystyrene microparticles prepared from a DCM solution containing 10:1 polymer-to-nanoparticle ratio with 7.5 wt% polystyrene in DCM.

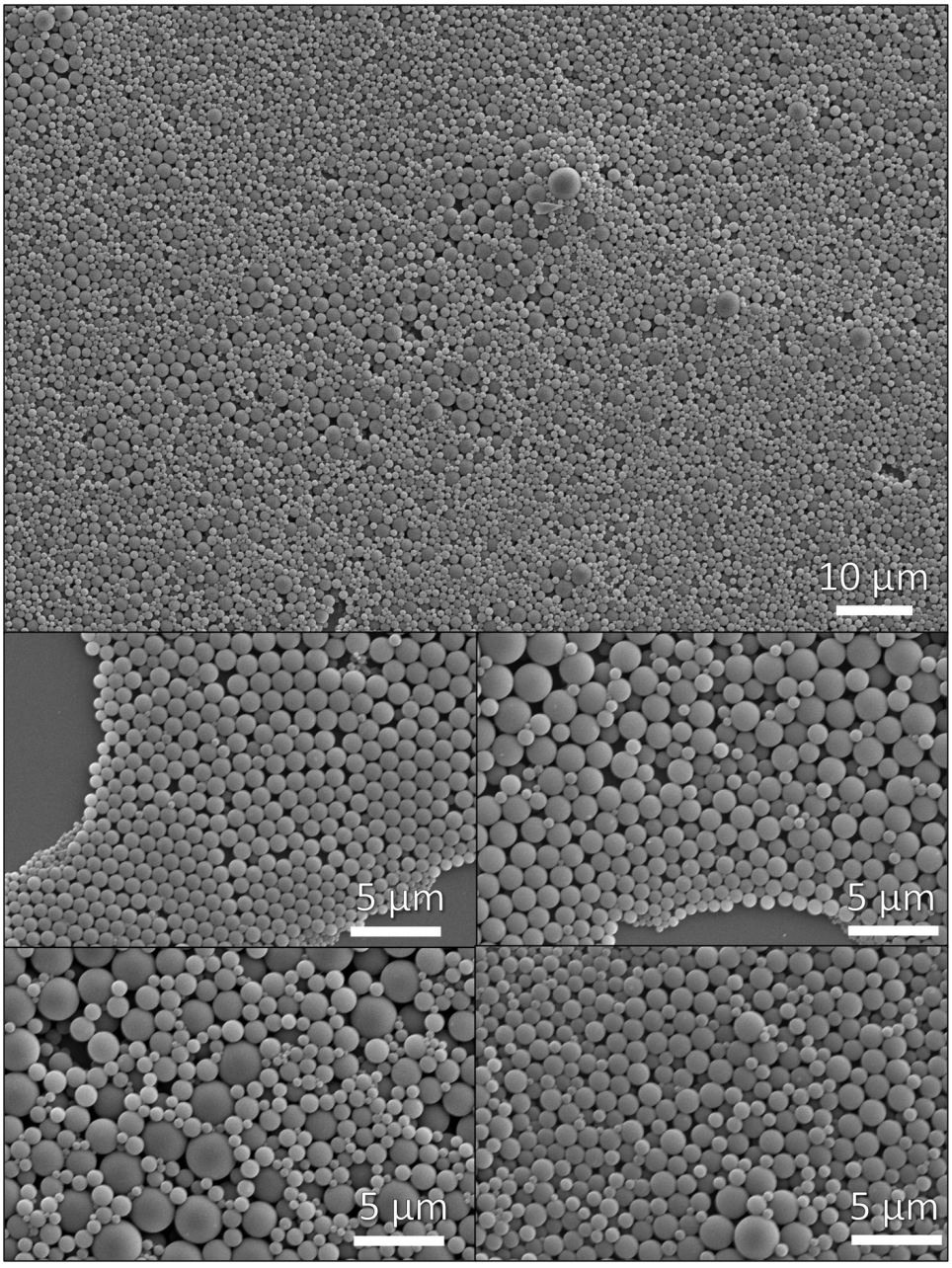


Figure A.7: SEM images of polystyrene microparticles after THF treatment prepared from a DCM solution containing 50:1 polymer-to-nanoparticle ratio with 7.5 wt% polystyrene in DCM.

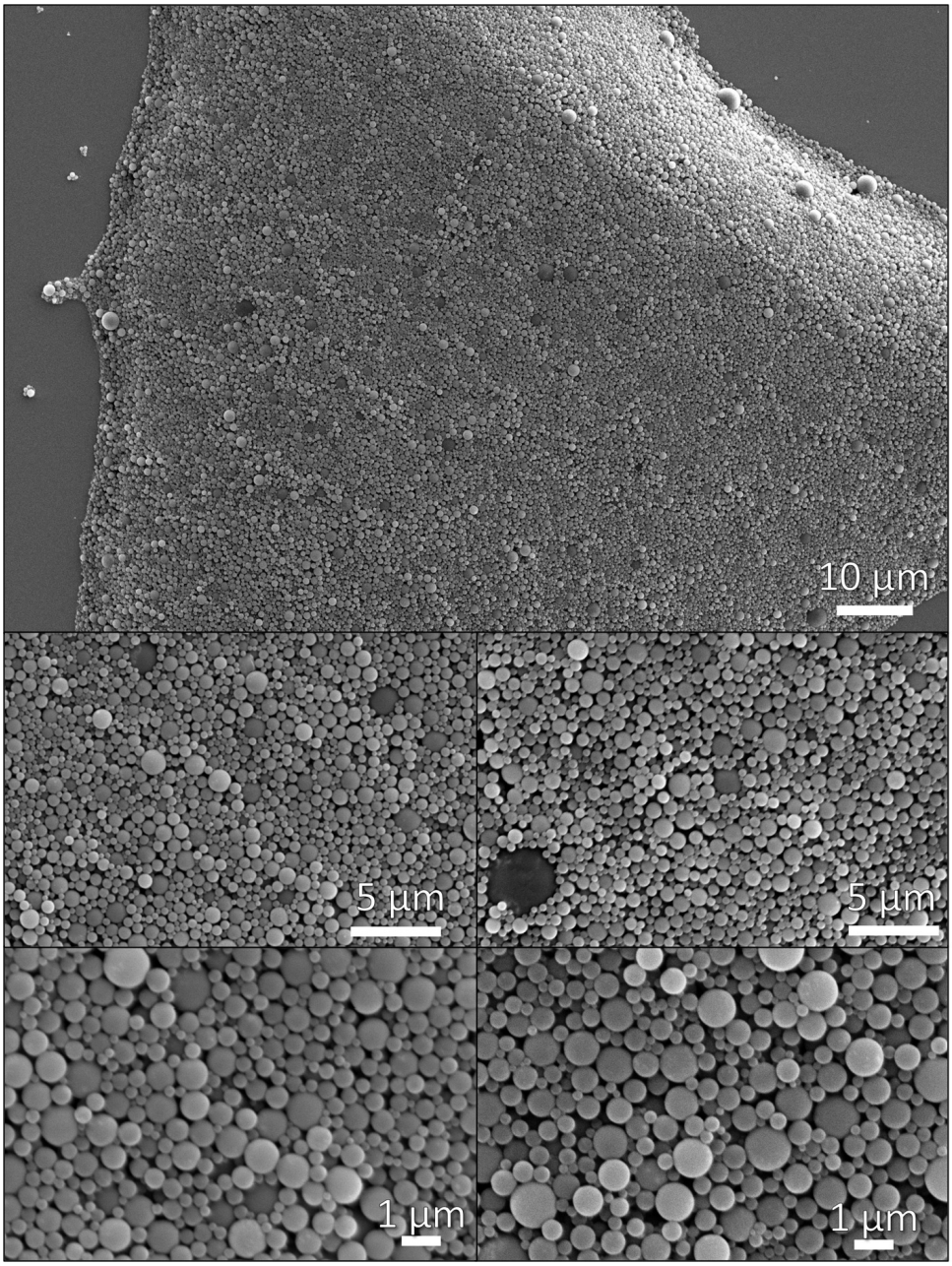


Figure A.8: SEM images of polystyrene microparticles after THF treatment prepared from a DCM solution containing 10:1 polymer-to-nanoparticle ratio with 7.5 wt% polystyrene in DCM.

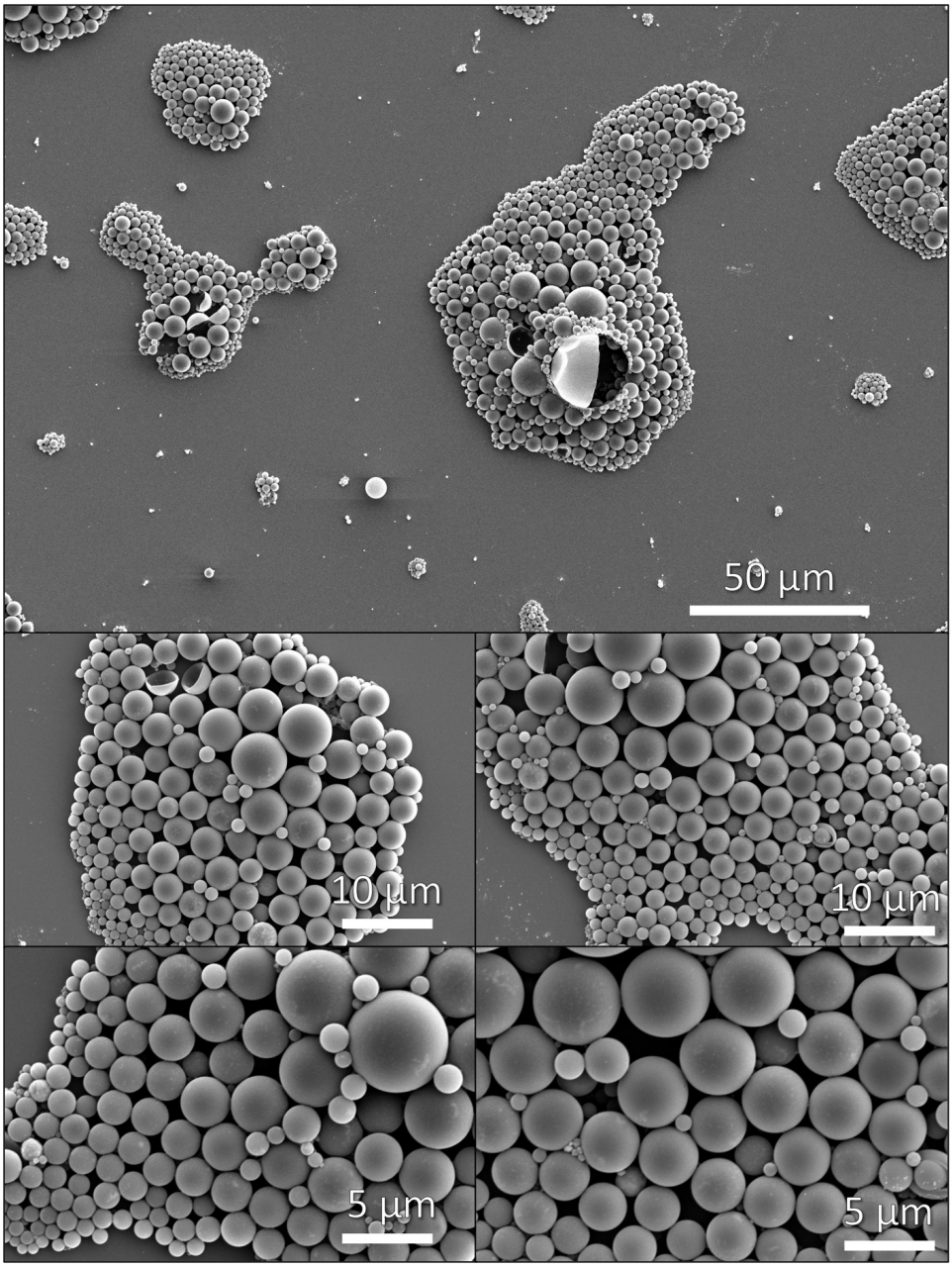


Figure A.9: SEM images of polystyrene microparticles prepared from a DCM solution containing 50:1 polymer-to-nanoparticle ratio with 1.5 wt% polystyrene in DCM.

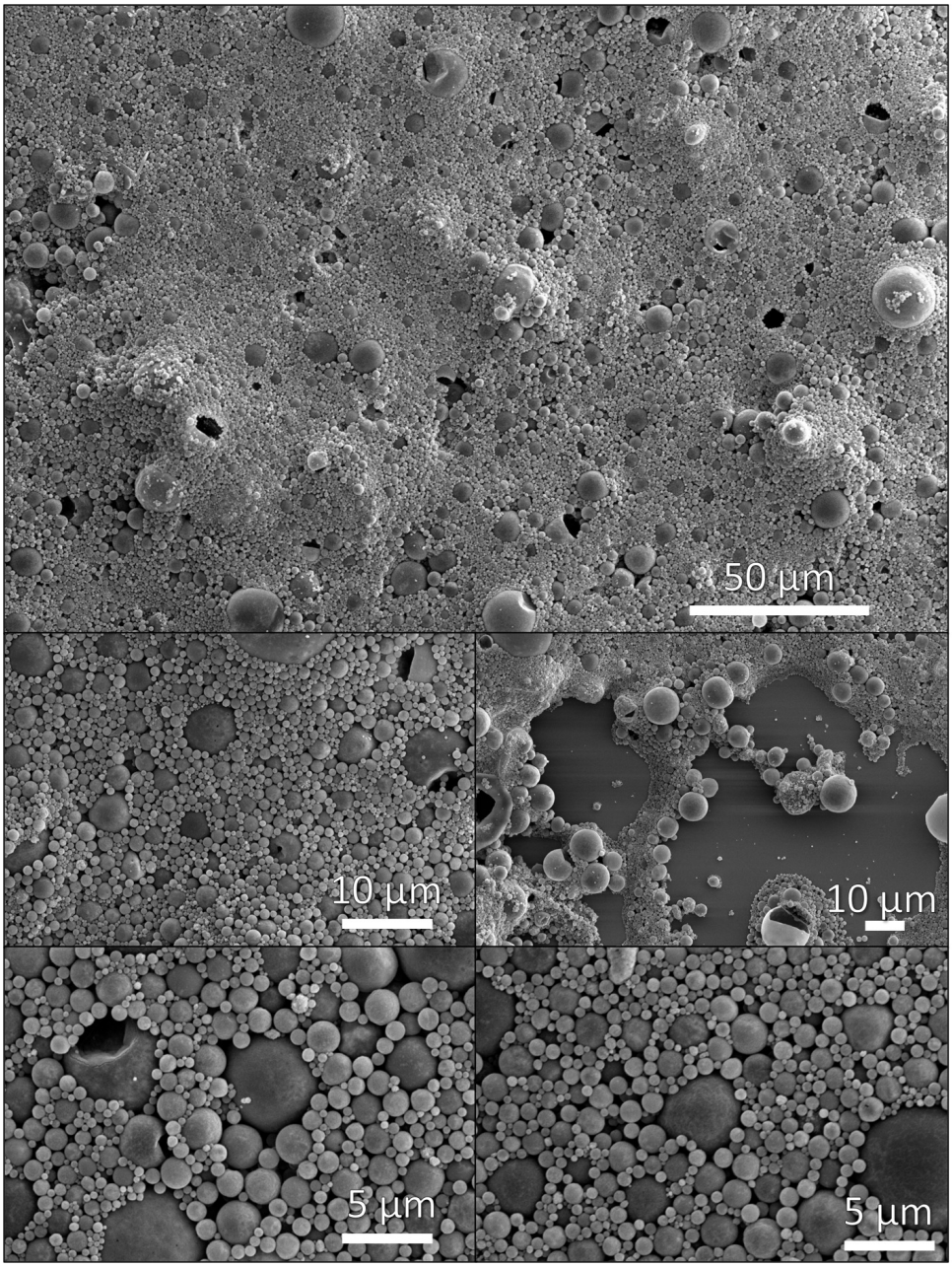


Figure A.10: SEM images of polystyrene microparticles prepared from a DCM solution containing 10:1 polymer-to-nanoparticle ratio with 1.5 wt% polystyrene in DCM.

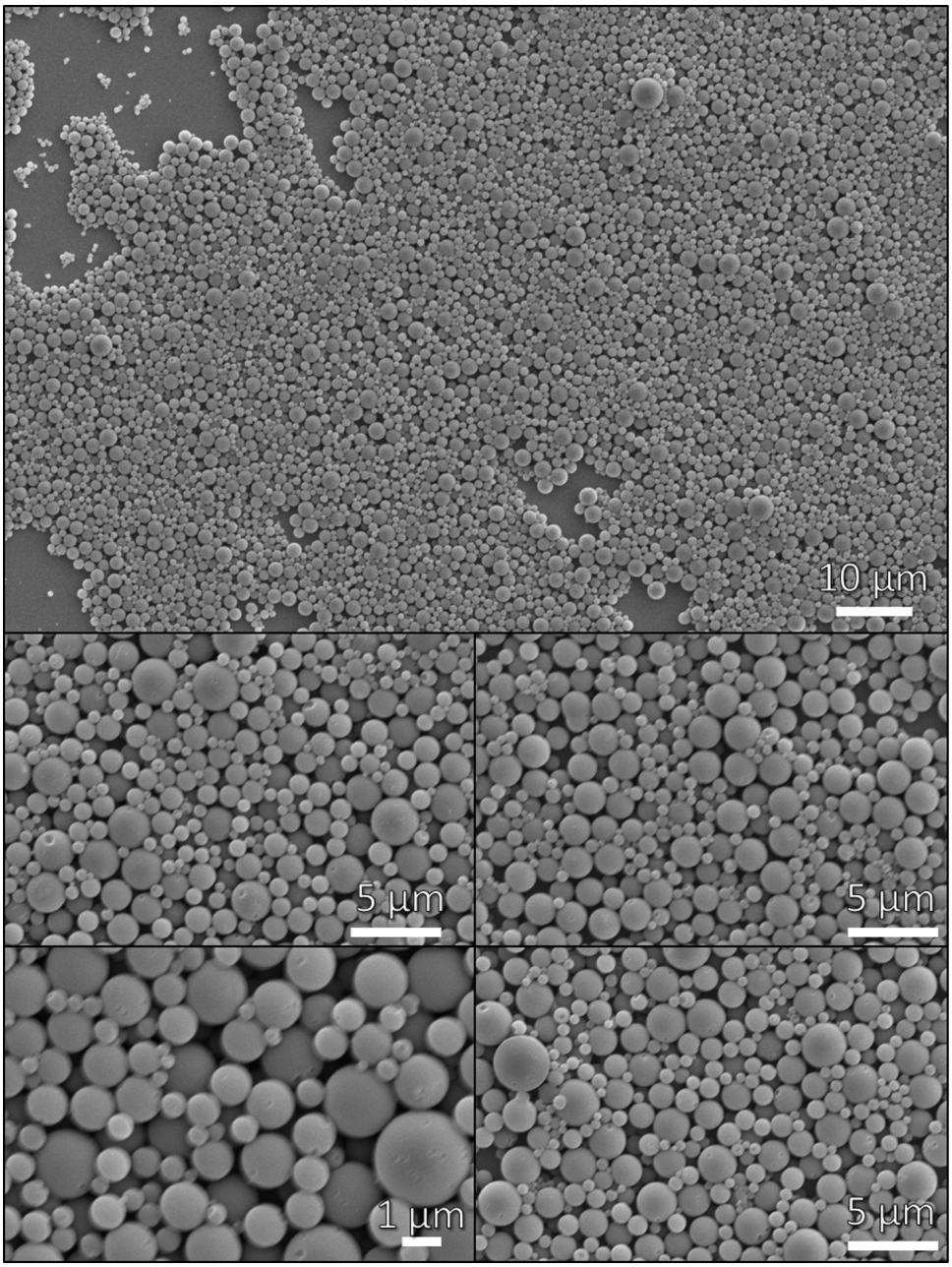


Figure A.11: SEM images of polystyrene microparticles after THF treatment prepared from a DCM solution containing 50:1 polymer-to-nanoparticle ratio with 1.5 wt% polystyrene in DCM.

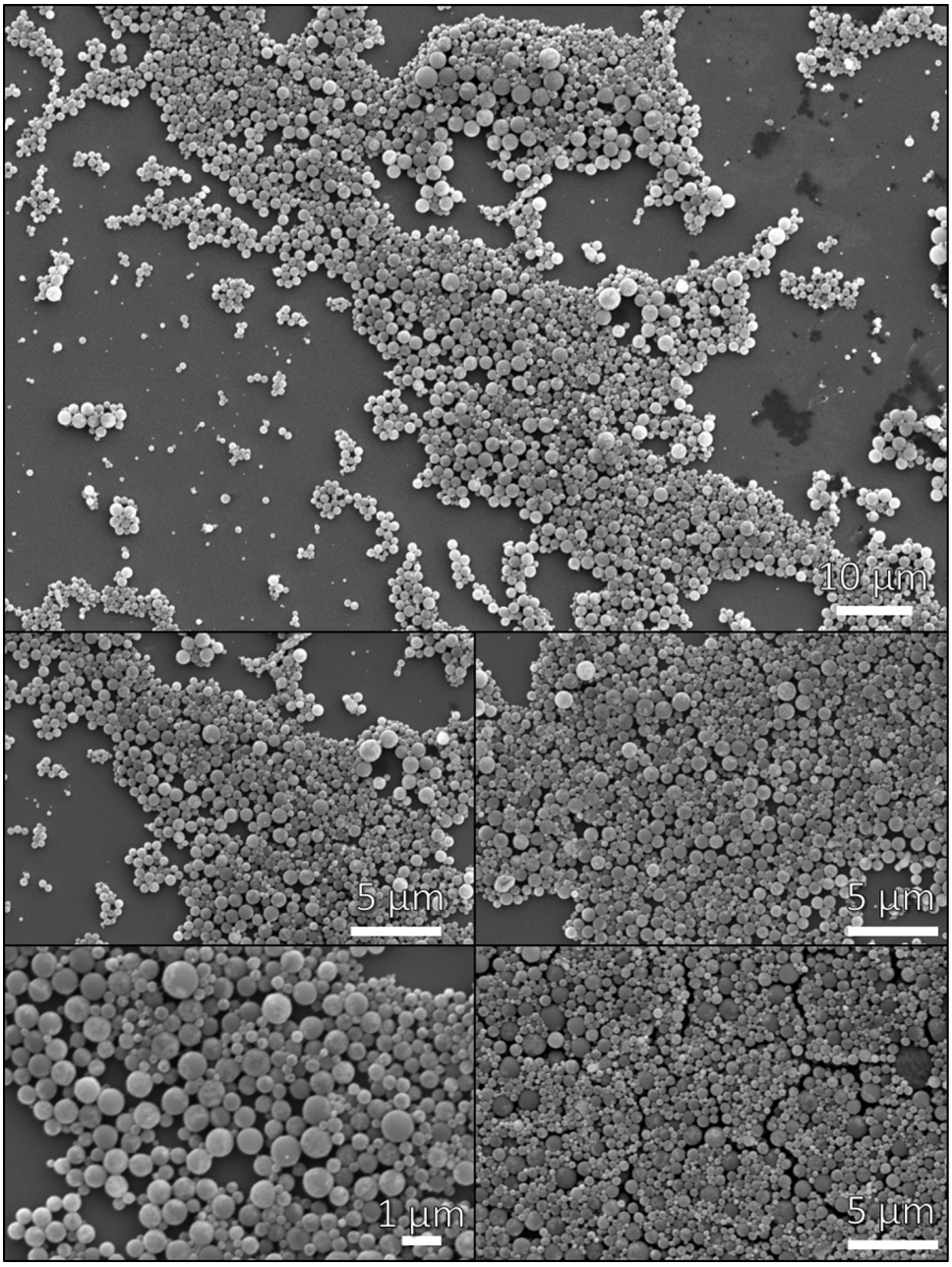


Figure A.12: SEM images of polystyrene microparticles after THF treatment prepared from a DCM solution containing 10:1 polymer-to-nanoparticle ratio with 1.5 wt% polystyrene in DCM.

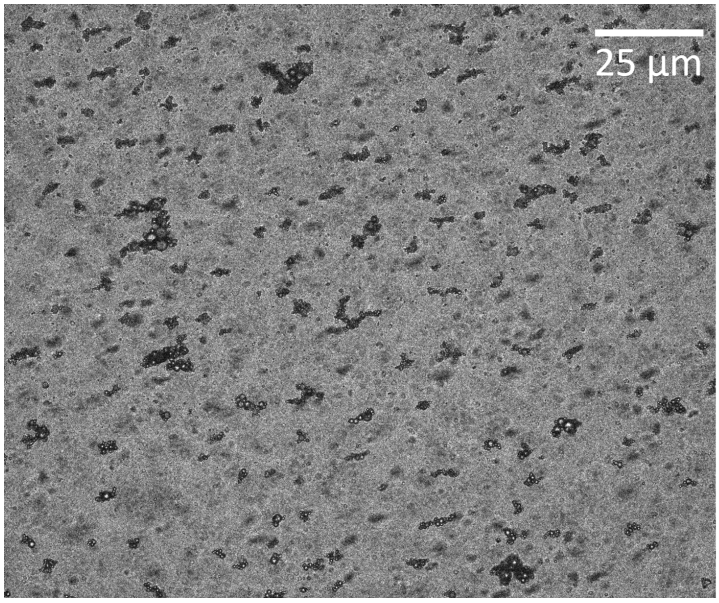


Figure A.13: Optical microscopy image of resultant particles formed from DCM droplets with 0.01 wt% SDS. This corresponds another area in the same capillary shown in Figure 5.3 A.

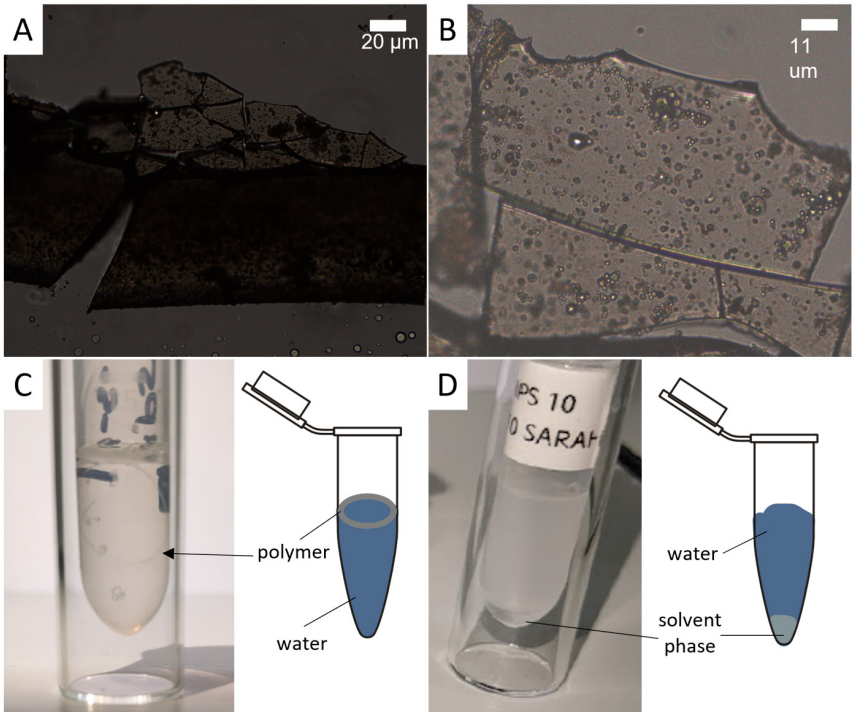


Figure A.14: Optical microscopy images of polymeric aggregates/films formed at (A) 20 vol% and (B) 1.25 vol% solvent phase. (C) Images and schematics of prepared samples at (C) 1.25 vol% and (D) 20 vol% solvent phase.

Summary

Since their initial discovery in the early 1800s, colloidal particles, with their diverse range of distinctive and frequently material-dependent properties, have attracted the curiosity of researchers from a wide range of fields. In this thesis, we explore the design of self-assembled materials formed from anisotropic particles based on their shape as well as their interactions. We also investigate ways to alleviate some of the limitations that current anisotropic and magnetic colloidal particles encounter as photocatalytically active particles. Additionally, we aim to develop novel techniques for anisotropic composite magnetic microparticle preparation.

The first part of the this thesis deals with the self assembly of colloidal superballs, a unique cube-like shape family that smoothly interpolates between a sphere and a cube. We assemble colloidal superballs inside evaporating droplets and probe the assembly process via small-angle x-ray scattering (SAXS). Chapter 2 explores the effect of superball shape on the resultant assembled structure. We observe and characterize four distinct drying regimes that emerge as our hollow silica superballs assemble inside the shrinking droplet. We discovered that they arrange into the predicted paracrystalline, rhombohedral C_1-lattice, which varies depending on the shape of the individual superballs. In Chapter 3, we assemble colloidal superballs possessing permanent magnetic moments to investigate the assembly process with additional dipole-dipole interactions as well as anisotropic shapes. As the particles assemble inside an evaporating droplet, we observe the formation of particle shape-dependent structures similar to their non-magnetic counterparts. When we apply a magnetic field during the drying process, we discover that large magnetic fields impede the formation of well-ordered assemblies due to the formation of out-of-equilibrium dipolar structures, but lower magnetic fields allow particles to reorganize and orient without inhibition. The ability to tune these interactions based on shape and magnetism of the assemblies constituent particles will allow for the controllable formation of macroscopic colloidal assemblies as functional materials.

The second part of this thesis explores how we can improve current photocatalytically active hematite microparticles for use as self-propelled swimmers since these systems are of interest in applications such as cargo delivery, environmental remediation, and modeling biological systems. Chapter 4 presents a general approach to improve the activity of hematite microswimmers. We calcine hematite microparticles and observe their swimming behavior using optical microscopy and particle tracking in this approach. We investigate the mean-squared displacement (MSD) of the particles, and we discover that calcination leads in a maximum 87-fold increase in MSD at 1-minute lag times, depending on the calcination time. This increased activity makes hematite more accessible to key areas of soft matter and photocatalysis research.

The final part of this thesis examines different techniques for the preparation of anisotropic composite magnetic microparticles. Polymeric particles are already used in a range of applications and have well-established synthetic techniques. When other components are incorporated into the polymeric matrix, the particles gain additional,

desirable properties. In Chapter 5, we look into a simple yet flexible synthetic method for making micron-sized polystyrene particles loaded with magnetic cobalt ferrite nanoparticles. This method utilizes the evaporation of an emulsion droplet containing polymer and magnetic nanoparticles to form composite polymeric microparticles with tunable sizes and magnetic content. Due to the evaporation process, large (>5 μm) particles contain porous or hollow internal structures which we solidify via addition of a small amount of the polymers' plasticizer. The particles produced from this method are all spherical in nature. In Chapter 6, we apply a thermal stretching method to our composite polymeric particles to form anisotropic, ellipsoidal, microparticles. In the final chapter, Chapter 7, we discuss the current state and limitations that we faced throughout this work while looking forward into the research we expect to see within this field.

Samenvatting

Sinds hun eerste ontdekking in het begin van de 19e eeuw hebben colloïdale deeltjes, met hun diverse onderscheidende en vaak materiaalafhankelijke eigenschappen, onderzoekers uit een breed scala van vakgebieden geïnteresseerd. In dit proefschrift hebben we het ontwerp van zelf-geassembleerde materialen, gevormd uit anisotrope deeltjes, onderzocht op basis van hun vorm en hun interacties. We hebben methoden onderzocht om enkele van de beperkingen te overwinnen waarmee anisotrope en magnetische colloïdale deeltjes als fotokatalytisch actieve deeltjes worden geconfronteerd. Daarnaast wilden we nieuwe technieken ontwikkelen voor de bereiding van anisotrope composiet magnetische microdeeltjes.

Het eerste deel van dit proefschrift gaat over de zelfassemblage van colloïdale superballen, een unieke familie van kubusachtige vormen die soepel interpoleert tussen een bol en een kubus. We hebben colloïdale superballen geassembleerd in verdampende druppels en het assemblageproces onderzocht via small-angle x-ray scattering (SAXS) (Hoofdstuk 2). We onderzochten het effect van de vorm van een superbal op de resulterende geassembleerde structuur. We observeerden en karakteriseerden vier verschillende droogregimes die ontstaan wanneer onze holle silica-superballen zichzelf assembleren in de krimpende druppel. We ontdekten dat ze gerangschikt zijn in het voorspelde parakristallijne, rhombohedrale C_1-rooster, dat varieert afhankelijk van de vorm van de individuele superballen.

In Hoofdstuk 3 hebben we colloïdale superballen met permanente magnetische momenten in elkaar gezet om het assemblageproces te onderzoeken waarbij extra dipool-dipoolinteracties en anisotrope vormen aanwezig waren. Terwijl de deeltjes zichzelf assembleren in een verdampende druppel, zagen we de vorming van deeltjesvormafhankelijke structuren vergelijkbaar met hun niet-magnetische tegenhangers. Toen we tijdens het droogproces een magnetisch veld aanbrachten, ontdekten we dat grote magnetische velden de vorming van goed geordende assemblages belemmeren vanwege de vorming van geassembleerde dipolaire structuren, maar lagere magnetische velden zorgen ervoor dat deeltjes zich ongehinderd kunnen reorganiseren en oriënteren. Het vermogen om deze interacties af te stemmen op basis van vorm en magnetisme van de samenstellende deeltjes zal de controleerbare vorming van macroscopische colloïdale assemblages als functionele materialen mogelijk maken.

Het tweede deel van dit proefschrift onderzoekt hoe we de huidige fotokatalytisch actieve hematiet-microdeeltjes kunnen verbeteren voor gebruik als zelfrijdende zwemmers, aangezien deze systemen interessant zijn voor toepassingen zoals het afleveren van vracht, milieusanering en het modelleren van biologische systemen (Hoofdstuk 4). We presenteren een algemene aanpak om de activiteit van hematiet microzwemmers te verbeteren. We calcineerden hematiet-microdeeltjes en observeerden hun zwemgedrag met behulp van optische microscopie en het volgen van deeltjes in deze benadering. We onderzoeken de gemiddelde vierkante verplaatsing (MSD) van de deeltjes en vinden dat calcinering leidt tot een maximale 87-voudige toename van MSD bij vertragingstijden

van 1 minuut, afhankelijk van de calcineertijd. Deze verhoogde activiteit maakt hematiet toegankelijker voor belangrijke gebieden van onderzoek naar zachte materie en fotokatalyse.

Het laatste deel van dit proefschrift onderzocht verschillende technieken voor de bereiding van anisotrope composiet magnetische microdeeltjes. Polymere deeltjes worden al in een reeks toepassingen gebruikt en hebben gevestigde synthetische technieken. Wanneer andere componenten in de polymere matrix worden opgenomen, krijgen de deeltjes extra gewenste eigenschappen. In Hoofdstuk 5 onderzochten we een eenvoudige maar flexibele synthetische methode voor het maken van polystyreendeeltjes van micronformaat geladen met magnetische nanodeeltjes van kobaltferriet. Deze methode maakt gebruik van de verdamping van een emulsiedruppel die polymeer en magnetische nanodeeltjes bevat om samengestelde polymere microdeeltjes te vormen met instelbare afmetingen en magnetische inhoud. Vanwege het verdampingsproces bevatten grote (>5 μm) deeltjes poreuze of holle interne structuren die we stollen door toevoeging van een kleine hoeveelheid van de weekmaker van de polymeren. De deeltjes die door deze methode worden geproduceerd, zijn allemaal bolvormig. In Hoofdstuk 6 hebben we een thermische rekmethode toegepast op onze samengestelde polymeerdeeltjes om anisotrope, ellipsvormige microdeeltjes te vormen. In het laatste hoofdstuk, Hoofdstuk 7, bespraken we de huidige staat en beperkingen waarmee we te maken kregen tijdens dit werk, terwijl we vooruitkijken naar het onderzoek dat we op dit gebied verwachten.

Acknowledgments

I would like to express my sincere gratitude to my supervisor, Dr. Laura Rossi, for her invaluable guidance and support throughout my PhD journey. Laura, you have taught me how to conduct strong scientific research, and how to advocate for what I think is right. You have always encouraged me to pursue my interests and challenged me to grow as a researcher. Of course, if I had never taken this PhD, I would probably still be in the States. In this sense, you have also shown me a lot of the world that I may have never been able to see otherwise. I have truly learned a lot from these experiences and enjoyed them immensely. I am very lucky to have had such a wonderful mentor and role model.

Many thanks also to my promotor, Pouyan, for always making me feel welcome whether it is inviting me to the group meetings or passing by my office to say hello. I also appreciate your valuable input during my presentations, and how you helped me find ways to make my research and my communication about it stronger. Your guidance has truly shaped my academic and professional growth. In addition, I would also like to thank my committee members who took the time to assess my dissertation and participate in my defense: Prof. Atsushi Urakawa, Prof. dr. Albert Philipse, Dr. Joshua Dijksman, Dr. ir. Claire Chassagne, and Prof. dr. Stefano Sacanna.

I would also like to express my gratitude to the other ASM PI's for contributing to my growth as a scientist and giving me room to speak up for the PhD's in the staff meetings. You have been supportive and encouraging mentors who have challenged me to improve my skills and knowledge. I appreciate your feedback and guidance throughout my PhD journey. Specifically, I want to thank Reink for letting me join some of his group dinners. They were always fun and relaxing, and I enjoyed getting to know you and your family better. Jan, Eduardo, Stephen, Wolter, and Marcel, thank you for the friendly conversations we would have and the nice discussions during the ASM Science Discussion. You have taught me a lot about different aspects of science and inspired me to pursue my own interests. And Wolter, thank you for hanging out with us PhD's at CHAINS!

Next, I would like to thank the technicians who supported me throughout these 4 years. First, I thank Duco for his invaluable assistance with the scanning electron microscopy (SEM) experiments. He was always patient and helpful, and taught me a lot about the instrument and its applications. I also appreciate his friendship and the fun times we had outside the lab, especially the memorable hot pot dinner that left us all in tears from the spiciness. Secondly, I thank Marcel for his expertise and guidance with the atomic force microscopy (AFM) measurements. He was always ready to lend a hand and share his insights, and he also contributed to the social atmosphere of the group by hyping up the borrels and organizing a nice Christmas dinner. I also thank Seitse and Aleksandra for their professionalism and dedication in maintaining the lab facilities and equipment. I always enjoy lab cleaning, so that I can see our beautiful clean labs and then enjoy a drink (and some pizza!) with you afterwards. Finally, I would like to thank Xiaohui, for assistance with the x-ray diffraction (XRD) setups downstairs, as well as Bahiya (and Michael), for showing me all the fun tools I could use in the OM group. Of course, I

am grateful for all of the technicians who have helped me throughout my thesis for their support and encouragement.

I am also honored to have been able to supervise several students throughout my PhD. Their dedication, hard work, and enthusiasm have been a constant source of inspiration for me, and their contributions have been invaluable in shaping some the ideas presented in this thesis. In particular, Lex and Donna, your collaboration in navigating the lab during the challenging COVID-19 restrictions truly brought out our creativity and helped us overcome various obstacles. Giovanna, first you were my student, and now you are my colleague. It has been a great experience to witness firsthand how you have grown since you joined us as an MSc student. Not only that, but you and Silvana showed me what it truly means to be a supervisor when Laura was on leave. Silvana, your dedication and organization throughout your MSc thesis were exceptional. Your hard work has paid off, and we have gained valuable insights into our active particle system beyond what we had expected. It was a pleasure to see you at Physics @ Veldhoven as a fresh PhD! Alexander, your BSc was a fun project not only because I enjoyed the research we did but also your attitude and personality made for a great (and short) 11 weeks! Nitin, you have prepared an enormous amount of polystyrene particles, and all the hard work has paid off with excellent results. As a result, we now have a patent related to the process! Finally, Stefanie, even though I was not your official daily supervisor, I really enjoyed discussing your project with you and learning so much about hematite's nanostructure. Of course, it was also a lot of fun to take a long drive with you and Laura to France.

Apart from students, a lot of this work would have never been completed without collaborations from people outside my group and section. Andrei, I would like to thank you for always being enthusiastic about x-ray scattering and teaching me so much about synchrotrons and scattering. I always appreciate our conversations or taking a walk to see the red monster at ID32. Janne-Mieke, I would like to thank you for great discussions on how to analyze some of the most difficult data to work with. It was always nice to join a meeting where you were excited about my new updates on our colloidal assemblies. You were always a friendly face I was happy to find at a conference. Also, Max, I want to thank for putting up with me on the night shift at the synchrotron - I will probably always remember it when I watch a bad zombie movie. Lucia, it was a pleasure to work with some of your previously collected data. I'm grateful for the great data organization and pleasant collaboration. Peter, thank you for all your invaluable insights in the superball assembly project. We ended up with a very nice project. Georgy, thank you for always throwing a bone to the orphans next door. I always appreciate your help with the microscopes and other curiosities around the lab as well as any excuse to have a coffee and enjoy what sunshine the Netherlands has to offer.

Of course, I cannot get away with this acknowledgments section without mentioning all of my PhD cohort that I have closely spent the last four years with. Some PhD's have left before me, as is life in D2.260. Susan, I arrived to see you leave, thanks for showing me my first TUDelft PhD defense. Michelle, it was nice to work with you and try to assemble colloids with your unique system. Bowen, it was always fun to chat with you over lab clean dinner. I'm glad that I can still keep in touch with you as you work on your postdoc in the States. Hope that you are enjoying your time there as an American would. Tobias, I really liked having someone to chat to about the best way to BBQ a brisket and can have

a round of golf on the occasional sunny day in the Netherlands. Guotai, thanks for all the funny moments from the complaints about late lunch deliveries to having "too much" of my Swiss chocolate I brought one day. Hendrik and Benni, I always had fun catching up with you over coffee and visiting your house with seemingly too many rooms. I'm glad that we got to play some fun games throughout my time here. Juncheng, I always enjoyed hearing about your cycling adventures through the Netherlands. Elmira, I still remember our great group adventure in your car to Delftse Hout. I wish you the best with your future career! Ardeshir, thanks for being my MTP pal - I can only hope that my notes actually helped with your final round of that course. Anand, it was nice to chat with you about PhD life and new movies over lunch or lab clean. Best of luck finishing up your thesis! Gijs and Tamar, I'm glad that we could meet, even though our overlap here at ASM was brief. I hope that you will be able to keep the spirit of ASM alive. Benjamin, thank you for always being so welcoming to the group. Without some of your initial invites to group dinners and drinks, I may have never left my shell and would have remained that quiet Sarah from those first days. Hopefully, I didn't receive too many negative marks from not saying hello in the hall. I hope that you keep up the friendly attitude in your future career, and that we can still grab a drink at Bebop. Peggy, even though you weren't in the PhD program with us, I still enjoyed the time together with you at ASM. You always were excited to show me some new results that you had collected! I'm happy that you found a nice job that you enjoy, and I hope that I will still find you around town to catch up.

Suellen, I always enjoyed our coffee and tea breaks, especially when the day was getting close to 6 p.m. and I was tired and wanted to go home. Whether we were discussing stretchy polymers, lab worries, or weekend plans, I was always glad that you were there to support me, especially on days when I found a mess in the lab. I'm grateful that we could spend so much time outside of the lab exploring the great city of Delft! Irene, thank you for showing me how fun PhD life could be, well, when we were not in the lab. I loved going to your home in Italy and truly experiencing the Italian lifestyle, even if I did it incorrectly in the end. To be honest, I might not have survived this PhD without you two. Thank you both for all the girls' nights, coffee breaks, and discussions on how we would make whatever broken lab equipment work. I wish both of you the best for your futures.

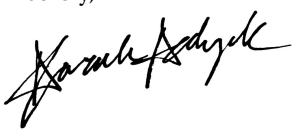
Wow, I've finally made it to the people outside of the lab (well, mostly) who really supported my efforts throughout these four years. To my friends back in the States, I can finally say that I made it. Devin, you've been a great friend since I met you in Astronomy all those years ago. I'm glad that we could still talk all these miles apart, and that I could see you get happily married! Sindi and Mo, I hope that you have been enjoying life outside Vegas as much as I have. It's always nice to catch up with you guys. Additionally, thanks to Joe for the help getting python to do what I wanted. I'm grateful for your willingness to share your knowledge and do crosswords with me. Kody and Alec, you were the few friends to visit me across the pond throughout the PhD. Kody, best of luck with your upcoming marriage! Addy, thanks for sticking around since high-school. Our paths led us to some different, exciting, and tropical places, but I am always glad to see you back in our hometown. Annelore and Stefan, thank you both for some amazing holidays in the Netherlands and in Austria - skiing was definitely a highlight of my PhD. If I don't mention my 6,000 hours in Dota 2, no one will know, right? Anyways, to all my gamer friends, thanks for toughing out the worst games with me. Additionally, Milan and Tippy

thanks for hanging out and giving me advice for osrs. To all my friends back home (and the ones that I haven't mentioned explicitly), thank you for being there for me, even from a distance. Your friendship has really meant a lot.

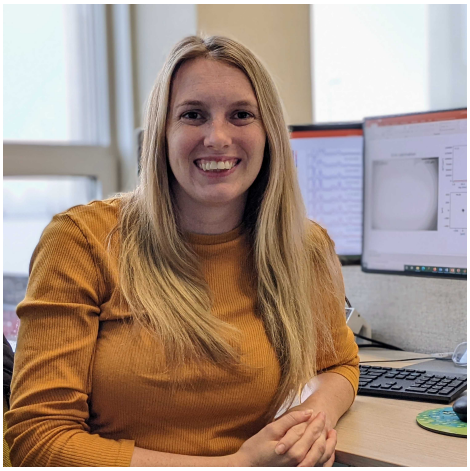
To my family, thank you so much for supporting me and letting me go so far from home without too much guilt. I am so grateful to have such a loving family that will always answer when I call. My grandparents and aunts and uncles, you have always been supportive and happy for me to do all of these crazy things so far from home. Mom and Dad, thank you so much for raising me with freedom, responsibility, and challenge. I would have never been able to do this without you. I don't know what the future will bring next, but I am glad that you are only a phone call away.

While ASM gave me the opportunity to become a PhD, I also found something else while I was there. Reece, thank you for supporting not only my goals and research, but also me. I couldn't ask for a better partner throughout this process. Your love, encouragement, and patience have been essential to me. Thank you for all the adventures and moments of joy that we have shared from exploring Europe to simply snuggling up on the couch. I can't believe four years is already ending, but I cannot wait to see where we go now.

Thank you everyone who read this far - I hope that you know I truly enjoyed working, playing, or living with you all in my life. All of your friendship, support, and collaboration has really impacted my life in the best way possible.
Sincerely,



About the Author



Sarah Schyck, born on July 14th in Murray, Kentucky, embarked on an academic journey fueled by curiosity and a passion for science. Sarah first pursued a Bachelor of Science degree in Physics at the University of Georgia, U.S.A., from 2012 to 2015. During this time, she delved into captivating projects, such as investigating the effect of organic hole scavengers on the photochromism of Bi_2WO_6 and exploring the growth of Cu nanofilms on polystyrene bead monolayer substrates through oblique angle physical vapor deposition. Seeking to expand her knowledge, Sarah obtained a Master of Science degree in Physics at the University of Nevada, Las Vegas, U.S.A., from 2016 to 2018. Her research focused on studying the inner-shell chemistry of mercury-based compounds under extreme conditions in diamond anvil cells. In 2019, Sarah began her PhD in Chemical Engineering at Delft University of Technology in the Netherlands. She has been engaged in research focusing on the preparation and out-of-equilibrium assembly of anisotropic and magnetic microparticles.

Sarah has actively involved herself in the local academic community by serving on the ChemE PhD Council, where she acted as a representative for the interests and concerns of her fellow PhD candidates. Additionally, Sarah has acted as the daily supervisor for several MSc and BSc student theses. She has also served as a graduate teaching assistant at both TU Delft and UNLV. Beyond her academic and teaching commitments, Sarah has gained valuable experience through internships and experimental research at synchrotron facilities. She worked as an ORAU and LSE intern at the Savannah River National Lab in 2016, where she conducted research on the synthesis and characterization of noble metal nanoparticles and studied the intriguing nucleation mechanism of noble metal nanoparticle growth on oxide-based particles. Sarah has also had the opportunity to engage in synchrotron experimental research at esteemed facilities such as the Argonne National Laboratory Advanced Photon Source, the University of Saskatchewan Canadian Light Source, the Lawrence Berkeley National Laboratory Advanced Light Source, and the European Synchrotron Radiation Facility.

Publications

- **Schyck, S.**, Meijer, J.-M., Baldauf, L., Schall, P., Petukhov, A. V., and Rossi, L. (2022). Self-assembly of colloidal superballs under spherical confinement of a drying droplet. JCIS Open, 5, 100037.
- **Schyck, S.**, Meijer, J.-M., Schelling, M.P.M., Petukhov, A. V., and Rossi, L. (2023). Droplet-based Assembly of Magnetic Superballs. *Submitted*.
- **Schyck, S.**, Cure, S.C., Sacanna, S., and Rossi, L. (2023). Enhancing the Active Motion of Hematite Microswimmers by Calcination. *In preparation*.
- **Schyck, S.**, Rajendra, N.M., and Rossi, L. (2023). Preparation of Magnetic Polystyrene Microparticles. *In preparation*. **Filed as patent under no. 2022E00148 NL.**

Publications obtained outside the scope of this thesis

- Hunyadi Murph, S. E., **Schyck, S.**, and Lawrence, K. (2022). Engineered Nano-antenna Susceptor as Efficient Platforms For Efficient Uptake and Release of Analytes. In T. S. Srivatsan, P. K. Rohatgi, and S. Hunyadi Murph (Eds.), Metal-Matrix Composites (pp. 351–365). Springer International Publishing.
- Murph, S. E. H., **Schyck, S.**, and Bass, J. (2022). Shape-Selective Palladium and Palladium-Composite Nanomaterials. In T. S. Srivatsan, P. K. Rohatgi, and S. Hunyadi Murph (Eds.), Metal-Matrix Composites (pp. 227–245). Springer International Publishing.
- **Schyck, S.**, Evlyukhin, E., Kim, E., and Pravica, M. (2019). High pressure behavior of mercury difluoride (HgF2). Chemical Physics Letters, 724, 35–41.
- Pravica, M. G., **Schyck, S.**, Harris, B., Cifligu, P., Kim, E., and Billinghurst, B. (2019). Fluorine chemistry at extreme conditions: Possible synthesis of HgF_4. Papers in Physics, 11, 110001–110001.
- Evlyukhin, E., Kim, E., Cifligu, P., Goldberger, D., **Schyck, S.**, Harris, B., Torres, S., R. Rossman, G., and Pravica, M. (2018). Synthesis of a novel strontium-based wide-bandgap semiconductor via X-ray photochemistry under extreme conditions. Journal of Materials Chemistry C, 6(46), 12473–12478.
- Evlyukhin, E., Kim, E., Goldberger, D., Cifligu, P., **Schyck, S.**, F. Weck, P., and Pravica, M. (2018). High-pressure-assisted X-ray-induced damage as a new route for chemical and structural synthesis. Physical Chemistry Chemical Physics, 20(28), 18949–18956.

